HYDROGEN TRANSPORT BEHAVIOR AND PHASE DECOMPOSITION OF AISI-321 AUSTENITIC STAINLESS STEEL VIA CATHODIC POLARIZATION

by

Oscar Mauricio Rosales Niño

A thesis submitted in partial fulfillment of the requirements for the degree of

MASTER OF SCIENCE
in
MECHANICAL ENGINEERING

UNIVERSITY OF PUERTO RICO
MAYAGÜEZ CAMPUS
2007

Approved by:

_____	_____
Paul A. Sundaram, Ph.D. Member, Graduate Committee	Date
_____	_____
Pablo Cáceres Valencia, Ph.D. Member, Graduate Committee	Date
_____	_____
Oswald N.C. Uwakweh, Ph.D. President, Graduate Committee	Date
_____	_____
Paul A. Sundaram, Ph.D. Chairperson of the Department	Date

ABSTRACT

Room temperature cathodic polarization of AISI-321SS austenitic stainless steel in aqueous electrolytic H_2SO_4 with hydrogen recombination inhibitor (Na_2HAsO_4) generated phase decomposition on the subsurface layer of the AISI-321 stainless steel. X-ray diffraction patterns of the input-side of the samples permeated based on the Devanathan & Stachurski (DS) twin cell, and the freely suspended or wholly charged samples revealed three distinct FCC structures, two hexagonal structures, and a BCC structure. The FCC structures were identified as retained austenite, austenite with dissolved hydrogen, and faulted austenite. These were not observed on the exit-side of the permeated samples. The hexagonal structures were identified as faulted regions or the $\varepsilon/\varepsilon_H$ – phases (with or without hydrogen), while the BCC structure was identified as a martensitic phase. The permeation test showed the dependence of the overall permeation profile as a function of charging polarization current, with the rapid decay after peak permeation. This analysis of the transient stage was used to determine the apparent diffusivity which averaged as 5.89×10^{-11} cm^2/s based on the slope method. Compared to the breakthrough method, the apparent diffusivity varied from 1.63x10-7 cm^2/s to 6.54×10^{-8} cm^2/s. Since the breakthrough time was almost independent of cathodic polarization current, the value of apparent diffusivity based on the slope method is taken to be more reliable. The decomposition of the austenitic phase accompanying the permeation implies therefore that the diffusivity is apparent.

RESUMEN

El acero austenítico sometido a polarización catódica, genera descomposición de fases en la capa inmediatamente inferior a la superficie del metal. El electrolito empleado durante la polarizacion fue de solución acuosa de H_2SO_4 la cual incluía un agente bloqueador de recombinación de hidrogeno (Na_2HAsO_4). Los patrones de difracción de rayos x obtenidos de la parte de ingreso de hidrogeno (en contacto con el electrolito acido) en las muestras que fueron permeadas mediante la técnica Devanathan & Stachurski y los patrones de difracción de las muestras que fueron cargadas de hidrogeno por ambas caras simultáneamente, revelaron tres estructuras cristalinas FCC distintas, dos estructuras hexagonales y una estructura BCC. Las estructuras FCC fueron identificadas como fase austenítica retenida, austenítica con hidrogeno disuelto y austenítica de efecto microestructural. Estas fases no se observaron en la cara de salida de las muestras perneadas. Las estructuras hexagonales fueron identificadas como regiones de falla o fases $\varepsilon_H/\varepsilon$ (con o sin hidrogeno), mientras que la estructura BCC fue identificada como una fase martensítica. Las pruebas de permeación mostraron una dependencia en función a la corriente de polarización. El análisis del estado transciente, fue usado para determinar la difusividad aparente basada en el método de la pendiente, la cual promedio $5.89x10^{-11}cm^2/s$. El método de tiempo de brecha (t_b) comparado con el método de la pendiente, indica que la difusividad aparente vario desde $1.63x10^{-7}cm^2/s$ hasta $6.54x10^{-8}cm^2/s$. Debido a que el método de tiempo de brecha (t_b) fue casi independiente de la corriente de polarización, el valor de la difusividad basado en el método de la pendiente

se toma como el más confiable. La descomposición de la fase austenítica que acompaña la permeación implica entonces que la difusividad es aparente.

To Katarina, Elvira,

Ludmila and

Jozef Labaj "Ocko" a beloved father and friend

ACKNOWLEDGEMENTS

I would like to thank my supervisor, Dr. Oswald N.C. Uwakweh that constantly encourage me and guided me through all these years with patient and wisdom in the development of this research.

I would like to thank Dr. Paul A. Sundaram, chairperson of the Mechanical Engineering Department for hosting me in his faculty and the support and collaboration he granted me since the first day of my acceptance to the department.

In the same manner I would like to acknowledge Dr. Pablo Caceres and Dr. Oscar M. Suarez for their support and suggestions during the development of the present research.

Special thanks to my kind friend and colleague Ms. Erick E. Chavarri for his support during the experimental stage of my research.

Finally I must express my gratitude to all my friends at the Department of Mechanical Engineering. My work and residence at the University of Puerto Rico was more pleasant due to their presence.

Table of Contents

Table List

Tables **Page**

Figure List

Figures **Page**

1 INTRODUCTION

Recognition of the absorption and embrittlement effects of hydrogen in iron and steels started from the beginning of the industrial revolution and still is an outstanding problem for the industry, and also in the development of new resistant alloys. The entry of hydrogen with its disastrous effects is well known [43]. Hydrogen absorption (or entry) reaction is a concern associated with the application of structural materials because hydrogen degrades metallic properties such as toughness, tensile strength, and stress intensity factor [6, 27, 43]. Due to its atomic radius 0.25-0.54 Å, hydrogen acquires significant mobility in metallic lattices and can enter the material from many sources, for instance, with melting and welding in the case of manufacturing, and in service due to electrochemical processes like corrosion and cathodic protection.

From the wide range of alloys used in the industry as structural materials, steels which are based on iron content are the most preponderant. One example is the stainless steel types whose properties derive principally from their Cr and Ni contents. Stainless Steels are commonly divided into five groups: Martensitic, Ferritic, Austenitic, Duplex (Ferritic-Austenitic) and Precipitation Hardening types. Due to low hydrogen diffusivity, austenitic stainless steels are selected for service under hydrogen environment more frequently than ferritic or martensitic steels.

Molecular hydrogen dissociation and subsequent atomic hydrogen absorption into steels have been shown to depend upon surface condition; for example, oxidized surfaces absorb hydrogen slower than clean surfaces [25]. One of the most discussed damages due to atomic

hydrogen absorption into metals is Hydrogen Embrittlement (HE). HE is a loss or reduction in the ductility of the material. This damage alters ductility mainly in Ferritic and Austenitic stainless steels [3]. Apart from the modification of mechanical properties of steels, structural changes such as the formation of internal cracks, blister, voids, etc. are also induced by HE.

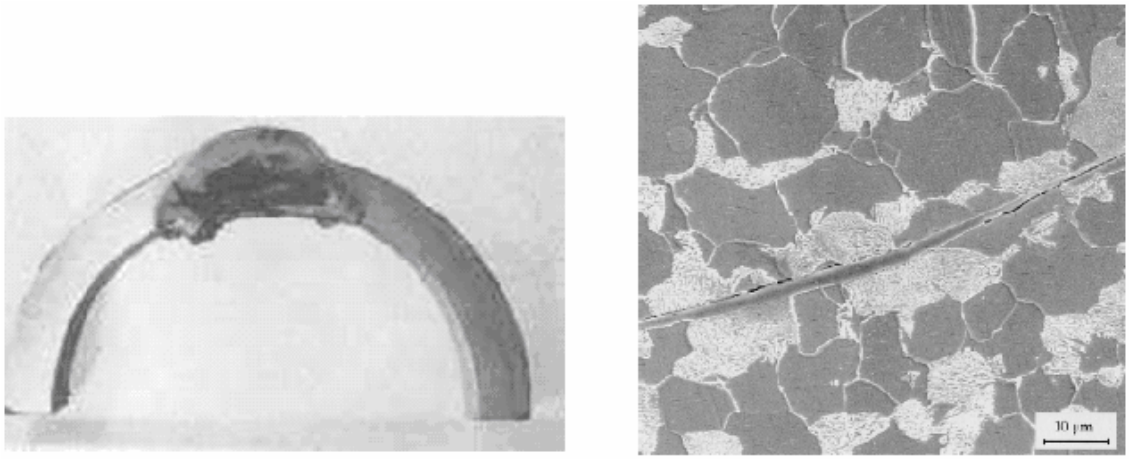

Figure 1.1 (a) Cross section of a boiler showing the damage due to hydrogen [27] (b) Hydrogen induced cracking of carbon steel in H_2S environment. [26]

Two examples of failures due to hydrogen embrittlement are shown in Figure 1.1. As seen in Figure 1.1(a), internal corrosion deposits formed on the wall of a boiler; subsequent hydroxyl ions built up on the deposit causing atomic hydrogen diffusion that consequently led to hydrogen attack. Micrograph of an induced cracking in wall of a steel pipe transporting H_2S products is shown in Figure 1.1(b). This type of damage was caused by internal hydrogen pressure.

Stainless Steel 321 is a basic austenitic 304 grade stabilized by titanium. This titanium addition reduces or prevents carbide precipitation during welding [25, 43]. It also improves the elevated temperature properties of the alloy, which includes excellent resistance to oxidation and corrosion. The AISI 321 is widely used in aircraft exhaust manifolds, heat exchangers, furnace parts or any application where elevated temperature is encountered.

During the last decades the primary techniques to characterize and investigate the phase transformation caused by hydrogen in cathodically charged austenitic stainless steels have been X-ray diffraction and Mossbauer spectroscopy while, morphology of induced phases were studied by Scanning Electron Microscopy (SEM) and Transmission Electron Microscopy (TEM). These techniques have shown that electrolytic hydrogen charging can induce the formation of ε and α' martensite phases [1, 21].

One of the methods to introduce hydrogen in steels is based on the electrochemical process developed by Devanathan and Stachurski [38]. This method is based on the use of a twin or double electrolytic cell. Hydrogen will be introduced in one side of a metal membrane by cathodic reduction while the other side of the membrane or the second cell will be filled with an alkaline electrolyte such as sodium hydroxide with enough potential to oxidize any hydrogen coming through the membrane. This experimental set-up formally called Devanathan-Stachurski (DS) double cell is extensively employed to determine the hydrogen permeation rate through metallic membranes [47].

1.1 Motivation

Determination of diffusion and hydrogen evolution mechanism on metals has been frequently based on the permeation technique developed by Devanathan and Stachurski [38]. This technique has been widely employed in studies of several types of alloys as in the case of high-strength steels, duplex stainless steels and austenitic steels. In the case involving the austenitic steels the most studied alloys subjected to hydrogen charging are the 301, 304, 310, and 316 types [1, 2, 7, 8, 11]. Nevertheless little information is found about permeation and decomposition on the AISI-321 type steel. A relatively close system to the AISI-321 steel is the AISI-304 type, which is basically the same 321 steel without titanium stabilization. Studies have shown [1] the appearance of two new phases in the 304 stainless steel, cataloged as γ* (fcc) and ε* (hcp) hydrides from samples under cathodic hydrogen charging. In the same manner, decomposition of these phases was also examined during room temperature aging. The proposed mechanisms of decomposition were the transformation from ε* (hcp) hydride to α' (bcc) phase and from γ* (fcc) to γ phase. The author suggested that hydrogen associated with ε phases may be identified as ε* hydride. This suggestion was based on observations by means of TEM and x-ray diffraction techniques. As a scope of the present work, mössbauer spectroscopy technique was included along with SEM and x-ray diffraction analysis to examine the evolution and phase decomposition of the mentioned hydride phases. In addition, hydrogen permeation on the AISI-321 stainless steel is proposed

to show the pertinent solubility and diffusivity of the material and to compare the induced phase transformation in both sides of the samples after hydrogen charging.

1.2 Objectives

1. Study the decomposition behavior of AISI-321 stainless steel during electrolytic cathodic charging.
2. Based on Devanathan-Stachursky permeation tests, determine hydrogen permeation behavior.
3. Use the hydrogen permeation behavior to determine threshold hydrogen concentration/content needed to induce phase decomposition.
4. Explore mathematical model to describe the permeation transport behavior.

2 THE EVOLUTION, ENTRY AND TRANSPORT OF HYDROGEN IN METALS

2.1 Sources of Hydrogen

The first clear appreciation of the absorption and embrittling effects of hydrogen in iron and steel by electrolytic charging seem to have been reported in the latter part of the 19th century. Smialowski denoted in his publication [43] that around 1864 Cailletet noticed the entrance of hydrogen through the steel of a rifle barrel from the furnace atmosphere due to accumulation of this gas under pressure inside the barrel hole. Since Cailletet findings, hydrogen has shown its role in modern life in a benevolent way, such as hydrogen storage cells for electricity or catastrophically in the case of absorption and embrittling effects of hydrogen in iron and steel. Hydrogen is the lightest and most abundant element in the universe and is present in water and in all organic compounds and living organisms. Its atomic radius 0.25-0.54 Å makes it highly mobile and can diffuse and be transported by movements of dislocations, through grain boundaries and other imperfections in the metallic matrix, and through porous and little internal voids for non-crystalline or polymer materials [52]. High strength steels are more susceptible to hydrogen embrittlement, since small amounts of hydrogen can lead to changes in mechanical properties such as fracture toughness [48]. In the aeronautical field, high and ultrahigh-strength steels such as AerMet® 100 and AF1410 are commonly used in making critical components such as landing gears, and horizontal stabilizers which are often subjected to extreme harsh environmental conditions and intense stresses [6, 27, 55].

In addition to the aeronautical field, hydrogen embrittlement of steels is frequently experienced during metal processing, and in chemical or petrochemical industries. Hydrogen can be unintentionally pre-charged in the structural material during treatments i.e., melting or electroplating and maintenance processes such as washing, welding or environmental exposure (hydrogen environment embrittlement).

2.2 Hydrogen Evolution

Different factors lead hydrogen to be in contact with the material, as previously discussed fabrication, maintenance and environmental exposure were among them. Once the sources of hydrogen are identified, the next step is to understand the mechanistic process of hydrogen flow and subsequent transport through the material. The ingress of hydrogen in a metallic membrane depends on many variables; surface condition, composition and nature of the metal or alloy are few examples of them [9, 12, 20, 25, 26, 43]. The type of experimental method for hydrogen charging can also be taken into consideration as a fundamental factor for the mechanism of entry and hydrogen transport to take place. In the electrochemical method for example, the hydrogen uptake is determined mainly by charging conditions, electrolyte, electrode potential and material constitution [1, 2, 8, 21, 29], while the entry of hydrogen from the gas phase is driven basically by pressure and temperature applied on the material surface [10,27, 44].

The hydrogen evolution reaction (HER) is the mechanism by which hydrogen absorption occurs. The multistep reaction starts with the discharge of the H+ ions on the metal surface

and continues with the detachment of hydrogen from the cathode and production of molecular hydrogen [43].

Different authors [18, 26, 25, 42, 43], have summarized and reported the mechanistic analysis of hydrogen evolution and absorption reactions through an iron membrane via the electrochemical permeation technique. To understand the mechanism of hydrogen flow through the metallic membrane, a description of the cycle can be summarized as follows:

At the ingoing surface: Dissociation of molecules, adsorption of atoms on the metal, Absorption of atoms from the surface inside the metal.

Inside of the metal phase: Diffusion of dissolved hydrogen atoms or anions through the membrane.

At the outgoing surface: Desorption of hydrogen atoms or ions from the metal membrane, recombination of desorbed hydrogen atoms into molecules.

2.2.1 Adsorption

The basic condition for the adsorption of a gas molecule on a surface is the collision of the molecule with the surface. The heterogeneity of this surface is a valid factor for increasing the adherence probability. Such heterogeneity comes for example from surface composition of an alloy, presence of contaminants (oxide, sulfides), or clean metallographic treatment (grinding and polishing). Under the latter considerations, an arriving molecule has a chance to attach to a suitable adsorption site (vacant site) where then it is possible for it to be

adsorbed into the metal or returned to the gas phase by recombination of its atomic species [25]. The reaction can be seen as follows [18]:

$$H^+ + e^- + M \xrightarrow{k_1} M\text{-}H_{ads}$$

Where M - H_{ads} is the adsorbed hydrogen atom on the metal surface. And k_1 is the discharge rate constant of the HER.

The formation of molecular hydrogen occurs via the chemical recombination:

$$M\text{-}H_{ads} + M\text{-}H_{ads} \xrightarrow{k_2} 2M + H_2$$

Or also by electrochemical reaction:

$$M\text{-}H_{ads} + e^- + H+ \longrightarrow M + H_2$$

2.2.2 Absorption

Once the hydrogen atom is absorbed in the bulk of a metal it has to pass through the surface; this is the hydrogen absorption reaction (HAR). The reaction can be seen as follows [18]:

$$M\text{-}H_{ads} \underset{k_{des}}{\overset{k_{abs}}{\rightleftharpoons}} M + H_{abs}$$

Where M + H_{abs} refers to an absorbed hydrogen atom in the metal lattice, and k_{abs} and k_{des} refer to the rate constants of the forward and backward direction of reaction.

At this stage, absorbed hydrogen begins to diffuse deeper into the metal and accumulates not only interstitially but also at voids, inclusion or dislocations. As a result of this accumulation embrittlement of the material takes place.

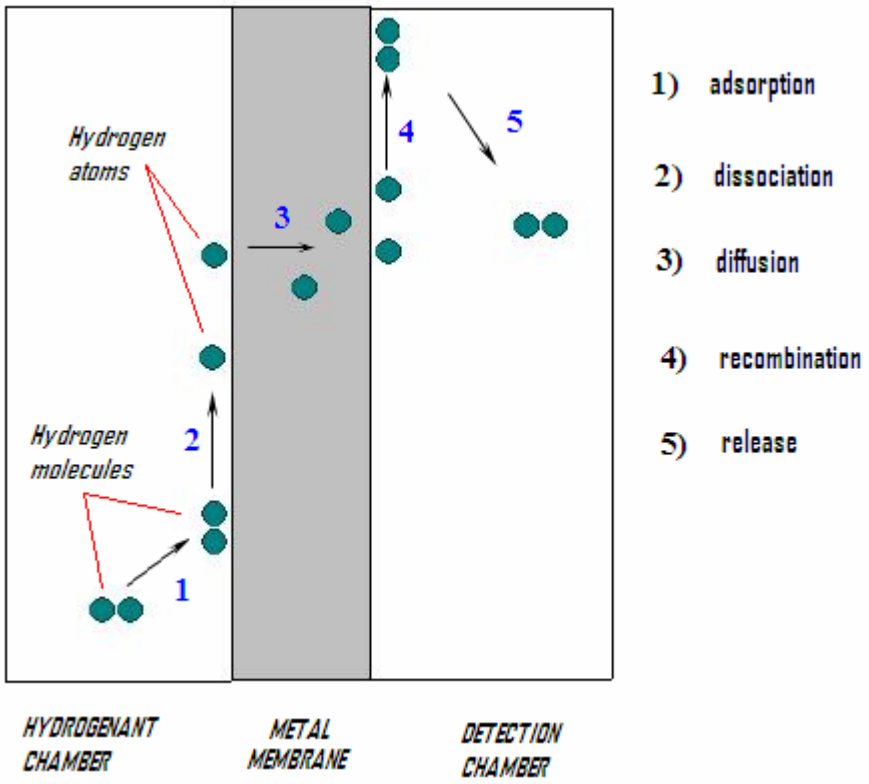

Figure 2.1 Steps during hydrogen transport in a metallic membrane [48]

Another model by T. Zakroczymski [53], shows the mechanism of the cathodic evolution of hydrogen from aqueous electrolytes. This model emphasizes the entry of hydrogen into steel during its dissolution in strong acids by cathodic polarization, which is accompanied by hydrogen gas evolution.

Depending on the electrolyte, the HER can be written as follows:

$$2H_3O^+ + 2e^- \longrightarrow H_2 + 2H_2O \qquad \text{(in acid solutions)}$$

$$2H_2O + 2e^- \longrightarrow H_2 + 2OH^- \qquad \text{(in alkaline solutions)}$$

The two following steps are essential to the overall HER mechanism. The first one consists in either a discharge of hydrated protons:

$$H_3O^+ + M + e^- \longrightarrow M\,H_{ads} + H_2O \qquad \text{(in acid solutions)}$$

or electrolysis of water:

$$H_2O + M + e^- \longrightarrow M\,H_{ads} + OH^- \qquad \text{(in alkaline solutions)}$$

Where H_{ads} represents the hydrogen atom adsorbed on the metal surface.

The subsequent mechanism of the second step depends on the nature of the electrode metal and the applied cathodic current density. The reaction is then for chemical desorption (acid or alkaline solutions):

$$M H_{ads} + M H_{ads} \longrightarrow H_2 + 2M$$

For the electrochemical desorption:

$$M H_{ads} + H_3O^+ + e^- \longrightarrow H_2 + H_2O + M \qquad \text{(in acid solution)}$$

$$M H_{ads} + H_2O + e^- \longrightarrow H_2 + OH^- + M \qquad \text{(in alkaline solution)}$$

Similarly Smialowski [25] mentioned in his publication the work done by Bockris et al., who proposed a model of hydrogen entry into metals, which considers that the stage through which electrolytic hydrogen passes to the metal substrate is the adsorbed state, and, is identical to the stage that leads to hydrogen evolution.

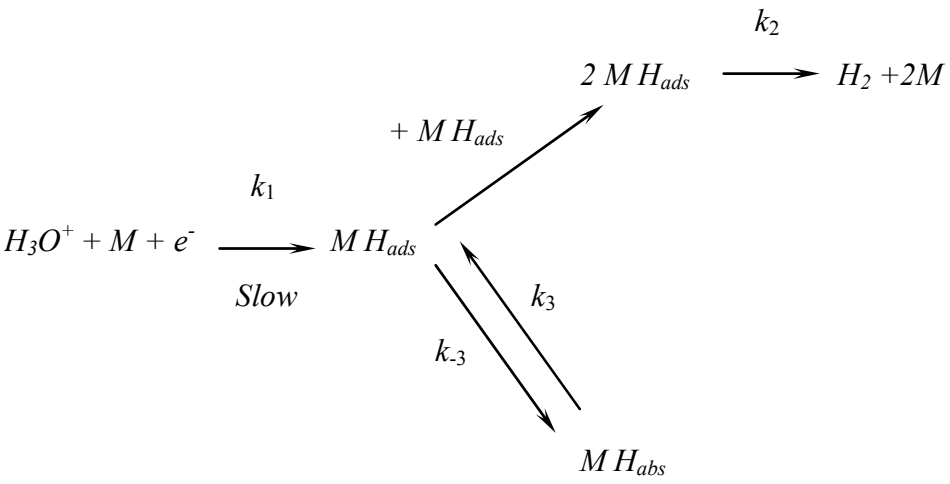

Where M H_{ads} refers to adsorbed hydrogen on the metal surface, M H_{abs} is the absorbed hydrogen beneath the metal surface, and k_1, k_2, k_3, are rate constants for the respective steps. This model indicates that the permeation rate at the entry side should be proportional to the

coverage of the metal surface (accumulation of H_{ads} over a certain area) by adsorbed hydrogen atoms.

2.2.3 The Diffusion Process

Diffusion is the means by which matter is transported or migrated through matter or another part of the system. Among the several different models of diffusion, there are two predominant for diffusion of atoms in a crystalline metallic lattice; the vacancy or substitutional diffusion mechanism and the interstitial mechanism. In the first mechanism, atoms can jump in crystal lattices from one atomic site to another when there is sufficient activation energy, while the second one refers to the movements of atoms from one interstitial site to another.

2.2.4 Steady State Diffusion

This diffusion condition assumes that over a period of time there is no change in concentration of solute atoms and therefore there will be a net flow of atoms from the region of higher concentration to the one of lower concentration. This kind of flow can be represented by Equation (2.1).

Fick's first law $$J = -D\frac{dC}{dx} \qquad \textbf{2.1}$$

In Equation (2.1), J indicates the flux of net flow of atoms (moles cm^{-2} s^{-1}). D is the diffusivity or diffusion coefficient (cm^2 s^{-1}) and the differential term is concentration gradient (moles cm^{-3} cm^{-1}).

2.2.5 Non-Steady State Diffusion

In this case the concentration of solute atoms at any point in the material changes with time. Fick's second law is shown in Equation 2.2 and it is possible to represent the diffusion of hydrogen when trapping effects are neglected.

Fick's second law $$\frac{\partial C}{\partial t} = D\frac{\partial^2 C}{\partial x^2} \qquad \textbf{2.2}$$

One practical solution of Equation 2.2 is for a semi-infinite solid in which the surface concentration is held constant, and the following assumptions can be made:

- Before diffusion, any of the diffusing solute atoms in the solid are uniformly distributed with concentration of C_0.
- The value of x at the surface is zero and increases with distance into the solid.
- The time is taken to be zero the instant before the diffusion process begins

The boundary conditions are expressed in a simple manner as follow:

$t = 0, \quad C = C_0 \qquad$ at $0 \leq x \leq \infty$

$t > 0, \quad C = C_s \qquad$ at $x = 0$

$C = C_0 \qquad$ at $x = \infty$

As the time of diffusion increases the concentration of solute hydrogen atoms at any point in the x direction will increase. If the diffusivity of the hydrogen into the membrane is independent of the position then a particular solution of the Fick's second law by means of the separation of variables leads to a mathematical function in the form of the error function:

$$\frac{Cs-Cx}{Cs-Co} = erf\left(\frac{x}{2\sqrt{Dt}}\right) \qquad \textbf{2.3}$$

Equation 2.3 represents the concentration ratio between the surface concentration of hydrogen diffusing into the surface (C_s), concentration of hydrogen at a distance *x,* at time, *t,* (C_x), and the initial bulk concentration (C_o), *x* means the distance from the surface.

2.3 Methods of Hydrogen Charging

2.3.1 Charging From the Gas Phase

Hydrogen is not dissolved in the bulk of a metal as molecules but as atoms. The dissociation takes places in an adsorption layer on the surface, followed by the whole process of hydrogen ingress into metals which entail the following steps: adsorption to the surface, dissociation, ionization, diffusion, recombination and desorption. One important factor for adsorption of a gas molecule on a surface is the collision of this molecule with the surface [25]. Based on the kinetic theory of gases, the number N of molecules of mass *m* colliding on the unit of surface area per unit of time *t* at a gas pressure *p* is given by:

$$\frac{\partial N}{\partial t} = \frac{p}{\sqrt{(2\pi m k_B T)}} \qquad \textbf{2.4}$$

Where k_B is the Boltzmann constant and T the absolute temperature.

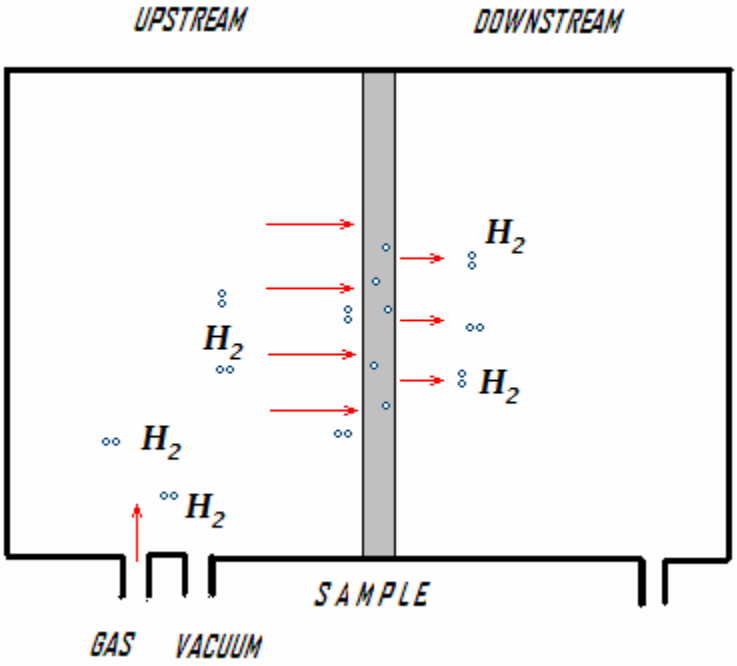

Figure 2.2 Schematics of a gas phase hydrogen permeation chamber [44]

As indicated by R. Mousavinejad [44], the procedure for obtaining gas phase hydrogen permeation is to maintain a sealed membrane with a thickness limitation no bigger than 1mm and to evacuate the volumes on both sides of the sample. The sample is then heated to a desired temperature and hydrogen at a known pressure is introduced at the upstream side of

the membrane. The flow of hydrogen through the sample is monitored as a function of time until the rate flow becomes time independent. After the steady state flow has been determined, hydrogen is quickly removed from the gas supply side. A final recording of the pressure – time diagram is obtained where the sigmoid permeation type curve can be visualized.

2.3.2 Electrochemical Charging

The electrochemical hydrogen charging by cathodic polarization is a widely used technique due to its simplicity. It consists of a solution (acid or alkaline) under cathodic polarization where hydrated cations are transported towards the cathodic side of the sample at the entry side of the electrolytic cell. This hydrating effect allows the reduction and transport of hydrogen through the membrane by diffusion. The diffused hydrogen atoms oxidize back to hydrogen ions at the anodic cell; this oxidation effect consumes electrical current from the solution that can be quantified. The obtained profile represents the rate of hydrogen diffusion (D) through the membrane [5, 12, 20].

Different techniques can be used to determine the diffusion coefficient (D) for permeation experiments in a given material as follows [42]:

Potentiostatic: This technique assumes an initial concentration of hydrogen with an equilibrium potential, then a constant potential (E) is applied between the sample and electrode. Finally an evolution of current (I) is measured and recorded.

Galvanostatic: In this method the controlled parameter is the current (I) while the varying parameter is the potential (E) on the surface of the sample.

Potentiometric: In this case the initial concentration is assumed to be constant and correspond to an equilibrium potential (E_o). A short high current is applied and the potential variation is measured as a function of time for $t > 0$.

Steady-State AC method: This technique also assumes a constant concentration and an equilibrium potential (E_o). A small sinusoidal AC signal E_{max} sinwt (amplitude of the AC voltage, w= $2\pi f$, f=frequency) is superimposed upon the constant DC voltage E_o and the response impedance parameters are monitored.

2.4 Hydrogen Permeation

To characterize the flow of hydrogen through a membrane, the most common technique for electrochemical hydrogen permeation was developed by Devanathan and Stachurski [38, 47] and takes the advantage of a double or twin cell named Devanathan-Stachurski (DS) double cell after the authors. Schematics of the cell configuration can be seen in Figure 2.3.

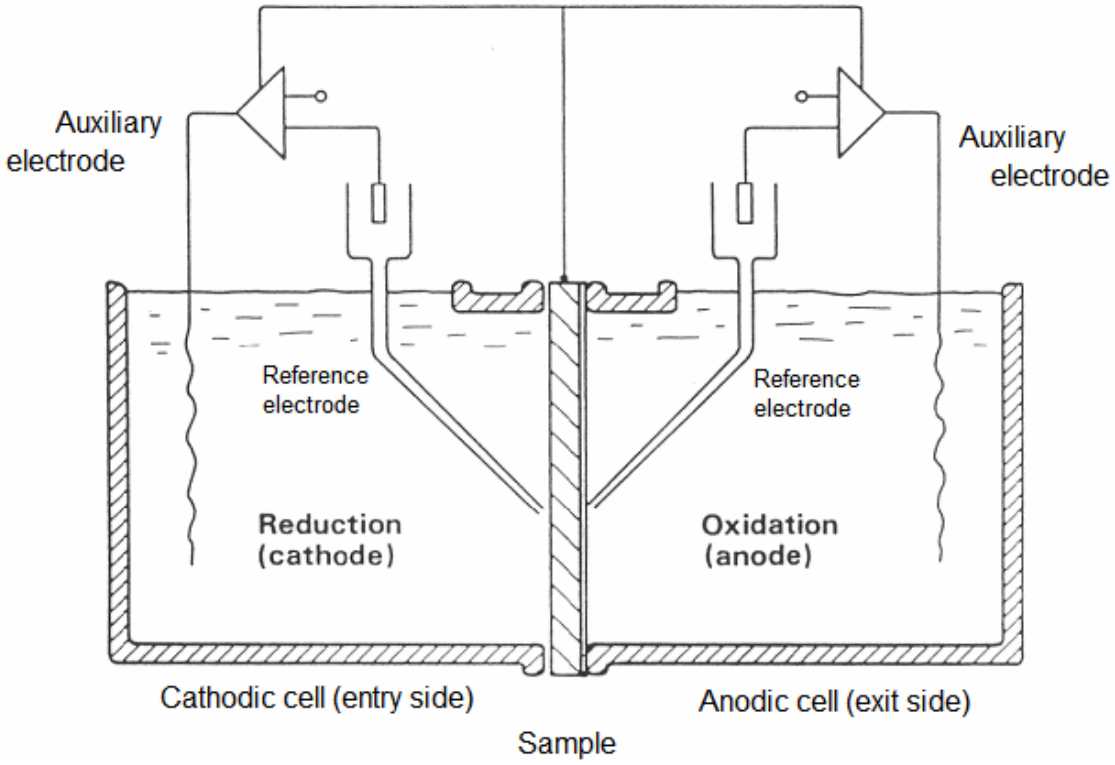

Figure 2.3 Twin cell as used by Devanathan and Stachurski [38]

The DS technique was based on the theory that the rate of permeation of hydrogen is controlled by diffusion in a material. The technique consists of a two compartment cells clamped to a metallic membrane. This membrane forms a partition wall between the chambers. One side of the membrane (charging side) is covered with absorbed atomic hydrogen produced by cathodic reduction at a certain current, while in the opposite side (oxidation side) the amount of atomic hydrogen is set to zero. The charging cell contains an acid solution while the oxidation cell contains an alkaline electrolyte. The first cell promotes hydrogen charging, while in the second the membrane is kept passive at a potential enough to oxidize any hydrogen coming through the membrane by anodic polarization.

The ingress and diffusion of hydrogen is due to the concentration gradient at the entry side of the membrane. The measurement of the oxidation current provides a direct determination of the hydrogen flux permeating the thickness membrane material.

Figure 2.4 shows a typical permeation transient (current density Vs time) obtained by Devanathan and Stachurski on Armco iron. J_∞ represents the steady state permeation point (limiting value) attained during the experiment. One of the methods employed for determining the diffusion coefficient (D) entails determining based on this method the time taken for the permeation to reach 0.63 of its limiting value (Equation 2.5) [38].

$$T_p=0.63\ J_\infty \qquad \textbf{2.5}$$

Where T_p is the time required for the permeation rate to attain 63% of the steady-state value (J_∞). Another way for calculating the diffusivity is by the use of the classical time lag method. This method is related to T_p by:

$$T_p = 0.63\ J_\infty = T_{lag} = L^2 / 6D \qquad \textbf{2.6}$$

Where L is the thickness of the membrane, and T_{lag} is the time lapse before the emergence of hydrogen at the exit side.

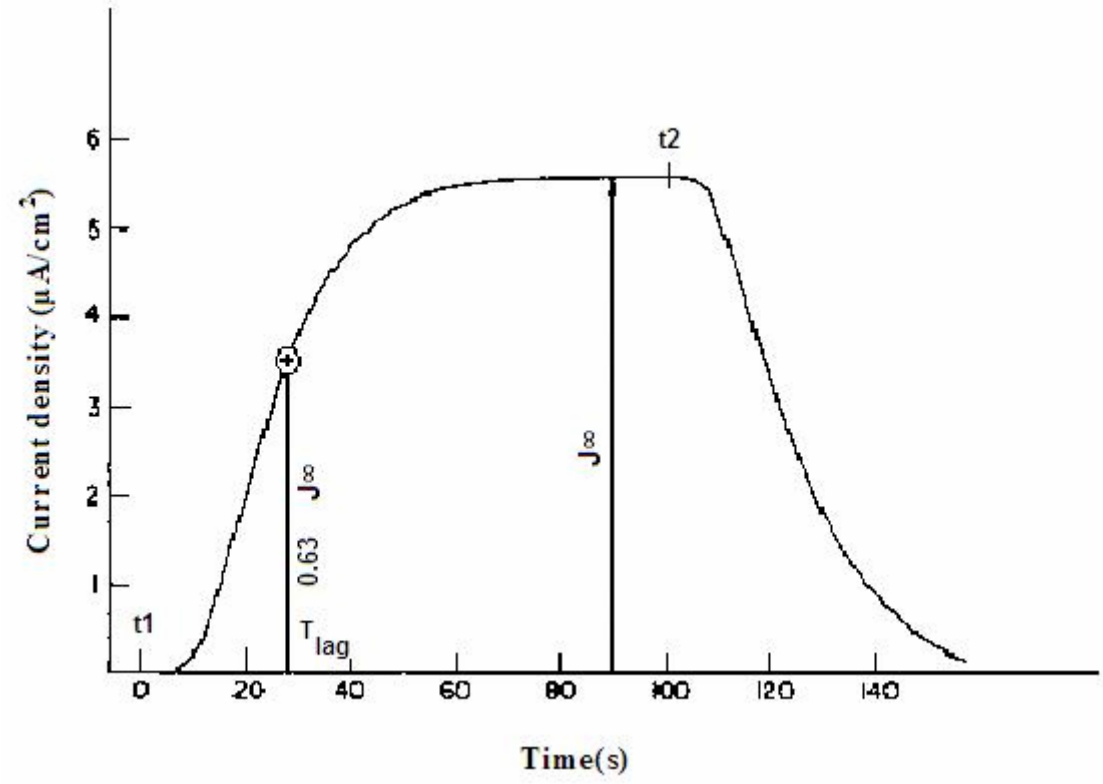

Figure 2.4 Typical permeation transient as stated by Devanathan and Stachurski [38]

In addition to the two methods mentioned above, another way for determining the diffusivity is the slope method. As seen in equation 2.7, L represents the thickness of the membrane and K, the slope obtained in the linear part of the transient of the permeation process such that once the value of K is known, then D, can be calculated.

$$K = \frac{L^2 \log(e)}{4D} \qquad \textbf{2.7}$$

2.5 Trapping of Hydrogen

Metallurgical defects and imperfections such as voids, dislocations, vacancies etc., can act as trapping sites, and thereby play a crucial role in the uptake and transport of hydrogen in a material. One consequence of the presence of trap sites is the decrease in the rate of transport of hydrogen through the metallic membrane, because the residence time of hydrogen can become longer than in a perfect lattice diffusion situation. Hydrogen traps can also affect the accurate evaluation of the physical properties such the diffusion coefficient and solubility limits in steels, and hydrogen desorbed from the bulk material.

According to their energies, traps can be divided in two identified categories known as reversible and irreversible types. Reversible traps are characterized by low interaction energy; due to this, the accompanying residence time of hydrogen atoms in them is short, because they (hydrogen) can leave the site easily. On the other hand, irreversible (or deep traps) are sites in which the hydrogen atoms are tightly bound such that more energy has to be provided for their bulk release. Table 2.1 shows the binding energies for some classical traps found in different materials.

TABLE 2.1 Examples of traps in ferrous materials [26]

Traps	Binding energy (kJ / mol)	Degassing temperature (˚C)	Material
Matrix	6.9	Room temperature	Fe
Grain boundaries	17.15	112	Fe
Dislocations	20 – 26	215	Fe
		200	Fe
		272	AISI 4340 (carbon steel 0.39%C)
Microvoids	35 – 48	338	AISI 4340
		305	Fe
		480	Carbon steel (0.47 %C)
MnS inclusions	72	495	AISI 4340
Carbides interfaces	96.6	723	Fe

A model for trapping sites is presented in Figure 2.5, according to [12]. In this model, traps are distinguished in terms of the activation energy levels separated by a characteristic distance λ. This distance can be determined using the relationship [54] $\lambda = \sqrt{(D/v)}$, where v is the vibration frequency of a trapped hydrogen. The relevant value to hydrogen in steel is on the order of $\lambda = 2x10^{-8}$ cm. The energy of hydrogen entry from surface into the bulk material is represented in Figure 2.5, as E_a, while E' represents the energy level for hydrogen jump from the bulk to trap site. ΔE_x characterizes the kind of trapping energy necessary for hydrogen to leave the trap site. Finally the total activation energy of trapping E_T relates the

nature of the dissociated trapping site, for example if the energy of E_T is greater than ΔE_x ($E_T >> \Delta E_x$), then the trap corresponds to the irreversible type.

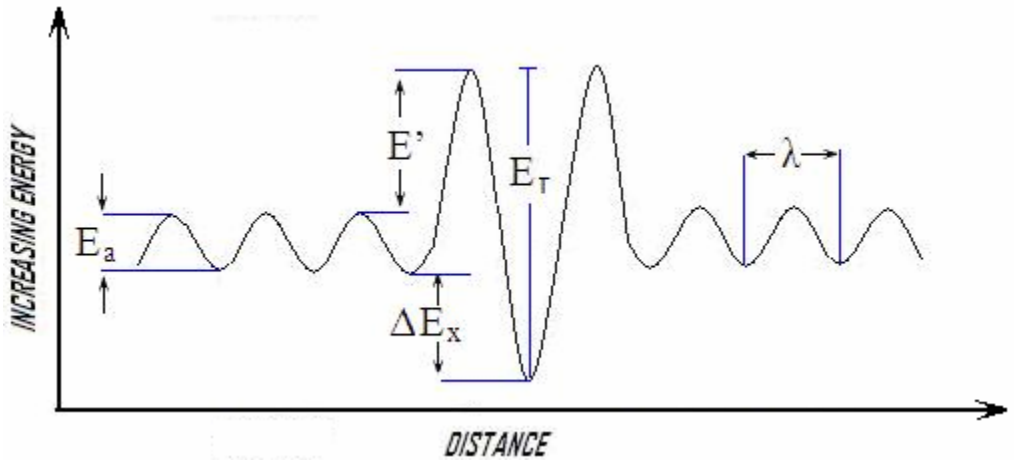

Figure 2.5 Trapping site model

Molecules of hydrogen cannot diffuse through the metal phase, due to their greater dimension in comparison with atoms and ions; hence, if one is formed inside an internal structure defect, it gets trapped there. Three characteristic cases can be noted based on the distance from the trap to the surface:

When the trap lies near the immediate surface of the membrane: Blisters are formed and at certain pressure, the walls of the blister crack and hydrogen escapes.

When the trap lies at a not so far distance of the surface: Accumulated hydrogen causes a blowhole, and the surface wall is elastically and plastically deformed.

When the trap lies far below the surface of the metal: High pressure is generated over small quantities of hydrogen atoms retained into the structure, surpassing the equilibrium (stationary state) between the walls and atomic hydrogen pressure. At this stage, the trap collapses and becomes inactive.

2.5.1 Promoters of Hydrogen into Metals

Several compounds have the ability to promote the entry of hydrogen into metals such as iron, steel and nickel, from gaseous or liquid environments. These promoters or known otherwise as "poisons" show their effect even at low concentrations in the electrolyte media. These promoters have the property of acting as a negative catalyst for the hydrogen recombination reaction.

It has been shown that the most effective promoters belong to the Vth and VIth periodic groups [25]. There are also indication of a similar but less effective influence of hydrogen promotion in anions (cyanide, rhodanide and iodine), and compounds of carbons (carbon sulfide, carbon monoxide and urea). Certain organic compounds, for example thiourea, decompose at the metallic sample giving hydrogen disulphide, while others such as arsenic distinctly promotes the penetration of hydrogen into iron membranes at concentrations of some $4x10^{-8}$mole/l [43]. During experimental hydrogen charging, it is important to consider that under prolonged electrolysis these elements escape into the atmosphere as hydrides, and the charging solution may experiment their reduction.

Some of the most common compounds known to promote hydrogen entry are shown in Table 2.2:

TABLE 2.2 Examples of hydrogen Promoters and Compounds [43, 25]

Periodic group or compound	Promoter
V-A	Phosphorous, Arsenic, Antimony
VI-A	Sulfur, Selenium, Tellurium
Carbon compound	CS_2 (carbon sulfide), CO (carbon monoxide) CON_2H_4 (urea), CSN_2H_4 (thiourea)
Anions	CN^- (cyanide), CNS^- (rhodanide), I^- (iodide)

2.6 Consequence of Hydrogen Transport in Metals

2.6.1 Hydrogen Embrittlement Interaction

Hydrogen has been observed to influence the loss in ductility, decrease in true stress and fracture behavior of all metals investigated to date [6, 10, 27, 48]. As a consequence of these effects, the capacity of an engineering structure to withstand the required load is degraded severely by the presence of hydrogen within the metal lattice or as massive hydrides on the metal surface.

When a steel sample is immersed in an acid solution in which it reacts to liberate hydrogen, some parts of this hydrogen enters into the material bulk and sometimes it may diffuse through the steel. When a pre-charged sample is removed from the solution and held in air, the contained hydrogen tends to diffuse out leaving remnant space and hence creating deformations. This introduction of a foreign atom into a metallic interstice involves a local strain in the lattice; as a result, the metal becomes very hard and brittle. The smaller the size of the interstice relative to the dissolved hydrogen atom, the more the lattice will be deformed. In the case of austenitic steel (γ-phase of iron, fcc) which has large interstices dissolves more hydrogen than the martensitic steel (α-phase of iron, bcc), but the solubility in this martensitic steel, is greater than the solubility of the modified martensitic steel (ε-phase of iron, hcp) even thou it has larger interstices [43]; this means, that the geometrical factor plays barely any part in the solubility of hydrogen for austenitic stainless steel. Direct consequences of hydrogen embrittlement (HE) in metal and alloys can be summarize as the formation of compounds in the case of metallic hydrides, the loss of mechanical properties due to fracture enhancement and hydrogen induced cracking (HIC), and phase decomposition or phase transformation which affect the geometrical factor of the material crystalline structure (for example fcc to other phases).

In spite of the fact that hydrogen embrittlement has not been fully understood, different mechanisms and theories have been proposed to describe the embrittlement mechanism in metals; such theories [48] can be summarized as follows:

Pressure Theory: Hydrogen increases its concentration within the internal defects. This increment creates a large internal pressure which facilitates the formation of voids and cracks.

Surface Interaction: This theory proposes that hydrogen adsorbs on the free surface created during crack propagation. As a consequence, the energy necessary for the increase of the crack area is thereby decreased and the metal becomes brittle.

Hydride Precipitation: Hydrogen diffuses in the bulk material and forms hydride when its terminal solid solubility is exceeded. Hydrides are brittle phases and their precipitation results from simultaneous processes, such as hydrogen diffusion into the bulk, material deformation and non-mechanical energy flow. As a result, a material subjected to these processes can concentrate hydrides in areas of triaxial stress ahead of a crack tip.

Figure 2.6 summarizes the steps involved during the embrittlement process. Primary steps entail processes such as hydride formation, hydrogen transport, lattice decohesion and dislocations interaction. Secondary steps influence the main embrittlement one, and are associated with the impurities from the environment, surface hydrides and oxide films,

plastic blunting and the level of triaxiality. It can be concluded that hydrogen does not affect appreciably the elastic properties of metals, but it highly influences the plastic properties.

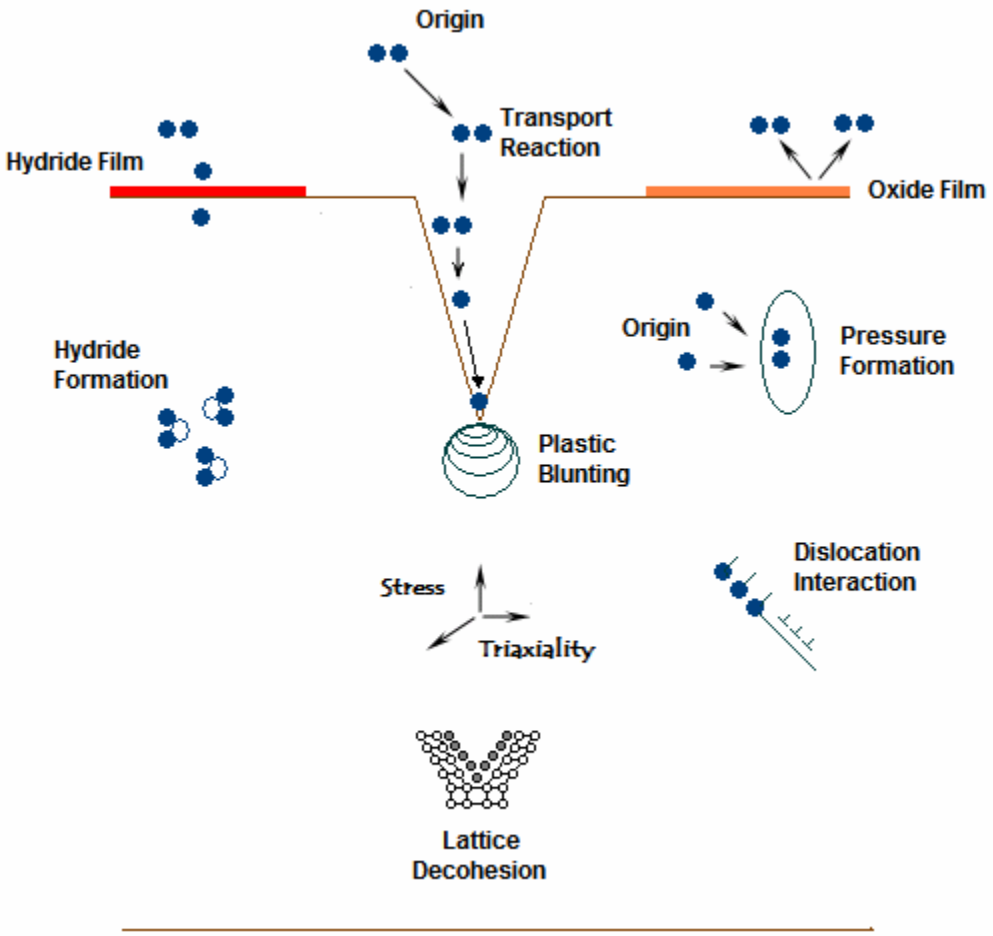

Figure 2.6 Schematics of primary and secondary effects during hydrogen embrittlement in metals [48]

2.7 Mathematical Models for Hydrogen Permeation Transient and Discharge

Mathematical models for examining the permeation transient through a membrane have been developed [5, 19, 35, 37] for potentiostatic and galvanostatic charging. As seen in the Figure 2.7, if one sets one side of the membrane (entry side) at constant concentration C_o, the other side (exit side) at C_L and an initial condition of constant concentration C_i for the membrane before charging, then there will be a time for establishing the steady state condition.

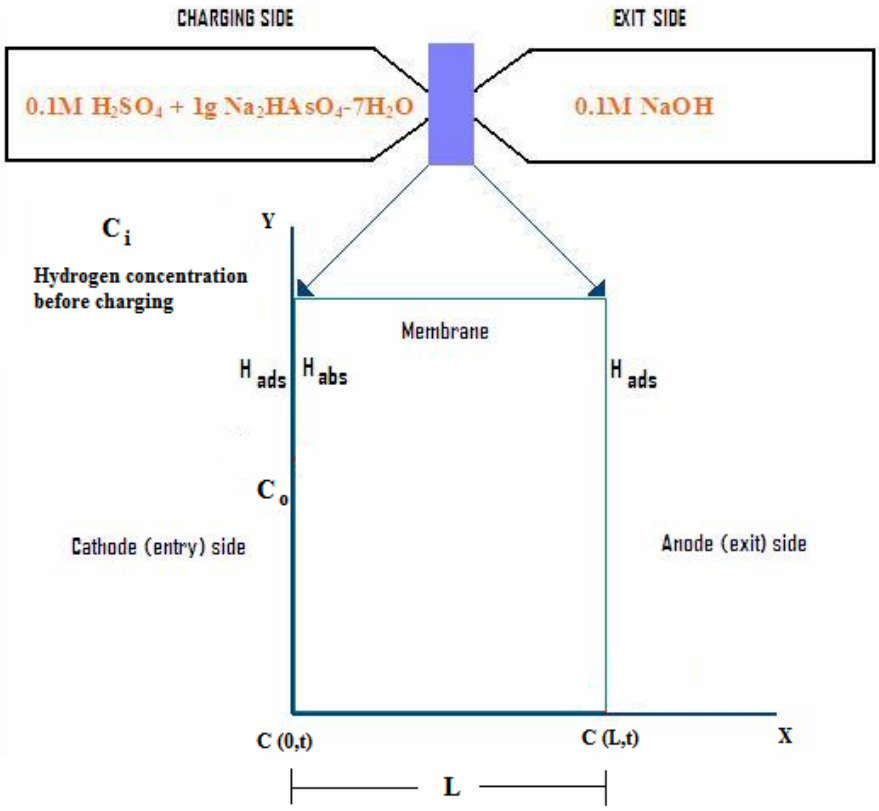

Figure 2.7 Schematics of boundary conditions applied to a membrane between the electrolytic cells

Initial condition

$$C(x,0) = C_i$$

Boundary conditions (for t > 0)

$$C(0,t) = C_0$$

$$C(L,t) = C_L$$

Once the boundary and initial conditions are set, the solution for the Fick's second law by means of the separation of variable method gives:

$$C = C_0 + (C_L - C_0)\frac{x}{L} + \frac{2}{\pi}\sum_{n=1}^{\infty}\frac{C_L\cos n\pi - C_0}{n}\sin\left(\frac{n\pi x}{L}\right)\exp\left[-D\left(\frac{n\pi}{L}\right)^2 t\right] + \frac{4C_i}{\pi}\sum_{m=1}^{\infty}\frac{1}{2m+1}\sin\left(\frac{(2m+1)\pi x}{L}\right)\exp\left[-D\left(\frac{(2m+1)\pi}{L}\right)^2 t\right] \quad 2.8$$

Experimental arrangement established that the membrane is initially at zero concentration (C_i=0); in the same manner, the concentration at the exit side of the membrane is either maintained at zero (C_L=0). Base on the previous assumptions, Equation 2.8 can now be written as follows:

$$C = C_0 + C_0\frac{x}{L} - \frac{2}{\pi}\sum_{n=1}^{\infty}\frac{C_0}{n}\sin\left(\frac{n\pi x}{L}\right)\exp\left[-D\left(\frac{n\pi}{L}\right)^2 t\right] \quad 2.9$$

Equation 2.9 describes the hydrogen concentration distribution for different times.

The typical sigmoid permeation transient profile can be derived from Equation 2.1, 2.2 and 2.9 giving the following result:

$$J(t) = J_{\infty}\left[1 + 2\sum_{n=1}^{\infty}(-1)^{n}\exp\left(-D\left(\frac{n\pi}{L}\right)^{2}t\right)\right] \qquad 2.10$$

Analysis made by Zakroczymski [3] showed that is possible to obtain a desorption model represented by Fick's second law under initial condition of constant hydrogen flux permeating through the sample. The equation for predicting and fitting the experimental decay (desorption) at the entry side (X=0) of the DS cell is presented in Equation 2.11 as follows:

$$\frac{J_{H,0}}{J_{\infty}} = 2\sum_{n=1}^{\infty}\exp\left(-\frac{n^{2}\pi^{2}Dt}{L^{2}}\right) \qquad 2.11$$

$J_{H,o}$ means the desorption rate of hydrogen at the entry side (charging side mA/cm^2), while $J\infty$ is the initial steady state permeation rate of hydrogen (mA/cm^2).

The previous equations may also be used to calculate the hydrogen diffusivity once the concentration at the input side settles at a new value after the change of cathodic current. [3, 37.

The equation equivalent for the desorption model at the exit side (X=L) is:

$$\frac{J_{H,L}}{J_{\infty}} = -2\sum_{n=1}^{\infty}(-1)^{n}\exp\left(-\frac{n^{2}\pi^{2}Dt}{L^{2}}\right) \qquad 2.12$$

2.8 Induced Transformations in Steel by Cathodic Charging

2.8.1 Hydride Formation

The negative ion of hydrogen (hydride) is used to describe compounds of hydrogen with other elements. The bonding of these hydride ranges from metallic to covalent to ionic with a great variation in their stability. All metals that form stable hydrides are hydrogen embrittled, and some of them have a greater possibility for hydride formation due to the structure and electron configuration at the d-orbital. Table 2.3 shows some of the most common hydrides formed under the influence of cathodic charging [49].

TABLE 2.3 Examples of some hydrides promoted by cathodic charging [43, 25]

Element	Atomic Number	Hydride	Element	Atomic Number	Hydride
H_2	1	H_2	Ti	22	TiH_2
N_2	7	NH_3	Y	39	YH_2, YH_3
O_2	8	H_2O	Cu	29	CuH
P	15	PH_3	V	23	VH, VH_2
S	16	H_2S	Ni	28	NiH
As	33	AsH_3	Al	13	AlH_3
Se	34	H_2Se	Fe	26	FeH
Sb	51	SbH_3	Mg	12	MgH_2
Te	52	H_2Te	Cr	24	CrH, CrH_2
Bi	83	BiH_3	Ta	73	TaH

2.8.2 Phase Transformation

High fugacity of hydrogen atoms due to cathodic charging promotes phase changes throughout the material. These changes are accredited to the lattice strain hosting hydrogen solution in austenite [25]. X-ray analyses have shown that the increment of the interatomic spacing can be up to 3 to 5% for typical charging conditions, which when converted to unit cell volume, the increment is 5 to 8% for hydrogen-metal atom ratios of 0.4 to 0.7.

Oriani in his publication [25], mentioned the work of Caskey [55] in which it was indicated that hydrogen expanded not only the austenite (γ) lattice but also several phases such as ε-phase, expanded γ * and expanded ε* phases formed in types 304, 304L, 316, 316L and 310 stainless steels. Structures identified by x-ray such as ε and α' phases were the same as those formed by cold work or low temperature transformation. Caskey [55] also noted that in the 304 stainless steel, diffraction patterns obtained after cathodic charging showed consistent changes with hydrogen clustering on (110) and (111) planes with ε phase in near surface and γ phase in interior regions.

Another study of the hydride formation and decomposition in electrolytically charged metastable austenitic stainless steel (304 and 305 types) at room temperature with current densities of 1, 10 and 100mA/cm^2 was done by Chen et al. [1]. As a comparison, these authors began their study on the transformation by cathodic charging of stable austenitic stainless steel of type AISI 310. The transformations sequence for the system was expressed as follows [1]:

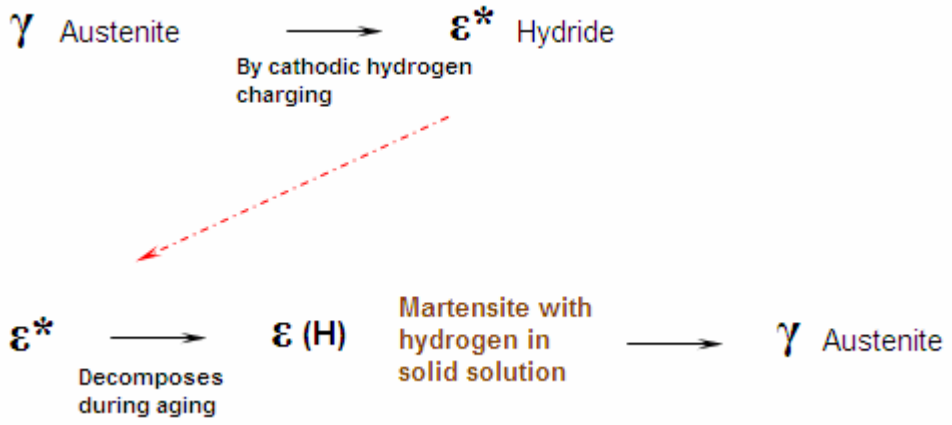

During the transformation, no α' martensitic phase was observed after aging in hydrogen-charged AISI 310 type steel [1].

On the other hand, studies done on the metastable austenitic 305 stainless steel by the same authors, showed the following transformation:

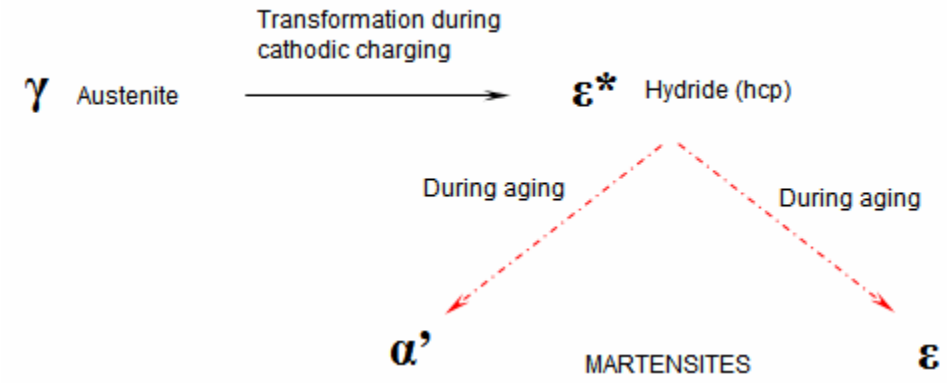

The presence of the resultant phases (ε and α' martensites) was confirmed by transmission electron microscopy (TEM), showing that hydrogen-induced ε martensite is crystallographically and morphologically identical to strain-induced ε martensite. TEM analyses also showed that the ε-phase appeared mainly near the membrane edge as small plates resembling stacking faults. Similarly α' martensite plates were present in the middle of the sample after hydrogen charging [1].

Continuing with the investigation, Chen et al [1] examined the effect of charging on phase transformation for the ultra low carbon 305 and 304 type steels based on by x-ray diffraction measurement after typical charging conditions of 100mA/cm^2. The peaks observed are shown in Table 2.4.

TABLE 2.4 Observed peaks after charging the AISI 305 stainless steel [1]

AISI 305	First Peak	Second Peak	Third Peak
Phase	α'	ε*	ε
Plane	{110}	{10$\bar{1}$1}	{10$\bar{1}$1}
Lattice Parameter	a=0.288nm	a=0.261nm c=0.425nm c/a=1.628	a=0.257nm c=0.419nm c/a= 1.630
Angle	44.5	45.5	46.2

TABLE 2.5 Obtained peaks after charging the AISI 304 stainless steel [1]

AISI 304	First Peak	Second Peak
Phase	γ* Fcc	ε* Hcp
Plane	{111}	{10$\bar{1}$1}
Lattice Parameter	a= 0.362nm	a=0.261nm c=0.425nm c/a=1.628
Angle	42.8	45.5

The effect of aging time on phase transformation at room temperature was also studied by the author who observed changes in the X-ray spectra. Pertinent overall phase transformations after (20 minutes approximately) for 305 and 304 type stainless steels were described as follows:

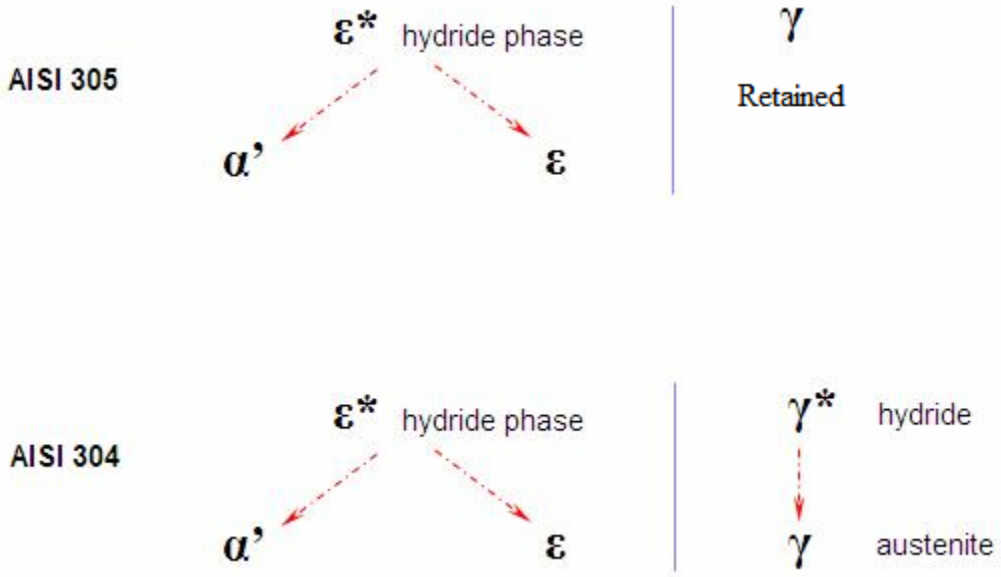

Finally, a summary of the process of transformation during low charging involves the dissolution of hydrogen into the matrix accompanied by the lowering of the stacking fault energy (SFE) of the austenite phase and increasing the lattice strains. The sequence of transformation was identified to be [1]:

$$\gamma \dashrightarrow \varepsilon \dashrightarrow \varepsilon^*$$

Disagreements on the previous discussion are found on the work done by Olson and Cohen [46]. They indicated that the γ (austenite) transforms to ε (martensite) by a faulting mechanism from ABCABC… (fcc) to ABABAB… (hcp) stacking, promoted by hydrogen via the reduction in the stacking fault energy (SFE) of austenite. Figure 2.8 illustrate the structure of conventional stacking faults in the fcc lattice. A normal ABC stacking sequence

of the fcc close packed planes can be seen in Figure 2.8(a). Figure 2.8(b) represents the intrinsic fault that can be formed by the motion of a single Shockley partial dislocation on a close packed plane; this dislocation produces on every second plane a bulk hcp crystal. Thus an intrinsic stacking fault is an hcp embryo. Extrinsic dislocation is shown in Figure 2.8(c). This fault can be generated by the motion of Shockley partial dislocation on two consecutive close packed planes producing a twin, it can be concluded that this fault is a twin embryo.

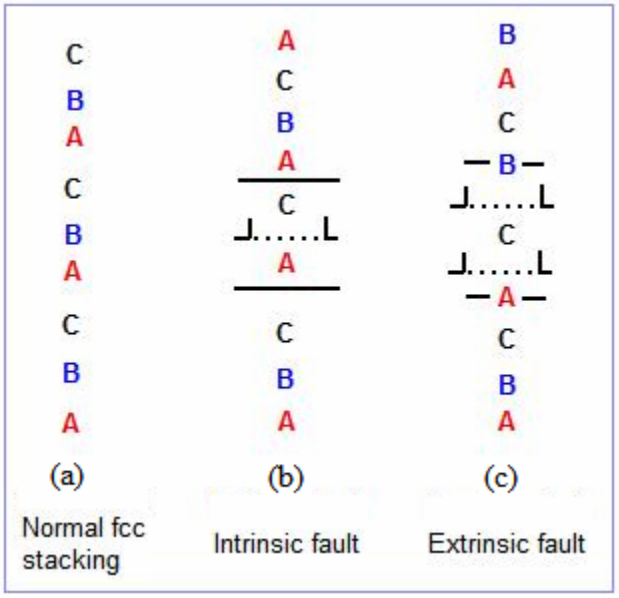

Figure 2.8 Schematics of fcc stacking fault sequence (SFE) for close packed planes [46]

The basic principles of the SFE are based on the following relationship:

$$n = xm \qquad \textbf{2.13}$$

Where x is the number of planes by which one dislocation moves to produce a bulk structure, m is the number of dislocations, and n is the embryo thickness produced by m dislocations. This means for example in Figure 2.8(b), that intrinsic stacking fault is an hcp embryo with 2 planes in thickness (n=2).

An illustration of the transformation mechanism is presented in Figure 2.9 [1, 46]:

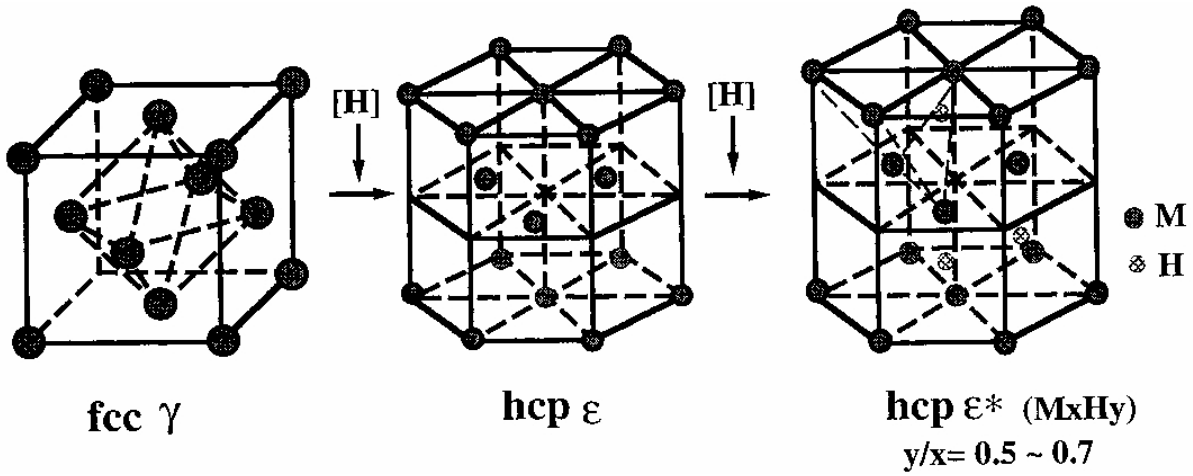

Figure 2.9 Schematics of phase transformation and hydride formation during charging

Verification of formation of hydride phases by examining the XRD data of possible metal-hydride contents in the AISI-321SS austenitic stainless steel is one of the main purposes of the current research. As also verify stacking fault contribution to XRD.

3 MATERIALS AND EXPERIMENTAL TECHNIQUES

3.1 Material Description

Experiments were performed on commercial AISI-321SS austenitic stainless steel type. The as-received material for this study was a 36 by 12 cm cold-rolled foil with a thickness of 50μm. Mean composition of the AISI-321SS type [51] is shown in Table 3.1. AF1410 type steel probes employed also during permeation experiments were in a cold rolled condition extracted from a 7x3.5cm sheet with thickness of 1mm.

TABLE 3.1 Mean composition of AISI 321 Stainless Steel

Carbon	0.08 max.
Manganese	2.00 max
Phosphorus	0.045 max.
Sulfur	0.030 max.
Silicon	0.75 max
Chromium	17.00 – 19.00
Nickel	9.00 – 12.00
Titanium	5 x (C + N) min. 0.70 max
Nitrogen	0.10 max
Iron	Balance

3.2 Material and Sample Preparation

AISI-321 Stainless Steel – Permeation Samples: A set of coupons measuring 2.5x2.5cm were cut from the original cold rolled foil along the same direction, taking into consideration the orientation for all the samples, as shown in Figure 3.1. The advantage of this precaution in the samples was to eliminate the effect of texture of grains due to rolling, as this can affect the diffraction patterns when characterizing the samples by x-ray diffraction measurements.

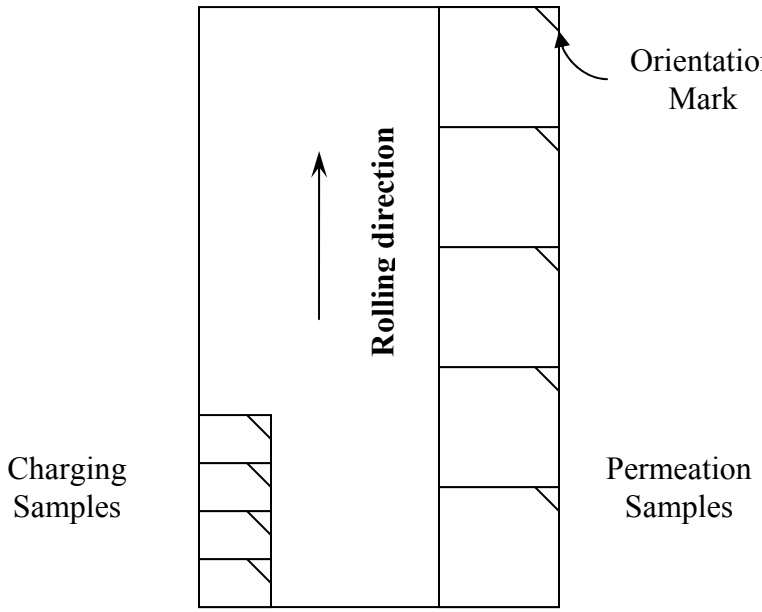

Figure 3.1 Coupon-like samples. Cuts made from the as-received cold rolled sheet

Even though the samples measured 2.5cm by 2.5cm, the effective exposed area to the electrolyte was 1.89cm^2 in the case of the permeation experiments. The remaining area was attached to the working electrode of the potentiostat as shown in Figure 3.3b.

The samples were prepared following careful polishing operation made possible by the use of 600, 800 and 1200 grit paper successively. After obtaining a mirror-like finish on either side (Figure 3.4a), samples were rinsed in ethanol to prevent oxidation of the surfaces and finally stored in desiccators. Prior to every permeation or charging experiment, samples were rinsed in ethanol and blow air dried. As seen in Figure 3.2, heat treatment of as-received samples was carried out in a quartz vacuum ampoule to prevent oxidation of the steel. In order to eliminate remaining traces of oxygen molecules from the ampoule, a titanium sponge was placed inside. Samples were heat treated at 950˚C for a period of 8 hours with subsequent water quenching at room temperature. The purpose of this treatment was to reduce the texture condition of the sample

Figure 3.2 Quartz vacuum ampoule employed for AISI321 samples heat treatment

AF1410 – probe samples: Pairs of samples of 2.5x3.5 cm were cut from a 7x3.5cm slab with initial thickness of 1mm. Grinding of both sides of the samples was made by using the following grit papers 60, 120, 320, 400, 600, 800, 1200 respectively, followed by a polish with 0.05μ alumina suspension with CHEMOMET cloths. Continuous rinses with ethanol and blow air drying stages were made to prevent oxidation of the surface.

3.3 Permeation

3.3.1 Set up and Equipment

The experimental technique of hydrogen permeation was achieved by means of a custom made Devanathan & Stachurski (DS) twin double cell. This double cell with a capacity of 200ml of electrolyte, was made of Teflon with a central orifice of 1.89cm^2 surrounded with elastomer O-rings for sealing. Inert platinum (Pt) rods were used as counter electrodes together with Ag/AgCl reference electrode on the exit side. An acid electrolyte of 0.1M H_2SO_4 with pH 3 impregnated with a promoter of 1g/l Na_2HAsO_4-$7H_2O$ was used in the entry side of the DS setup. The main function of the promoter was to accelerate the permeation process. On the other hand, the environment in the exit side was composed of a base electrolyte of 0.1M NaOH with a pH 13 acting as an oxidation agent for desorbed hydrogen. This base environment also prevented corrosion at the exit side of the membrane.

The experimental setup for hydrogen permeation is shown in Figure 3.3.

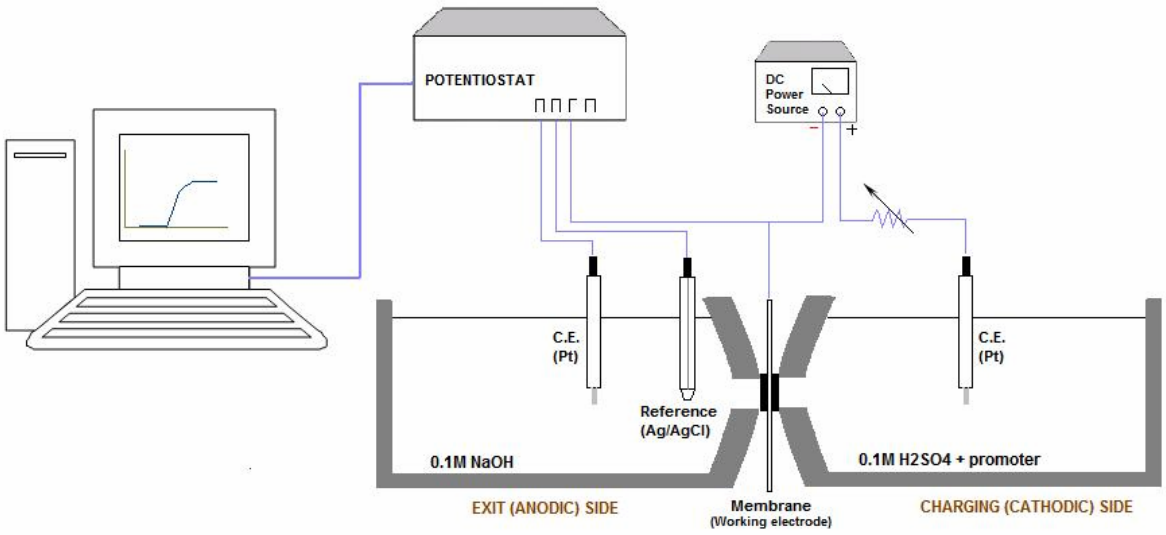

Figure 3.3 Schematics of a Devanathan-Stachurski (DS) cell for hydrogen permeation

Figure 3.4b shows the entry (cathodic) side of the membrane (steel sample), attached to an alligator clip. a coupon-like sample attached to a copper wire after a for 24 hours permeation with a 200mA current charging. The portion exposed to the electrolytic media exhibited a distortion on the surface (charging side). The permeated sample was found to be blunt or corrugated like (i.e., distorted) at the end of every permeation experiment.

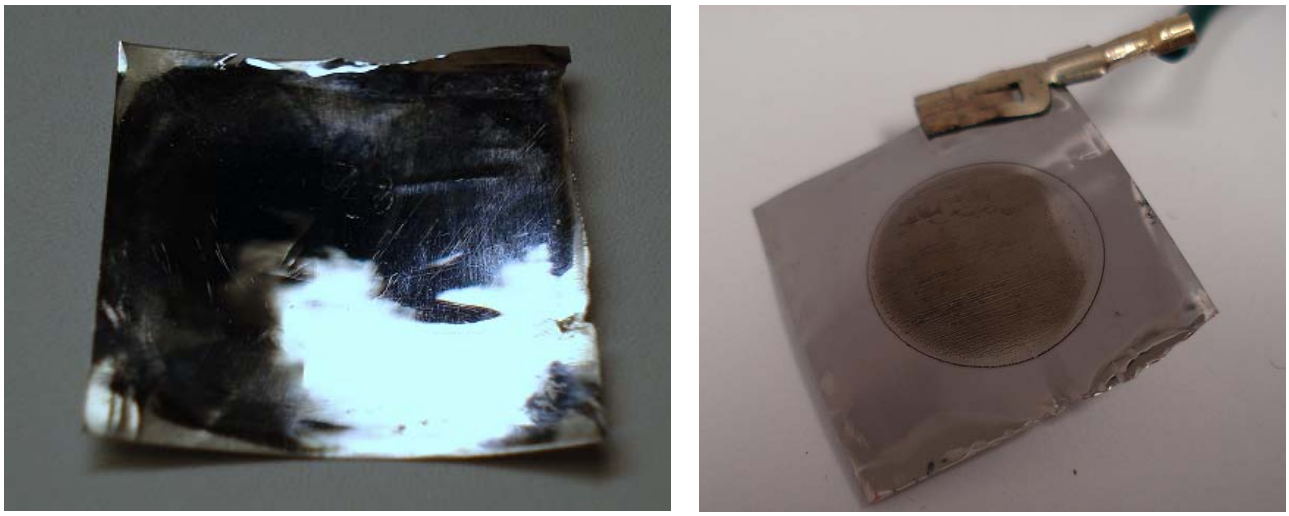

(a) **(b)**

Figure 3.4 AISI-321SS type steel. (a) Polished coupon-like sample prior to permeation. (b) Sample after hydrogen permeation under 200mA current charging

Hydrogen charging was carried out by a DC power supply (Hewlett Packard 6216C). A variable resistance (RS200 JET) was employed to control the current necessary for permeation. A potentiostat (Solartron 1280) was used in the extraction side to maintain and control the voltage between the working electrode, in this case the AISI-321 membrane, and the reference electrode (Ag/AgCl) to a constant value.

The software used for data acquisition and analysis was CorrWare. This software also controlled the potentiostat and was able to perform at different conditions such as the potentiostatic, potentiodynamic and galvanostatic modes. For the study of permeation on the AISI-321SS type Stainless Steel, the potentiostatic mode was employed.

Samples were characterized by x-ray diffraction measurements with a Siemens D500 Diffractometer shown in Figure 3.5 which was operated with a Cu Kα radiation at 30kV and 35mA. Measurements were made from $10° \geq 2\theta \leq 110°$ using step angles of 0.02 for 1 second.

Figure 3.5 Siemens Diffractometer D-500 employed during X-ray characterization

3.3.2 Permeation Procedure

The hydrogen permeation of hydrogen in an AISI-321SS foil was done by combining the classical Devanathan-Stachurski method [26, 38, 42, 47] with electrochemical potentiostatic condition at room temperature. Previously polished samples (membrane) were rinsed in ethanol and mounted between the cells. Both cells were equipped with platinum rods as counter electrodes (C.E.), and with a reference electrode of silver/silver chloride (Ag/AgCl). The potential on the oxidation cell was set to 0.3V with respect to reference electrode. Upon

attaining a low stable background current typically in the range of 1μA/cm^2 (at the exit side), the charging current was set to a desired value to let the hydrogen evolve cathodically on the entry side of the membrane in a 0.1M H_2SO_4 solution, impregnated with a promoter of 1g/l of sodium arsenate (Na_2HAsO_4-$7H_2O$). The permeated hydrogen was oxidized at the exit side in a 0.1M NaOH solution. Tests were carried out independently by galvanostatic method for 100mA, 150mA, 200mA, 250mA, 300mA 350mA and 400mA charging current by controlling the power supply at the entry side. The observed permeation current, *J,* for each experiment, was a direct measurement of the overall permeation kinetics. The units employed during galvanostatic charging of samples (as-received, heat treated, and polished) are expressed in current (mA) and not in current density (mA/cm^2); therefore it is advisable to divide the charging currents by 1.89cm^2 to convert the current to current density. The values obtained during permeation experiments at anodic cell (exit side) controlled by the Potentiostat are expressed conveniently in units of current density.

3.3.3 Desorption of Charged Samples

The process of desorption was meant to show the release of hydrogen from the membrane when the charging potential was interrupted, and the concentration at the entry side set to zero. Once the permeation process has attained a steady state current *(J_∞)*, the charging current (power source) was stopped. Desorption of hydrogen was then calculated on either side of the membrane. When desorption at the exit side was calculated, the solution at the

cathodic cell (entry side) has to be removed and the membrane flushed with ethanol to avoid further corrosion; at the same time, the potentiostat still continues to record the hydrogen leaving the sample. Once the experiment was over, flushing the sample with ethanol on both sides of the membrane was always necessary. Finally the entry side was filled with a solution of 0.1M NaOH with the counter and reference electrodes set as shown in Figure 3.3. The potentiostat was then allowed to record the desorbing hydrogen.

3.4 Characterization of Charged Samples

X-ray diffraction measurements were carried out immediately in order to characterize both sides of the membrane, after each experiment once a steady state current was achieved. Diffraction patterns were analyzed in order to correlate the charging conditions with the decomposition of the AISI-321SS steel, and to identify the resulting induced phases. For the x-ray diffraction data analyses, computing and elimination of the background noises were necessary. In addition, scanning electron microscopy (SEM) was performed on charged and 15 days room temperature aged samples in order to study the surface morphology.

4 RESULTS AND DISCUSSIONS

Previous tests on AF1410 were made before charging the AISI-321SS type steel. A sample of high-strength steel of AF1410 was charged under potentiostatic condition with a current density close to the ones used for the AISI-321SS type steel in order to effectuate base reference comparison. The corresponding permeation profile for a 1mm thick sample charged at 50mA is shown in Figure 4.1

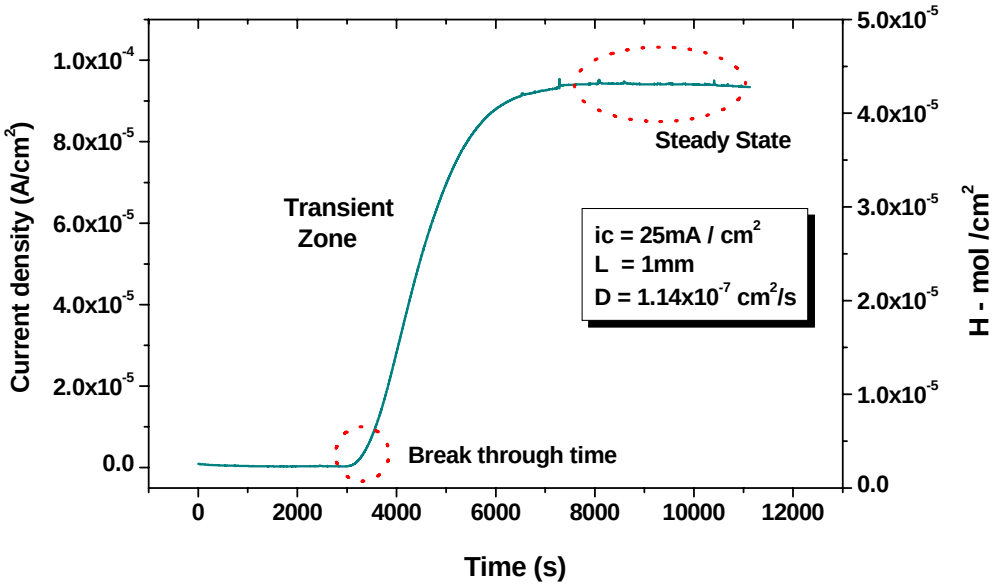

Figure 4.1 Typical sigmoidal shape of a complete permeation experiment. As-received AF1410 with charging current of 50mA

A typical sigmoid-shaped permeation profile is shown in Figure 4.1. It can be noticed that the steady state fraction of the profile is equivalent to a peak permeation point, and so the amount of permeated hydrogen can be related directly to the amount of charging current density employed when the sample is cathodically charged.

4.1 Hydrogen Permeation on as-received AISI-321 Austenitic Stainless Steel Samples

4.1.1 Hydrogen Permeation Profile, Peak Permeation and Stabilization Times

Different currents ranging from 100mA to 400mA were employed on the entry cell using a solution of 0.1M H_2SO_4 + 1g/l Na_2HAsO_4-$7H_2O$ to charge AISI-321 austenitic stainless steel type samples under galvanostatic condition (constant current). The time to attain a current background of 1μA/cm^2 in the alkaline solution (0.1M NaOH) on the exit cell under constant potential of 0.3V with respect to Ag/AgCl reference electrode varied approximately from 5000 to 10000 seconds. This background current was generally accepted as a standard [2, 3, 37] for permeation experiments in metallic materials. In order to induce the permeation process, introduction of the acid electrolyte was necessary after achieving the required background current. Similar breakthrough times were experienced prior to the commencement of the transient zone for the as-received material; this is shown in Table 4.1. Figure 4.2 to Figure 4.8 correspond to different permeation profiles set that were run for a period of 24 hours.

TABLE 4.1 Summary of breakthrough times with different current charging

Charging current (mA/)	100†	150†	200†	250†	300†	350†	400†
Break Through time (t_b) (S)	10	10	10	10	10	10	10

†Charging Time = 24hours

Rapid increase in the transient zone was observed after 10 seconds of cathodic polarization (charging) followed by a steady state region. Experimental results show a continuous current drop until stabilization condition. In contrast, different results of breakthrough time and times to achieve steady state were reported by Charca-Mamani [42] for different charging conditions on samples of AF1410 steel. Relationship between the breakthrough time (t_b) values, time to achieve steady state (t_{ss}) and the polarization current densities employed in the present study as obtained by the author can be seen in Table 4.2.

TABLE 4.2 Summary of breakthrough times and steady state for different current densities for AF1410

T_b (sec)	**T_{ss}(sec)**	**Current (mA/cm^2)**
5000	16000	1
4010	15000	2
3000	13000	3
2000	12000	6
2000	11000	10

From Figure 4.2 through Figure 4.8 is it possible to observe that the peak permeation value was a function of the polarization current density employed, as it increased with increasing value of the latter.

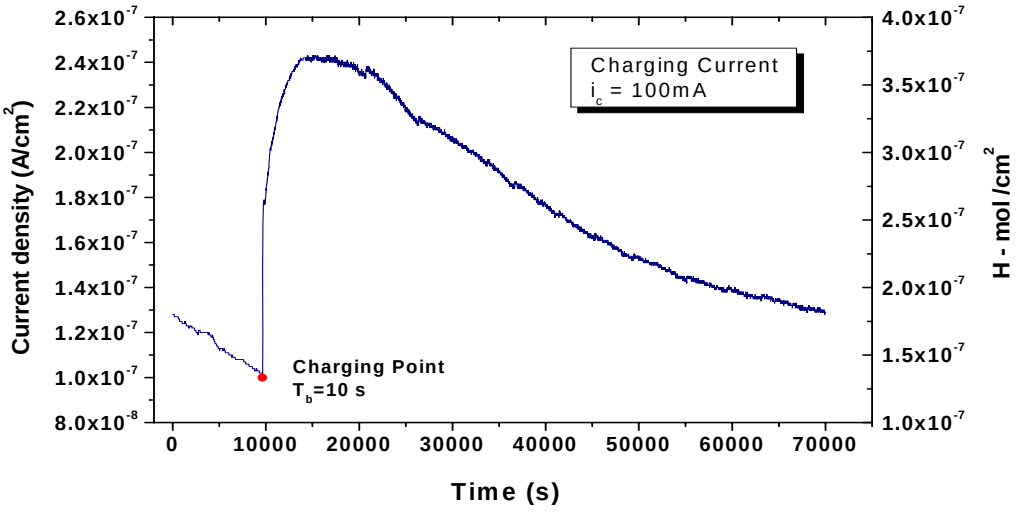

(a)

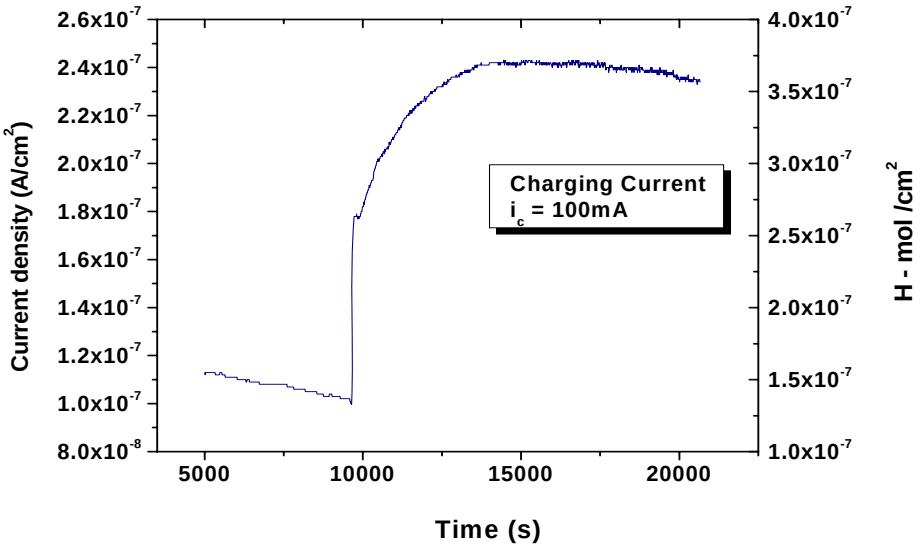

(b)

Figure 4.2 Hydrogen permeation profile for a 100mA current charging of as-received sample. (a) Complete hydrogen permeation profile, (b) Detailed portion of transient and steady state profile

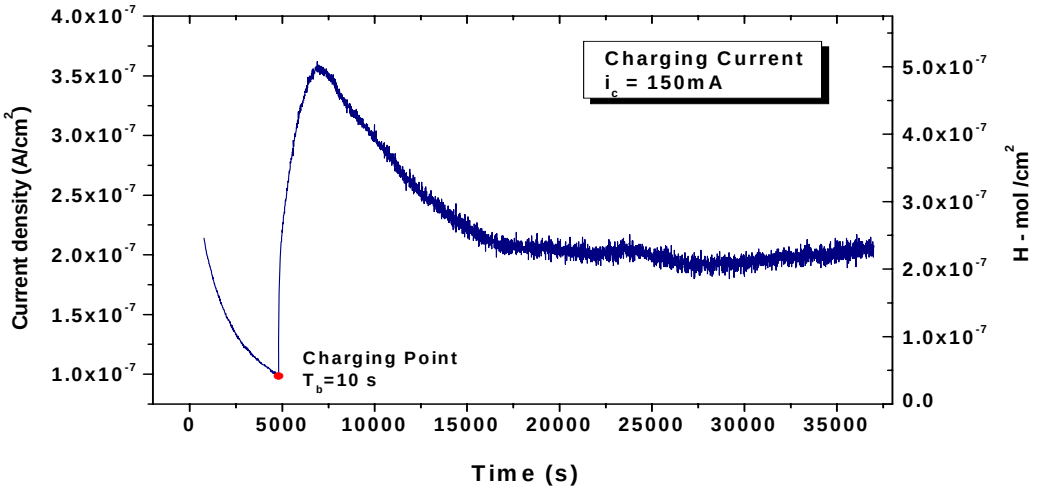

(a)

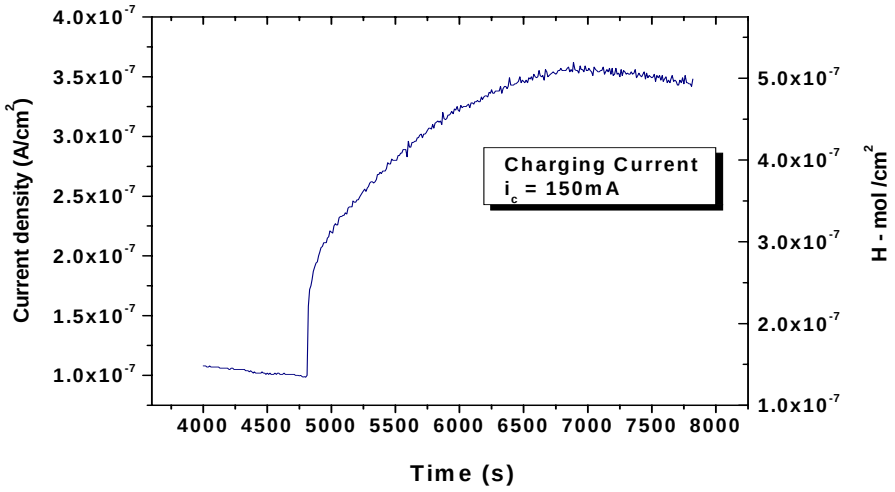

(b)

Figure 4.3 Hydrogen permeation profile for a 150mA current charging of as-received sample. (a) Complete hydrogen permeation profile, (b) Detailed portion of transient and steady state profile

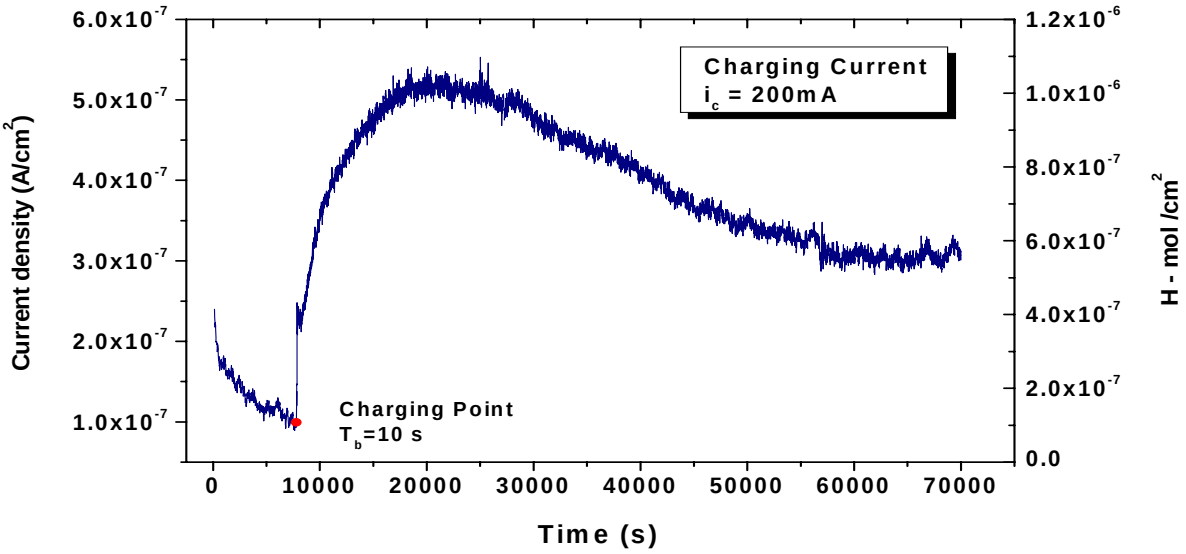

(a)

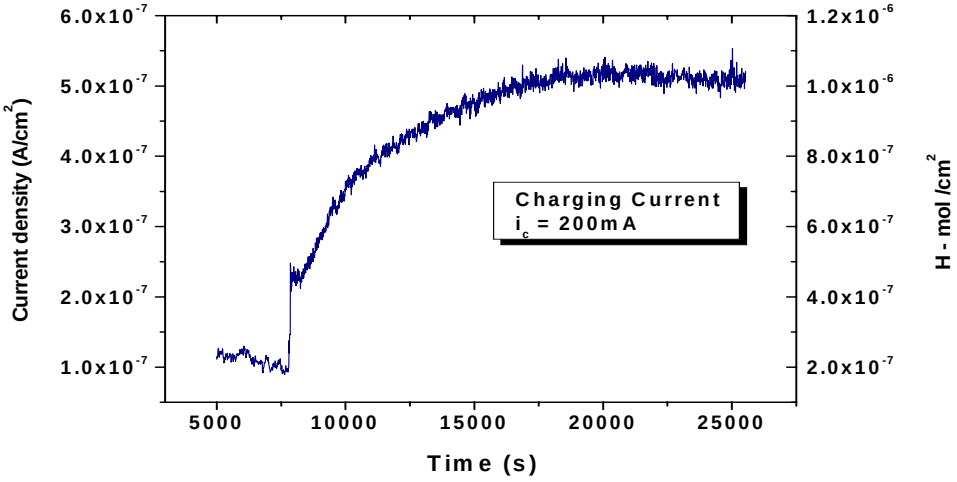

(b)

Figure 4.4 Hydrogen permeation profile for a 200mA current charging of as-received sample. (a) Complete hydrogen permeation profile, (b) Detailed portion of transient and steady state profile

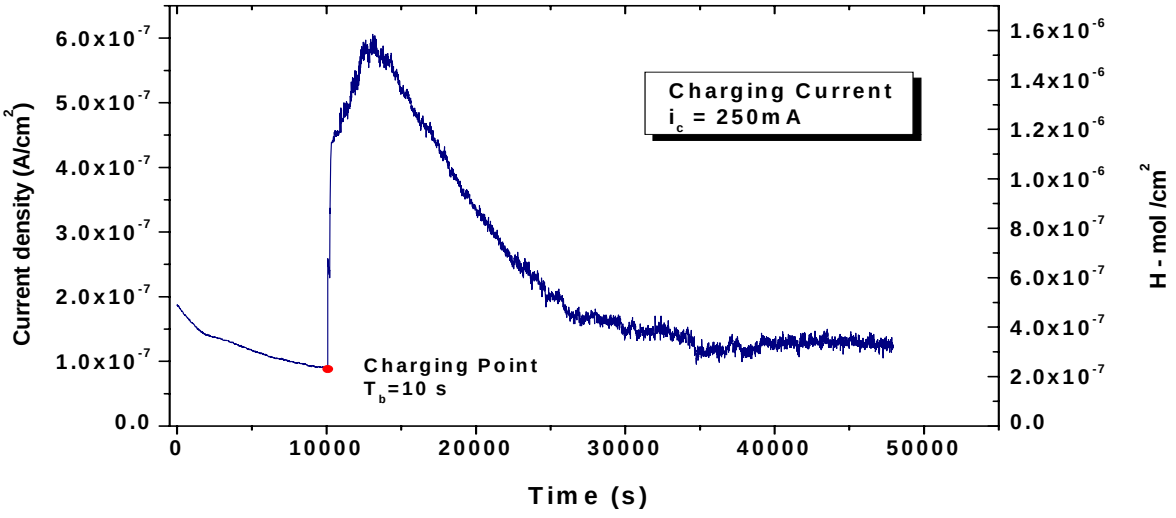

(a)

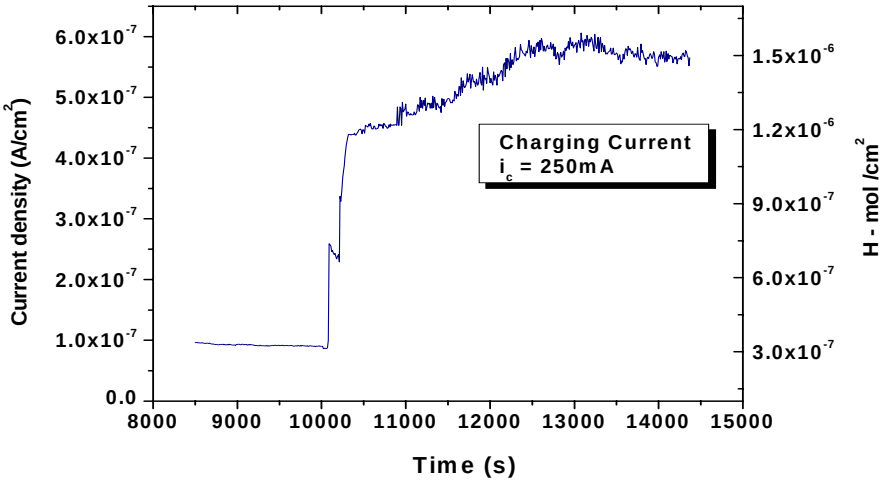

(b)

Figure 4.5 Hydrogen permeation profile for a 250mA current charging of as-received sample. (a) Complete hydrogen permeation profile, (b) Detailed portion of transient and steady state profile

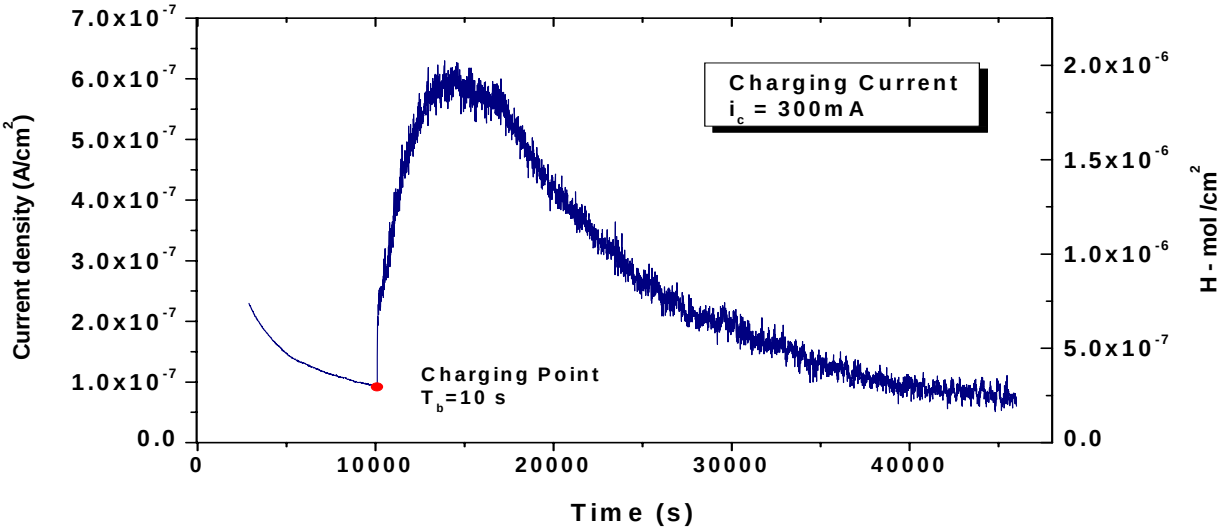

(a)

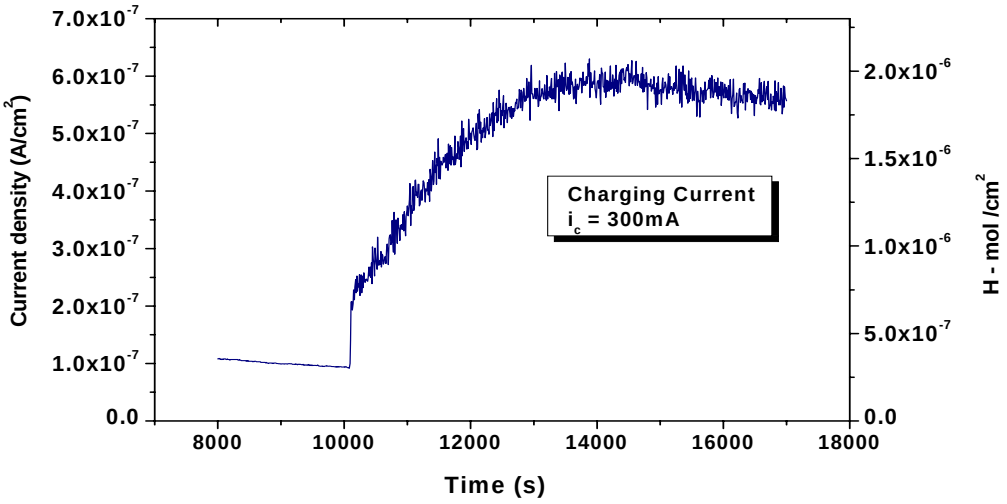

(b)

Figure 4.6 Hydrogen permeation profile for a 300mA current charging of as-received sample. (a) Complete hydrogen permeation profile, (b) Detailed portion of transient and steady state profile

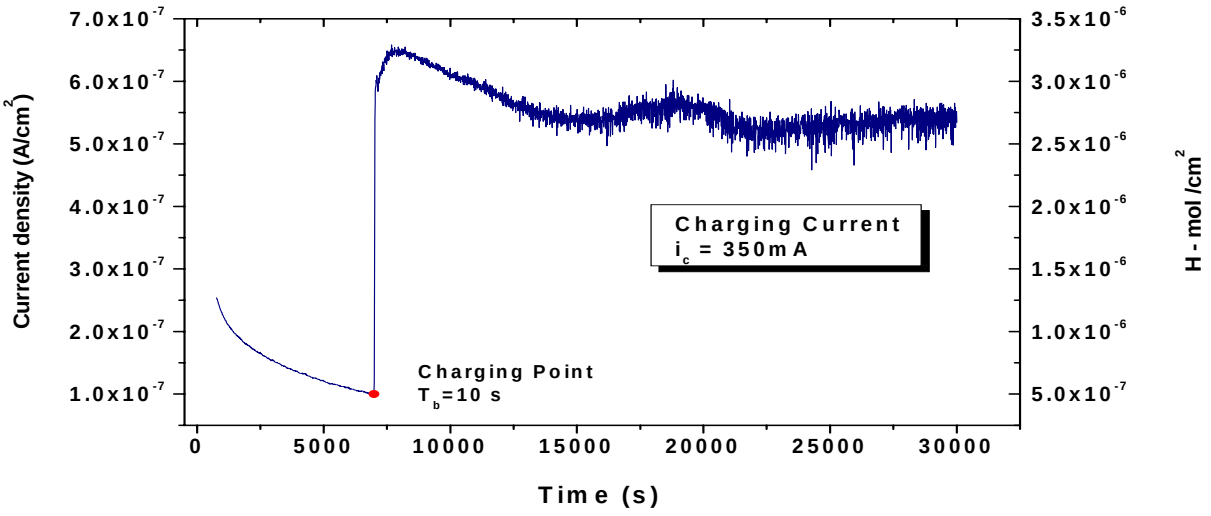

(a)

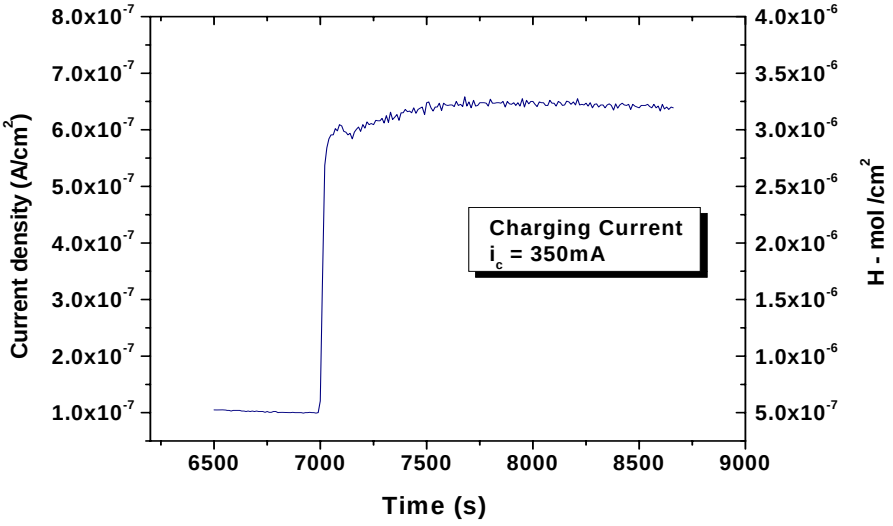

(b)

Figure 4.7 Hydrogen permeation profile for a 350mA current charging of as-received sample. (a) Complete hydrogen permeation profile, (b) Detailed portion of transient and steady state profile

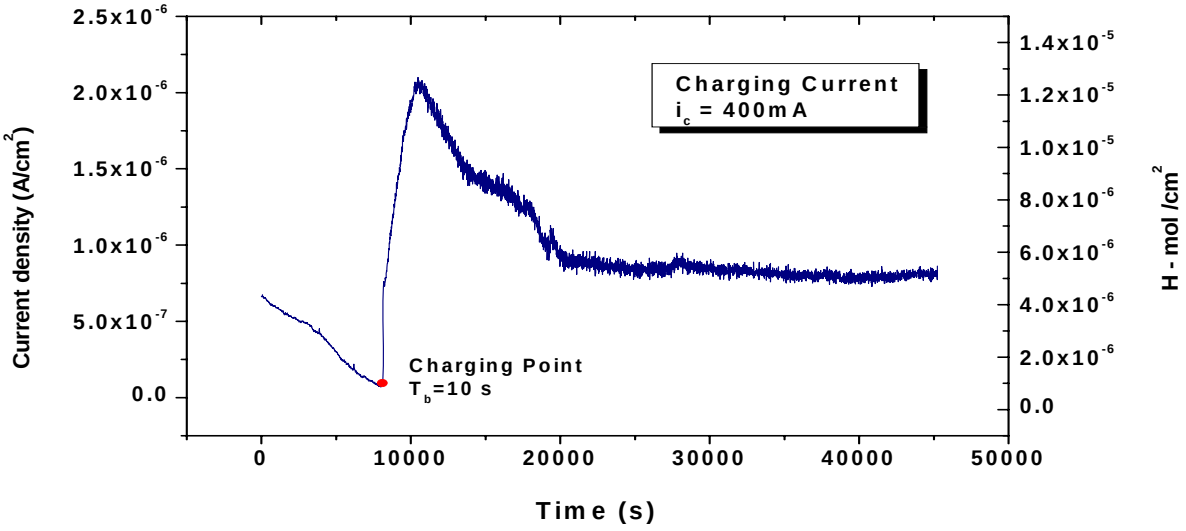

(a)

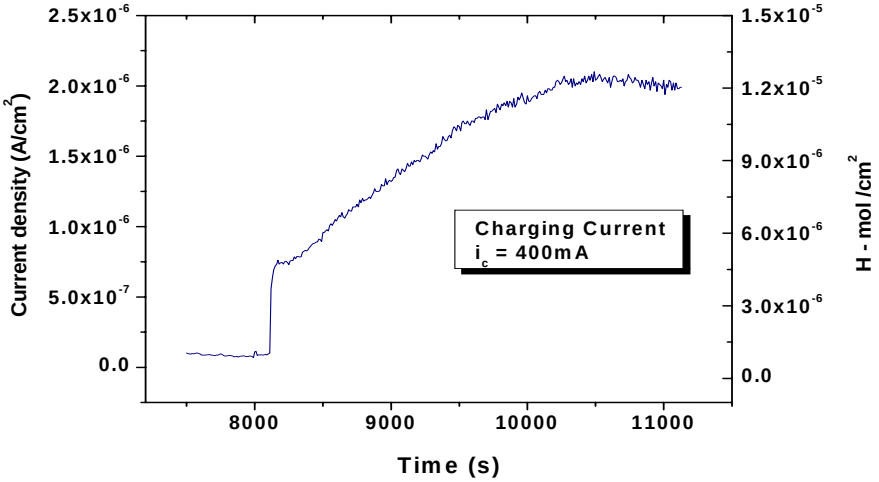

(b)

Figure 4.8 Hydrogen permeation profile for a 400mA current charging of as-received sample. (a) Complete hydrogen permeation profile, (b) Detailed portion of transient and steady state profile

4.1.2 Electrochemical Determination of Hydrogen Diffusivity and Concentration

As shown in Section 2.4, several methods could be employed to determine the diffusion coefficient [38]. The most common methods are the slope, breakthrough time, and time lag. Values summarized in Table 4.1 show similar breakthrough times (t_b) independent of the charging current employed for the permeation experiments. This is a huge disadvantage for the method since finding the apparent diffusivity values with similar t_b times resulted in equal permeation coefficients as seen in Table 4.3. The lag method also presented a main disadvantage since it has no theoretical basis due to the sharpness of the permeation transients that indicated a changing diffusivity with time; that explains why, the time lag method should be used as an empirical estimation of the permeation coefficient (D). The permeation coefficient parameter adapted in this work was calculated based on the slope method as indicated by ASTM G-148-97 standard. The apparent diffusivity can be calculated from the slope of a plot of log ($| J_\infty - J(t) |$) in the vertical coordinate Vs. 1/t in the horizontal axis. The result gives a linear plot whose slope corresponds to $L^2 \log(e) / 4D$. The remaining methods are explained in the Appendix A.1. The summary of values of the diffusion coefficient corresponding to hydrogen permeation obtained using different currents can be seen in Table 4.3.

An example of the determination of the apparent diffusivity (D) of hydrogen in the AISI-316 austenitic stainless steels was done by Zakroczymski et al. [2]. The author employed the experimental data analyses from build –up transients to find the diffusivity values. Experiments on the 316 type steel showed the expansion of the austenite phase (lattice expansion). The obtained coefficient of diffusion for the 316 type steel was $D=1.70 \times 10^{-12}$ cm^2/s.

TABLE 4.3 Summary of permeation coefficient by slope and breakthrough time method for as-received samples

Cathodic Charging Current (i_c, mA)	*Slope Method* Apparent diffusion (D, cm^2/s) $x10^{-11}$	(t_b,s)	*Breakthrough Time Method* Apparent diffusion (D_{app}, cm^2/s) $x10^{-7}$
100	9.22	10	1.63
150	9.15	10	1.63
200	6.48	10	1.63
250	4.95	10	1.63
300	3.93	10	1.63
350	2.41	10	1.63
400	1.98	10	1.63

Zakroczymski et al [3, 27] demonstrated mathematically that the fraction of hydrogen diffusing out of the membrane (exit side, $X = L$) is 1/3, while the fraction of hydrogen diffusing out at the charging side (entry side, $X = 0$) is 2/3 under galvanostatic charging condition. The final amounts of hydrogen can be obtained by integrating Equations 2.11 and 2.12 with respect to time to obtain the amount of hydrogen leaving the metallic membrane at the exit side ($\boldsymbol{q}_{H,L}$) and entry side($\boldsymbol{q}_{H,0}$), as seen in Equation 4.1 and 4.2:

$$q_{H,L} = \frac{j_H^0 L^2}{6DF} \qquad \text{H-mol/cm}^2 \qquad \textbf{4.1}$$

$$q_{H,0} = \frac{j_H^0 L^2}{3DF} \qquad \text{H-mol/cm}^2 \qquad \textbf{4.2}$$

Where J^0_H is the initial steady state of hydrogen recorded experimentally, L equals the membrane thickness, D is the apparent diffusion value and F is the Faraday constant. Hence, the total amount of hydrogen stored in the material before charging interruption, is represented by the addition of equation 4.1 and 4.2 as follows:

$$q_{H,TOTAL} = q_{H,L} + q_{H,0} = \frac{j_H^0 L^2}{2DF} \qquad \text{H-mol/cm}^2 \qquad \textbf{4.3}$$

Table 4.4 summarizes the calculated diffusible hydrogen at the entry and exit side and the total amount of hydrogen stored in the metallic membrane. Another important aspect is the subsurface hydrogen concentration (C_o) at the entry side. Steady state permeation current (j_H^0) gives information about the subsurface concentration from the relationship, $j_H^0 = FDC_0/L$ expressed in units of current density, which is governed by Fick's first law. Thus, solving for C_0 gives Equation 4.4:

$$C_0 = \frac{j_H^0 L}{DF} \qquad \text{H-mol/cm}^3 \qquad \textbf{4.4}$$

TABLE 4.4 Diffusible hydrogen and subsurface concentration at different charging current on as-received samples

Cathodic Charging Current (i_c, mA)	**Subsurface Concentration, (Co) *[H]-mol/ cm^3*** **(D, slope method)**	***Diffusible Hydrogen [H]/ mol cm^{-2}***		**$q_{H,\ total}$ = (Entry Side + Exit Side) *[H]-mol cm^{-2}***
		Entry Side (X=0)	*Exit Side (X=L)*	
100	1.51×10^{-4}	2.50×10^{-7}	1.25×10^{-7}	3.75×10^{-7}
150	1.77×10^{-4}	3.42×10^{-7}	1.71×10^{-7}	5.12×10^{-7}
200	3.91×10^{-4}	7.19×10^{-7}	3.60×10^{-7}	1.08×10^{-6}
250	6.03×10^{-4}	1.05×10^{-6}	5.27×10^{-7}	1.58×10^{-6}
300	1.09×10^{-3}	1.91×10^{-6}	9.52×10^{-7}	2.87×10^{-6}
350	1.41×10^{-3}	2.36×10^{-6}	1.18×10^{-6}	3.54×10^{-6}
400	5.50×10^{-3}	9.14×10^{-6}	4.50×10^{-6}	1.36×10^{-5}

As seen in the profiles of Figures 4.9a and 4.9b, the trend of the hydrogen amount and subsurface concentration for permeated samples increases with increasing polarization or current charging. Based on the experimental permeation profiles for as-received samples, the diffusivity for the stainless steel AISI-321SS was found to be very low [2]; this indicated that accumulation of hydrogen laid beneath the surface layer and not a huge amount reside in the bulk. The value of the apparent diffusion decreased with higher current densities mainly because higher currents promoted faster hydrogen evolution at the surface in the electrolyte than lower ones. This occurrence augmented rapidly the quantity of subsurface hydrogen concentration in the sample and as a consequence, slowing down the permeation rate through the bulk material.

It is possible to see the contrast of the plot of diffusivity against the subsurface concentration in Figure 4.10. As was shown in chapter 1, the AISI-321SS austenitic stainless steel was designed to withstand acid and corrosive environments; that is why the protective coating of the as-received samples should be taken also in consideration for registering low diffusivity values. Hydrogen diffusible at the exit side (Table 4.4) also indicated that a small amount of hydrogen permeated the sample as compared with the diffusible amount in the entry side of the material.

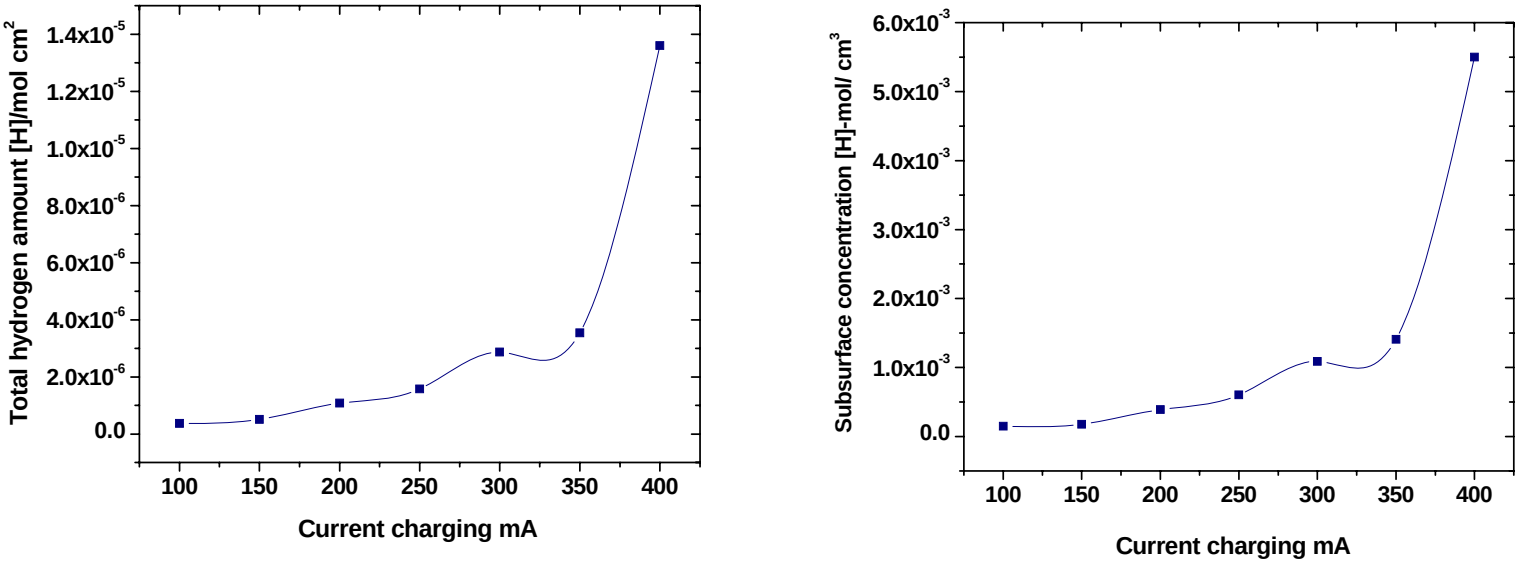

(a) **(b)**

Figure 4.9 Tendency at different current densities on the as-received sample of (a) Total of hydrogen amount. (b) Subsurface concentration.

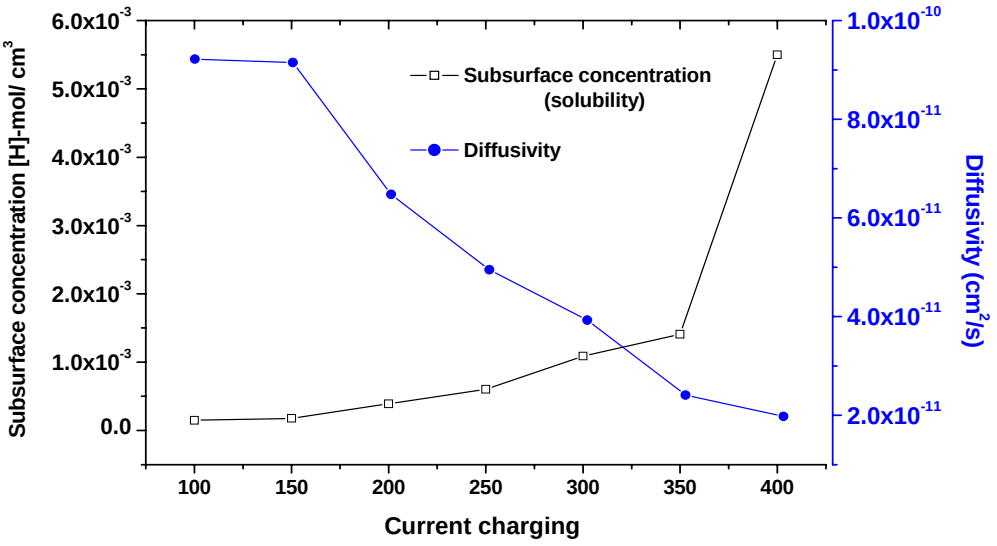

Figure 4.10 Comparison of permeation coefficient values and subsurface concentration as a function of current charging densities for the as-received sample

4.1.3 Effect of Hydrogen Permeation on as-Received Heat Treated Sample

The hydrogen permeation profile obtained for the annealed AISI-321SS stainless steel is presented in Figure 4.17. A typical sigmoid permeation profile (peak permeation, transient and steady state) was obtained followed by a fast hydrogen discharge after 16000 seconds. The sample with initial thickness of L= 0.005cm was heat treated for eight hours at a constant temperature of 950 ˚C in order to obtain a fully annealed state. The calculated diffusivity (D) was obtained by the slope method, and the breakthrough time (t_b) was found to be 10 seconds, similar to the t_b time for the as-received samples. Subsurface concentration

(C_o) was found to be 5.43x10^{-4} Mol-H /cm^3 while the total diffusible hydrogen ($q_{H,\ total}$) was equal to 1.31 x10^{-6} [H]/ mol cm^{-2}. The latter values are summarized in Table 4.5 and Table 4.6.

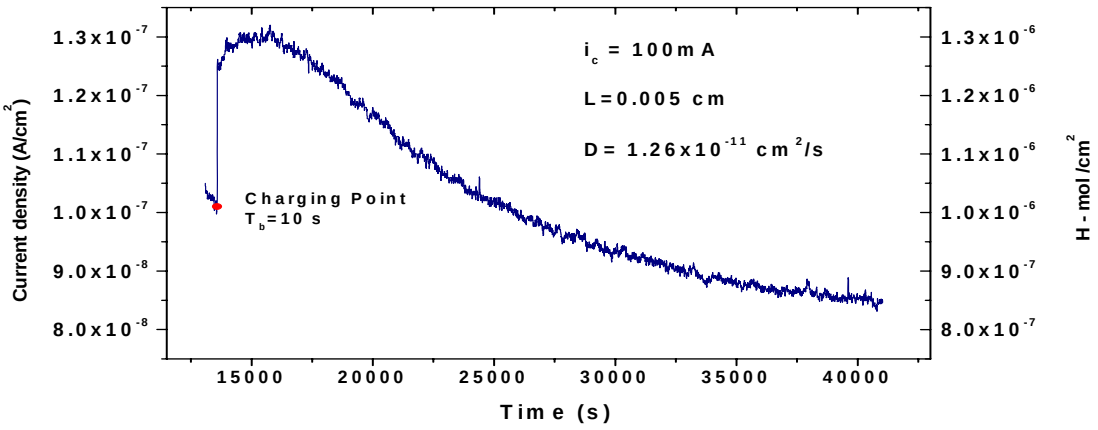

(a)

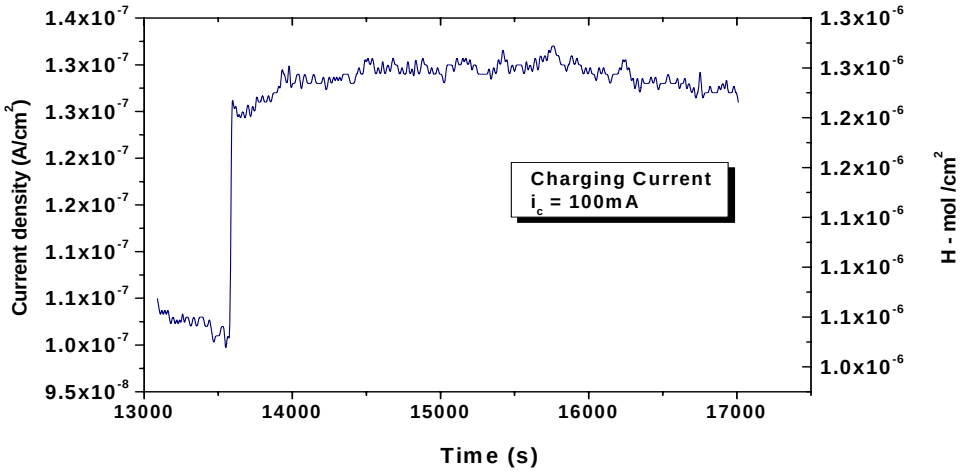

(b)

Figure 4.11 Hydrogen permeation profile for a 100mA current charging of an annealed as-received sample. (a) Complete hydrogen permeation profile, (b) Detailed portion of transient and steady state profile

The annealed treatment did not enhanced the diffusivity of hydrogen, and based on the values obtained for the subsurface concentration, and the diffusible hydrogen on the entry and exit sides of the sample (Table 4.6), indicated that the treated material behaved similar to the non-heat treated ones. The permeation profile found for the annealed sample was analogous to the as-received permeation profiles in section 4.1.1.

TABLE 4.5 Summary of permeation coefficient by slope and breakthrough time method for as-received heat treated sample

Cathodic Charging Current (i_c, mA/cm^2)	***Slope Method***	**(t_b,s)**	***Breakthrough Time Method***
	Apparent diffusion (D, cm^2/s) x10^{-11}		**Apparent diffusion (D, cm^2/s) x10^{-7}**
100	1.26	10	1.63

TABLE 4.6 Diffusible hydrogen and subsurface concentration at 100mA/cm^2 charging current on as-received heat treated sample

Cathodic Charging Current (i_c, mA/cm^2)	**Subsurface Concentration, Co *Mol-H /cm^3* (D, slope method)**	***Diffusible Hydrogen [H]/ mol cm^{-2}***		**$q_{H,\ total}$ = (Entry Side + Exit Side) *[H]/ mol cm^{-2}***
		Entry Side (X=0)	*Exit Side (X=L)*	
100	5.43x10^{-04}	8.71 x10^{-7}	4.36 x10^{-7}	1.31 x10^{-6}

4.2 Hydrogen Permeation on Polished AISI-321SS Austenitic Stainless Steel Samples

4.2.1 Hydrogen Permeation Profile, Peak Permeation and Steady State Permeation

Hydrogen permeation on polished samples was done under the same conditions as described in section 4.1.1. Currents of 100mA to 400mA were employed using the same solution of 0.1M NaOH and 0.1M H_2SO_4 + Na_2HAsO_4-$7H_2O$ under potentiostatic method. The first observation from Figure 4.12 to Figure 4.18 is that the peak permeation values are a function of the polarization current employed, as it increased with increasing values of the latter. It was also found that the time for stabilization of background current ($<<1\mu A/cm^2$) for the polished AISI-321SS austenitic steel was approximately from 5000 to 10500 seconds.

Obtained permeation profiles for polished samples showed a rapid increase in the transient zone, followed by a steady state region after the cathodic polarization has started. This sigmoid-shape profiles occur from 60 to 120 minutes, after that, a continuous desorption of hydrogen occurred. Summary of t_b times to the steady state (t_{ss}) are shown in Table 4.7.

TABLE 4.7 Summary of breakthrough times (t_b) to steady state values (t_{ss}) for desorption profile with different current densities for AISI-321SS

Current Charging (mA/cm^2)	t_b to t_{ss}(sec)	Peak permeation Current (A/cm^2) x 10^{-7}
100	1290	**1.10**
150	1240	**1.20**
200	2080	**1.55**
250	4140	**2.80**
300	5060	**5.70**
350	2080	**3.70**
400	1020	**10.0**

Figure 4.12 to Figure 4.18 contain the permeation profiles for the charging current of 100mA, 150mA, 200mA, 250mA, 300mA, and 350mA respectively. The current densities found in the permeation profiles varied from $1.57x10^{-7}$ A/cm^2 to $6x10^{-7}$ A/cm^2. The intensity of the permeation peak for the experiment done under current charging of 400mA was $1.01x10^{-6}$ A/cm^2 which was by far higher than those from previous experiments. Violent hydrogen evolution was observed during cathodic charging from 300mA to 400mA, in the form of hydrogen bubbles accumulated over the sample's surface (entry side) which effused out of the charging chamber at a rate approximately equal to a single bubble approximately every 5 seconds.

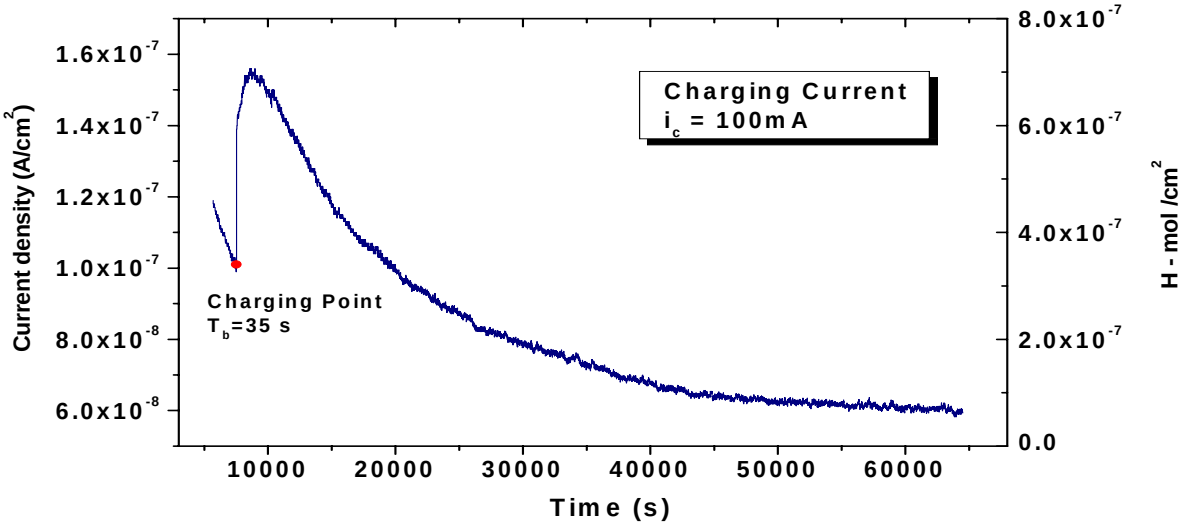

(a)

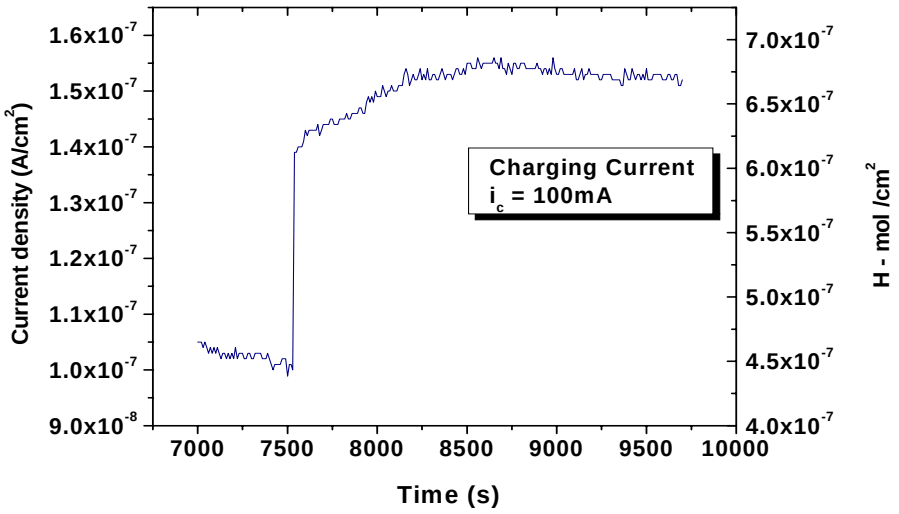

(b)

Figure 4.12 Hydrogen permeation profile for a 100mA current charging of a polished sample. (a) Complete hydrogen permeation profile, (b) Detailed portion of transient and steady state profile

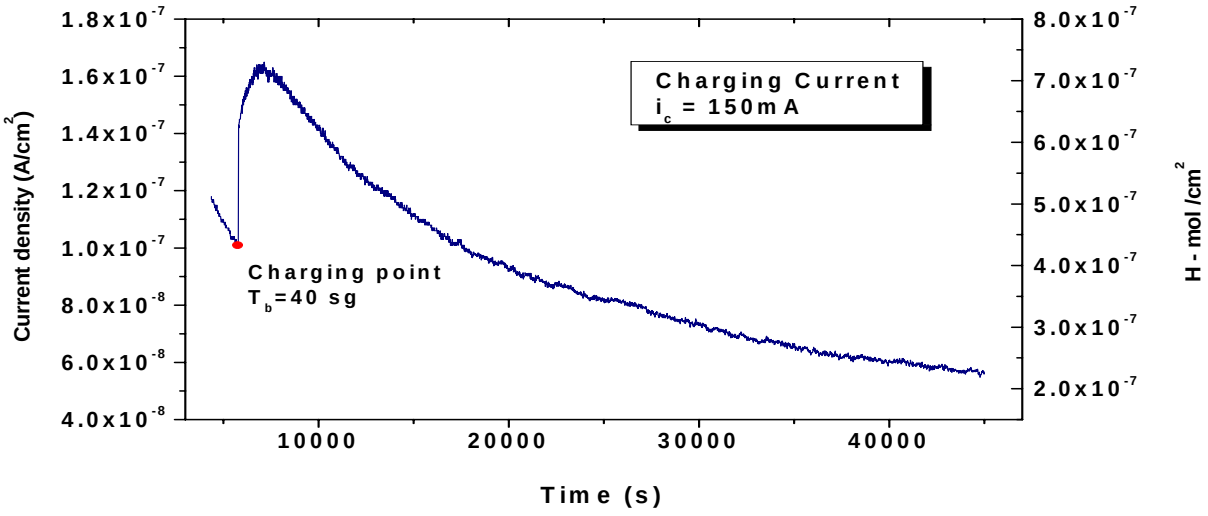

(a)

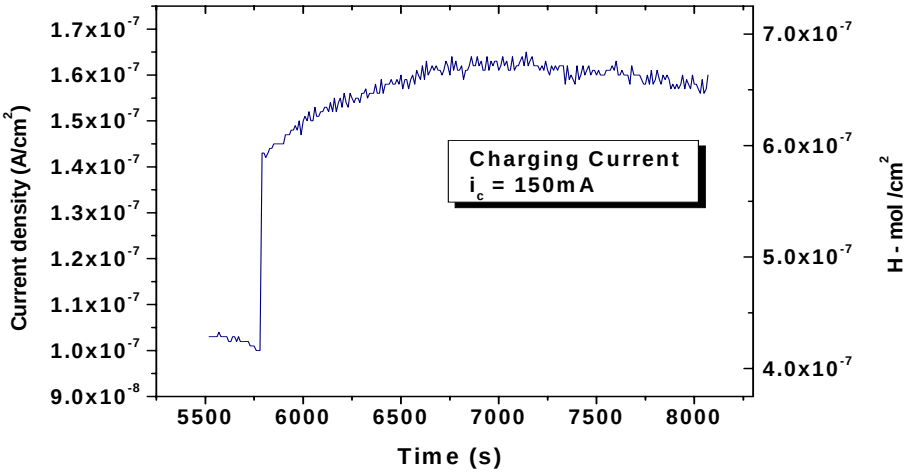

(b)

Figure 4.13 Hydrogen permeation profile for a 150mA current charging of a polished sample. (a) Complete hydrogen permeation profile, (b) Detailed portion of transient and steady state profile

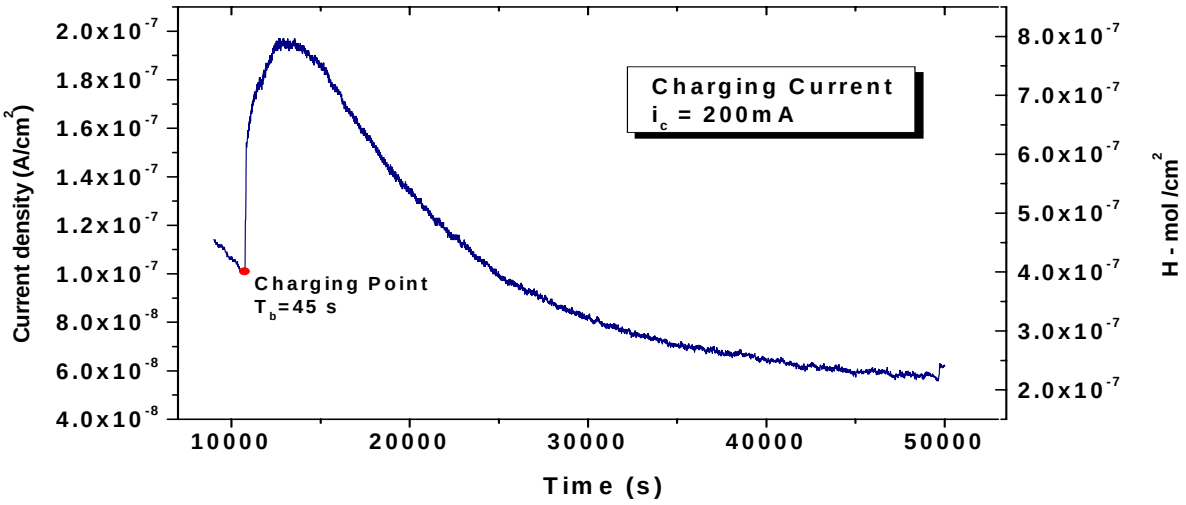

(a)

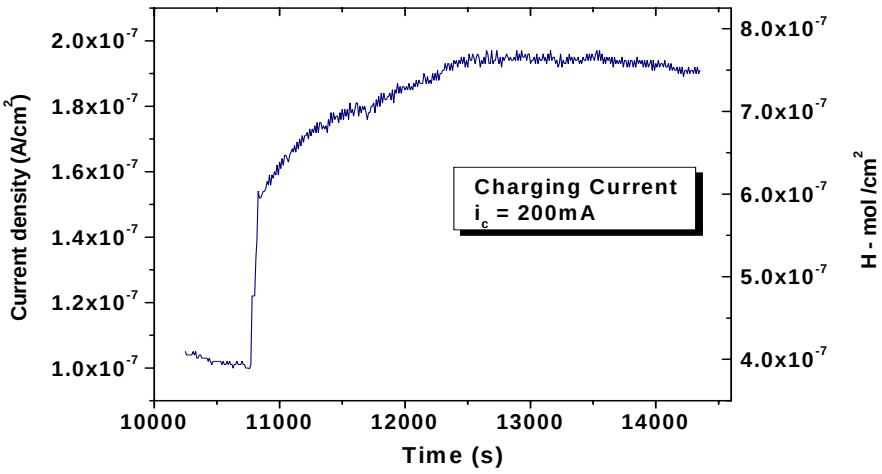

(b)

Figure 4.14 Hydrogen permeation profile for a 200mA current charging of a polished sample. (a) Complete hydrogen permeation profile, (b) Detailed portion of transient and steady state profile

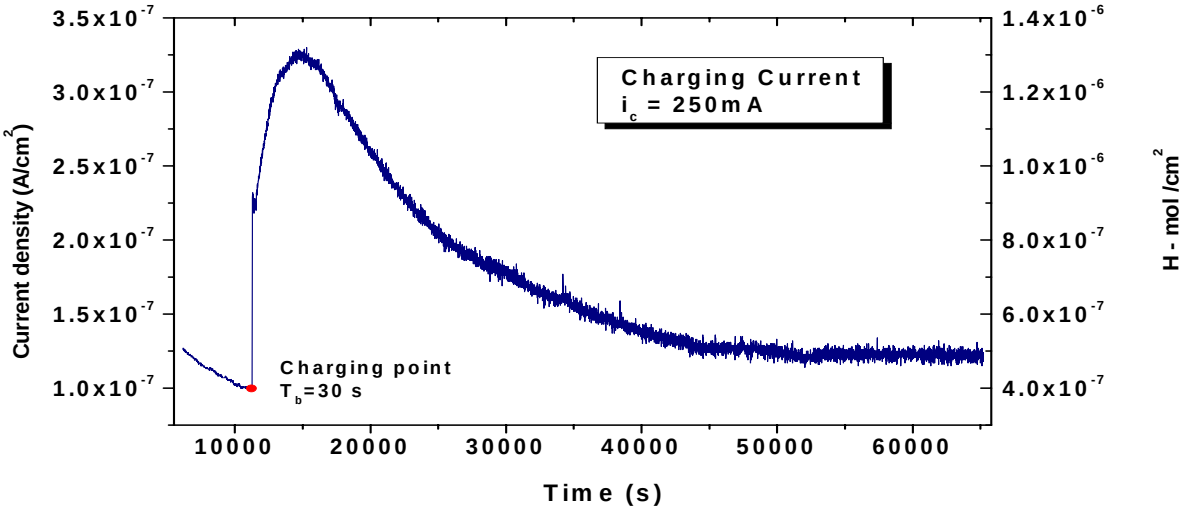

(a)

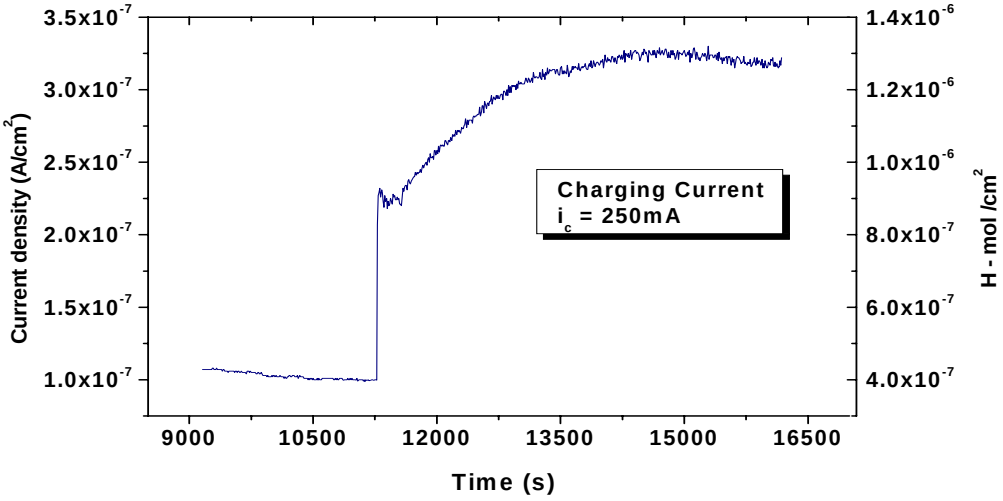

(b)

Figure 4.15 Hydrogen permeation profile for a 250mA current charging of a polished sample. (a) Complete hydrogen permeation profile, (b) Detailed portion of transient and steady state profile

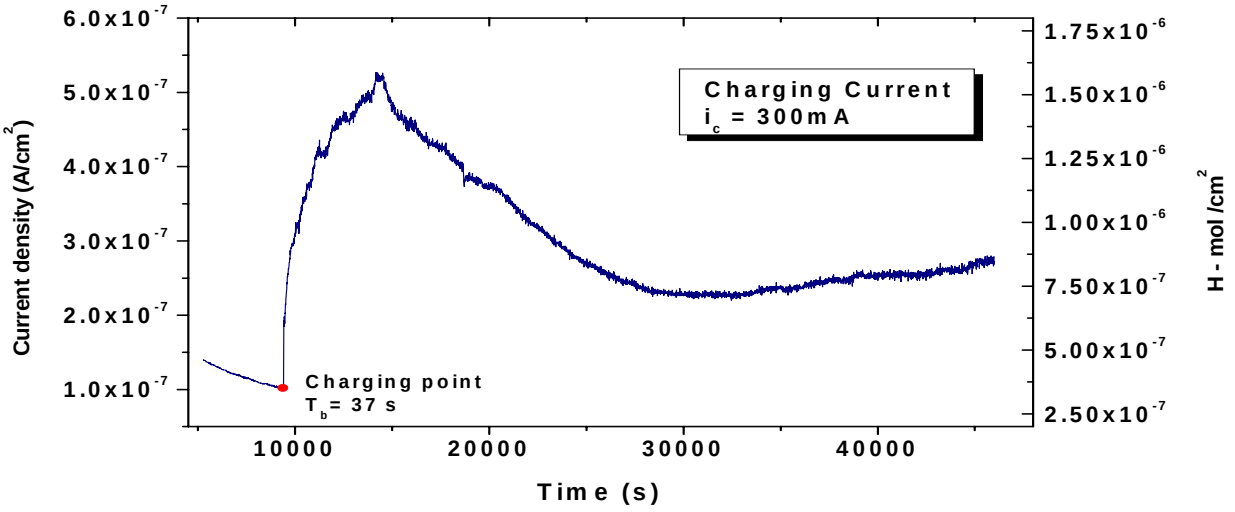

(a)

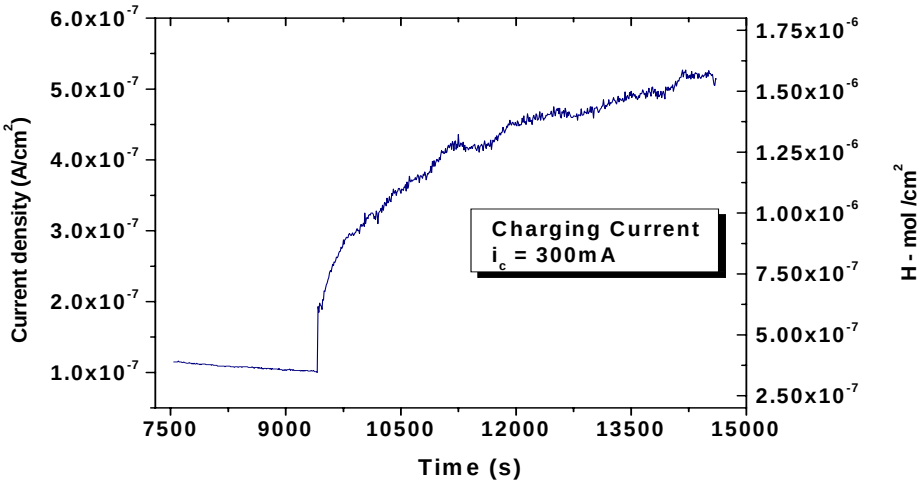

(b)

Figure 4.16 Hydrogen permeation profile for a 300mA current charging of a polished sample. (a) Complete hydrogen permeation profile, (b) Detailed portion of transient and steady state profile

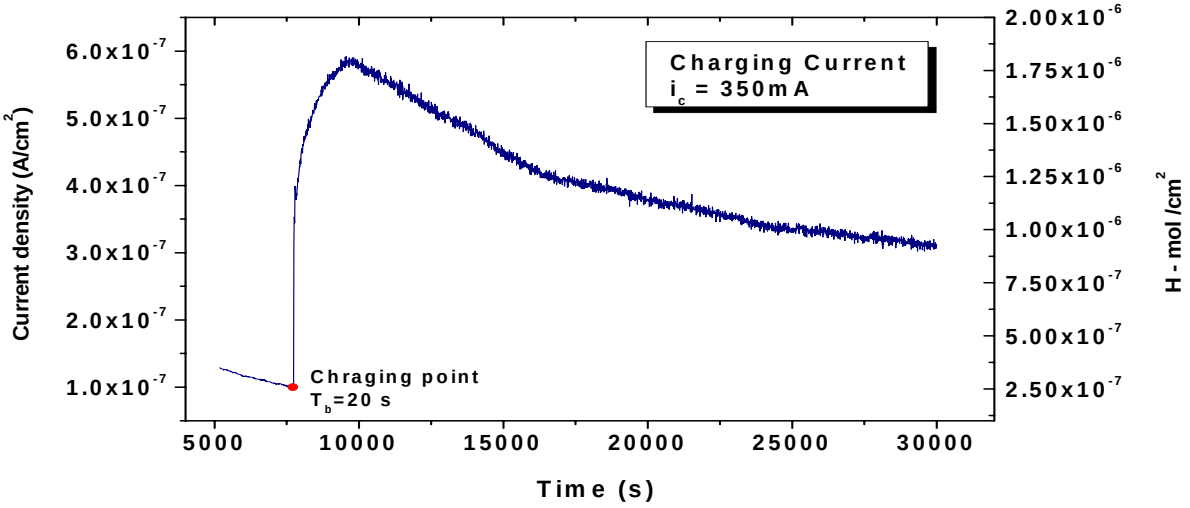

(a)

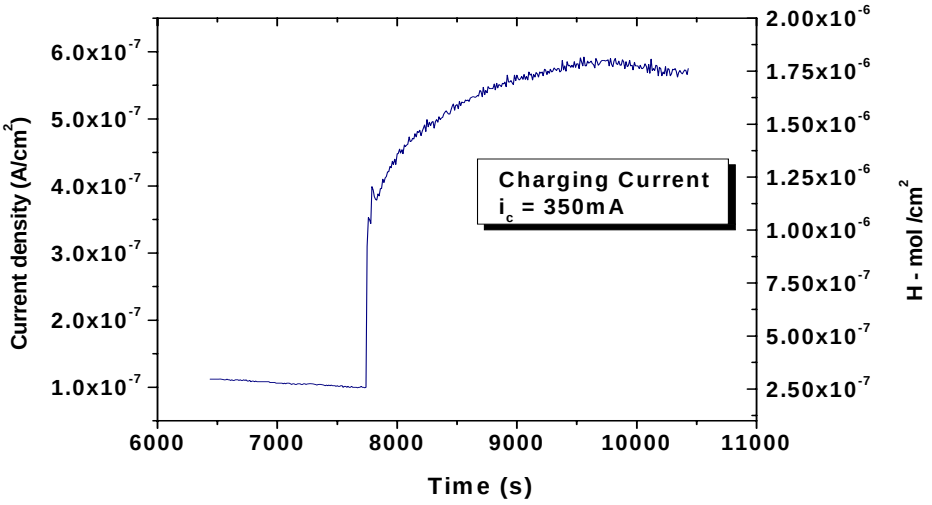

(b)

Figure 4.17 Hydrogen permeation profile for a 350mA current charging of a polished sample. (a) Complete hydrogen permeation profile, (b) Detailed portion of transient and steady state profile

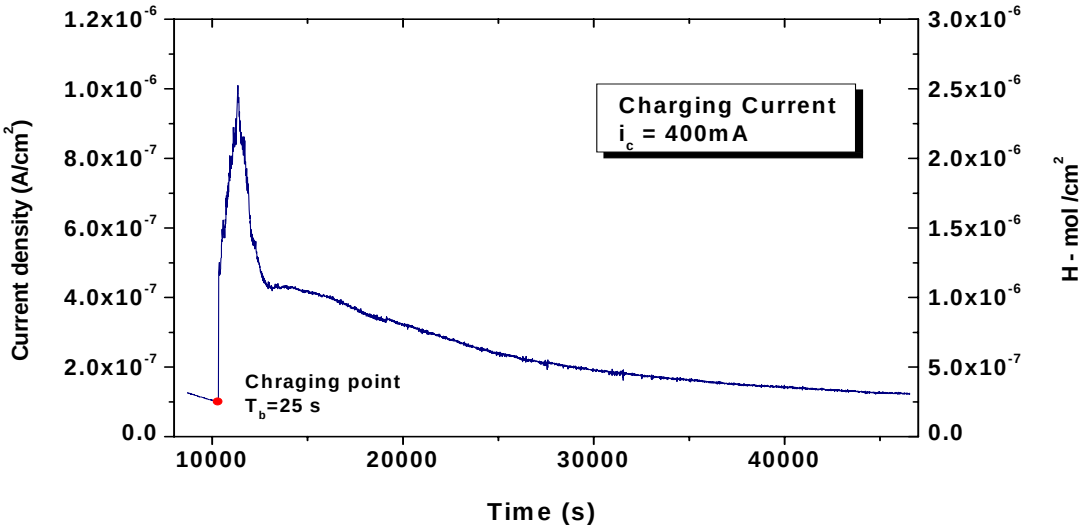

(a)

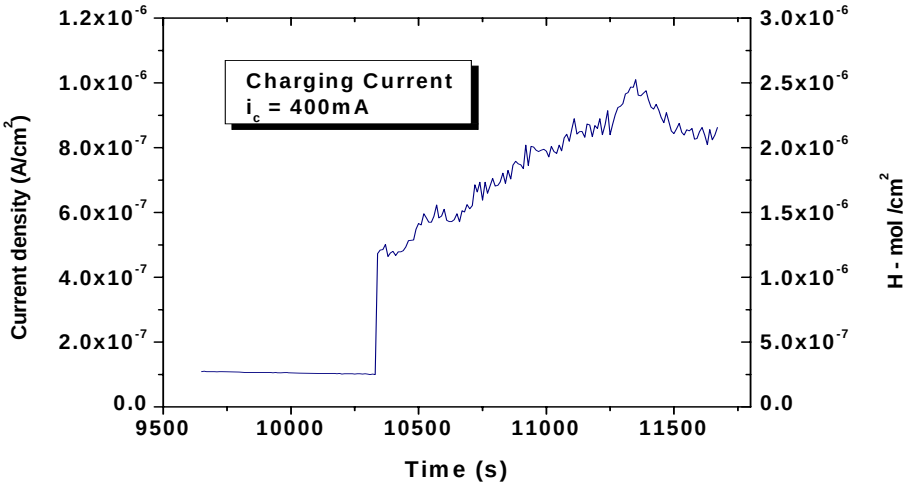

(b)

Figure 4.18 Hydrogen permeation profile for a 400mA current charging of a polished sample. (a) Complete hydrogen permeation profile, (b) Detailed portion of transient and steady state profile

The breakthrough time (t_b) recorded for the 100mA was 35 seconds while the time recorded for the 150mA was 40 seconds. The increase of the current density to 200mA showed a t_b time of 45 seconds. Even though first observations showed that the increasing breakthrough time was proportional to the charging current employed in every experiment, further experiments demonstrated that this relationship was not correlated. That is the case for example of experiments done with charging current densities varying from 250mA to 400mA (Figures 4.15 to 4.18). Table 4.8 shows the different currents employed along with their respective breakthrough times. As shown in Table 4.8, t_b times vary regardless of the charging current.

TABLE 4.8 Summary of breakthrough times with different current charging for polished samples

Current charging (mA)	100†	150†	200†	250†	300†	350†	400†
Break Through time (t_b) (s)	35	40	45	30	37	20	25

†Charging Time = 24hours

Increasing the cathodic charging current led to an increase of temperature in the electrolyte on the entry side. This event similarly occurred for permeation experiments on the as-received samples. Figure 4.19 showed the recorded raise in electrolyte (0.1M H_2SO_4 with 1g/l of Na_2HAsO_4-$7H_2O$) temperature vs. cathodic current charging. Measured pH for both the acid and base electrolyte were 3 and 13 correspondingly.

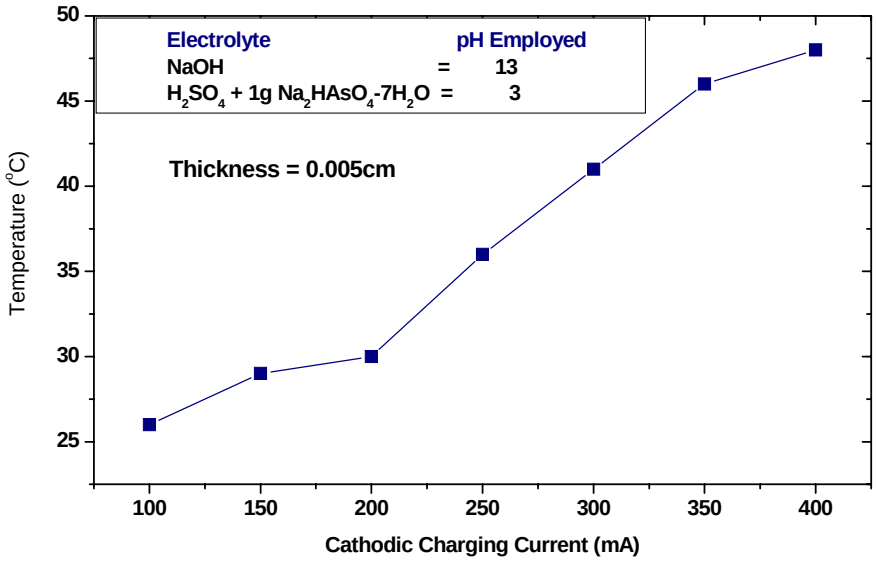

Figure 4.19 Electrolyte temperature with variation of cathodic charging current

4.2.2 Electrochemical Determination of Hydrogen Diffusivity and Concentration

Electrochemical calculations were done as indicated in section 4.1.2. Permeation transients and diffusivity were recorded after measuring the instantaneous rate of hydrogen permeation through the membrane. The amount of hydrogen leaving the metallic membrane at the exit side ($q_{H,L}$) and entry side($q_{H,0}$), were calculated accordingly using Equations 4.1 and 4.2, while the total amount of hydrogen retained or stored in the material ($q_{H,total}$) was determined by means of Equation 4.3. To find the value of the subsurface concentration (Co), Equation

4.4 was employed with a diffusivity obtained by the slope method. The calculated values are shown in Table 4.9 and Table 4.10.

TABLE 4.9 Summary of diffusion coefficient by slope and breakthrough time method for polished samples

Cathodic Charging Current (i_c, mA/cm^2)	*Slope Method* Apparent diffusion (D, cm^2/s) x10^{-11}	(t_b,s)	*Breakthrough Time Method* Apparent diffusion (D, cm^2/s) x10^{-8}
100	2.96	35	4.67
150	3.14	40	4.08
200	3.27	45	3.63
250	3.44	30	5.45
300	4.09	37	4.42
350	4.23	20	8.17
400	5.04	25	6.54

TABLE 4.10 Diffusible hydrogen and subsurface concentration at different charging current on polished samples

Cathodic Charging Current (i_c, mA)	Subsurface Concentration, (Co) *[H]-mol/ cm^3* (D, slope method)	*Diffusible Hydrogen [H]/ mol cm^{-2}*		$q_{H,\ total}$ = (Entry Side + Exit Side) *[H]- mol cm^{-2}*
		Entry Side (X=0)	*Exit Side (X=L)*	
100	2.66 x 10^{-4}	4.55 x 10^{-7}	2.27 x 10^{-7}	6.82 x 10^{-7}
150	2.72 x 10^{-4}	4.54 x 10^{-7}	2.27 x 10^{-7}	6.81 x 10^{-7}
200	3.07 x 10^{-4}	5.20 x 10^{-7}	2.60 x 10^{-7}	7.79 x 10^{-7}
250	4.97 x 10^{-4}	8.29 x 10^{-7}	4.15 x 10^{-7}	1.24 x 10^{-6}
300	6.60 x 10^{-4}	1.11 x 10^{-6}	5.56 x 10^{-7}	1.67 x 10^{-6}
350	7.15 x 10^{-4}	1.20 x 10^{-6}	6.02 x 10^{-7}	1.81 x 10^{-6}
400	1.04 x 10^{-3}	1.73 x 10^{-6}	8.65 x 10^{-7}	2.59 x 10^{-6}

As seen in section 4.1.2 the profile of subsurface concentration and hydrogen amount in the as-received (non-polished) sample behaved in an exponential manner. Similar profile is shown for permeated polished samples. Figures 4.20a and 4.20b depict this behavior. Different behavior was found for the diffusivity when the sample was subjected to polishing which according to Figure 4.21 shows an increase in the diffusivity. This could be attributed directly to the peeling-off of the protective layer on the surface. Even though the calculated diffusivities increased with respect to the as-received samples, the values were still very low. The polishing effect on the AISI-321SS steel did not affect the hydrogen concentration on the subsurface; this meant that hydrogen affected only the subsurface and not the material bulk.

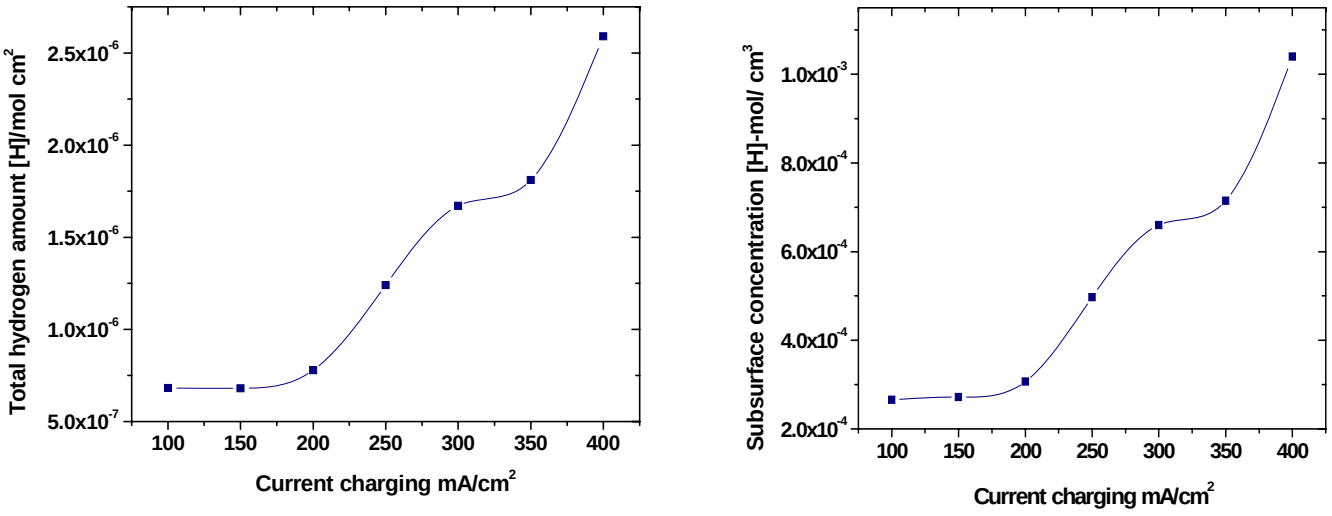

(a) **(b)**

Figure 4.20 Tendency at different current densities on the polished sample of (a) Total of hydrogen amount. (b) Subsurface concentration.

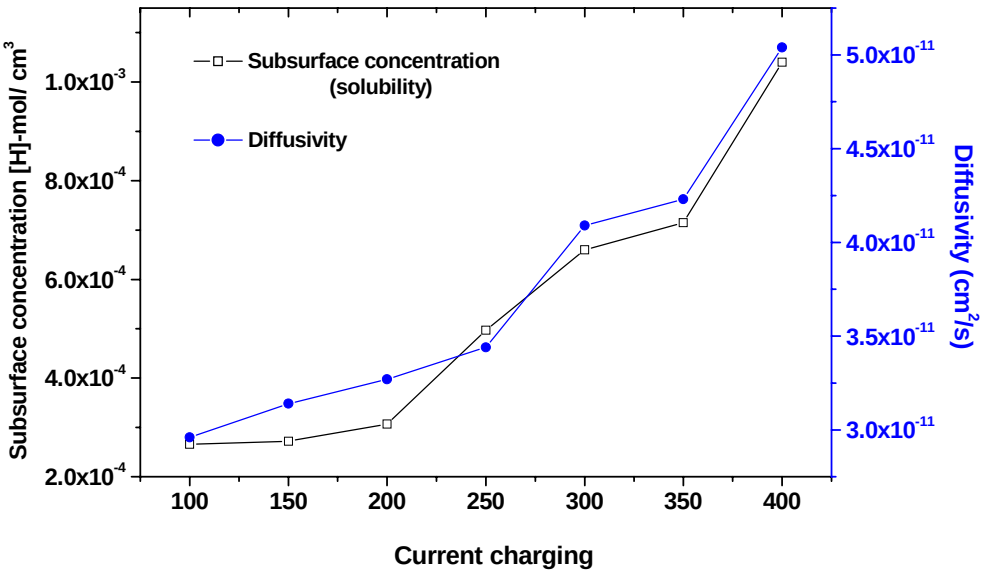

Figure 4.21 Comparison of diffusivity and subsurface concentration as a function of current charging for the polished sample

In contrast with experiments done with acid solution media, Zakroczymski [37] focused the hydrogenation of a high strength (0.99%C) steel sample plated with a thin palladium film, subjected to polarization in a saturated $Ca(OH)_2$ alkaline solution with cathodic current density of 1mA/cm^2 for 46 hours at 298K. After the completion of the charging process, the sample was immersed in solution of 0.1M NaOH to record the diffusion controlled desorption under anodic polarization conditions. This procedure estimated indirectly the diffusivity base on the egress of hydrogen. The diffusivity value was evaluated to be D= 1.66x10^{-7}cm^2/s. As a comparison with the latter experiment, the author [37] induced the hydrogen absorption on a foil sample of austenitic chromium-nickel (17% Cr, 12%Ni, 0.5%Ti) steel during 550 hours under cathodic polarization with a current density of

1mA/cm^2 in a solution of 0.1M H_2SO_4 along with the addition of a As_2O_3 promoter. The desorption process of hydrogen in the steel showed a diffusivity of D= 3.39x10^{-12}cm^2/s.

Studies of charging condition done by Farrell et al [11] on the 310 type steel immersed in 99% deuterated solution with arsenic as a promoter agent and a current density of 100mA/cm^2 applied for 24 hours, obtained a diffusivity value of D= 1.4x10^{-12}cm^2/s.

The diffusivity values found in this investigation under the same current density of 100mA/cm^2 for the as-received sample (D=9.22x10^{-11}cm^2/s), the polished sample (D=2.96x10^{-11}cm^2/s), and the heat treated sample (D=1.26x10^{-11}cm^2/s) are in close agreement with the previous investigation when cathodically charged in an acid electrolyte. However, the value of the diffusivity increases when the electrolyte media used for charging was alkaline even at low current density (1mA/cm^2).

The case of a high carbon content material such as AF1410 or Armco-Fe draws a different story about diffusivity values compared with austenitic steels. As reported by Charca-Mamani [42], the diffusivity found for Armco-Fe at low current density (1mA/cm^2) was D=2.37x10^{-5} cm^2/s in average, and for the AF1410, the average diffusivity was D=3.46x10^{-8} cm^2/s.

4.3 Model Verification of Experimental Data

4.3.1 Verification on AF1410 Probes

As was shown in chapter two, fitting the measured experimental build-up transients and steady state permeation can be done by combining the results of the first and second Fick's laws with a previous setting of pertinent boundary conditions. The potentiostatic model (exit side) applied in Figures 4.22 and 4.23 exhibited a good fit superposition for electrolytically charged AF1410 for a thickness of 1mm at 50mA and 100mA respectively by employing Equation 2.10. The diffusion coefficient obtained ($1.17x10^{-8}$ cm^2/s) for 50mA current charging and ($1.67x10^{-9}$ cm^2/s) for 100mA, agrees with the range found by Charca-Mamani [42] for the AF1410 type steel ($5.05x10^{-8}$ cm^2/s to $1.53x10^{-8}$ cm^2/s) under potentiostatic condition at different thickness with lower current charging (1mA-3mA).

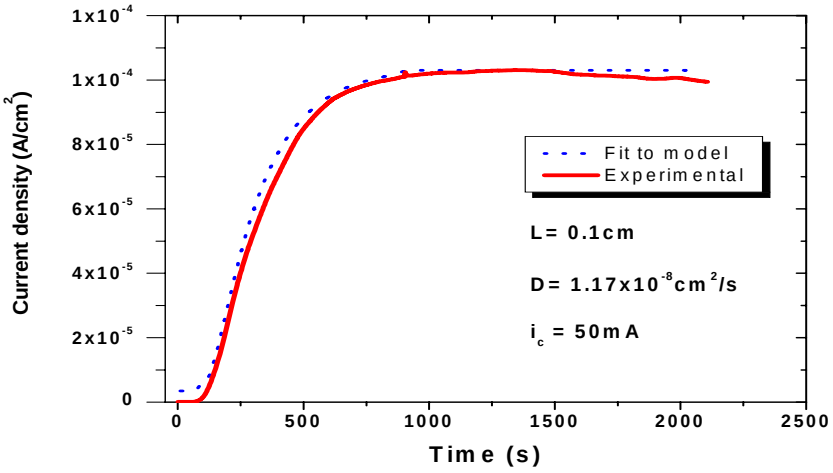

Figure 4.22 Comparison of the experimental hydrogen permeation Vs the mathematical model for AF1410 with thickness of 1mm with charging current of 50mA

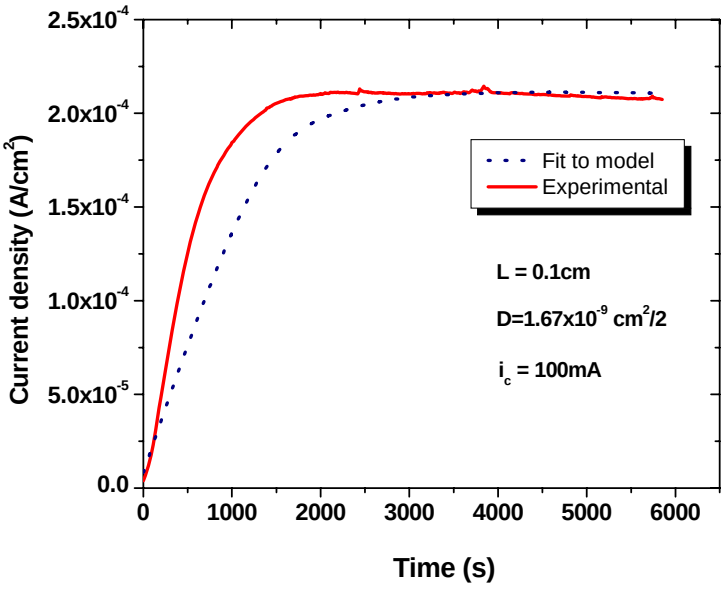

Figure 4.23 Comparison of the experimental hydrogen permeation Vs the mathematical model for AF1410 with thickness of 1mm with charging current charging of 100mA

4.3.2 Model Verification of Permeation on AISI-321 Stainless Steel

The behavior of hydrogen uptake, transient and steady state permeation of the experimental data were presented and compared with the proposed model. The membrane thickness L=0.005cm and exposed charging area of 1.89cm^2 were employed in the calculation for every model fitting. Figures 4.24 to 4.27 show respectively the experimental permeation profile of 100mA, 250mA, 300mA and 400mA cathodically charged samples compared with the obtained model under potentiostatic conditions.

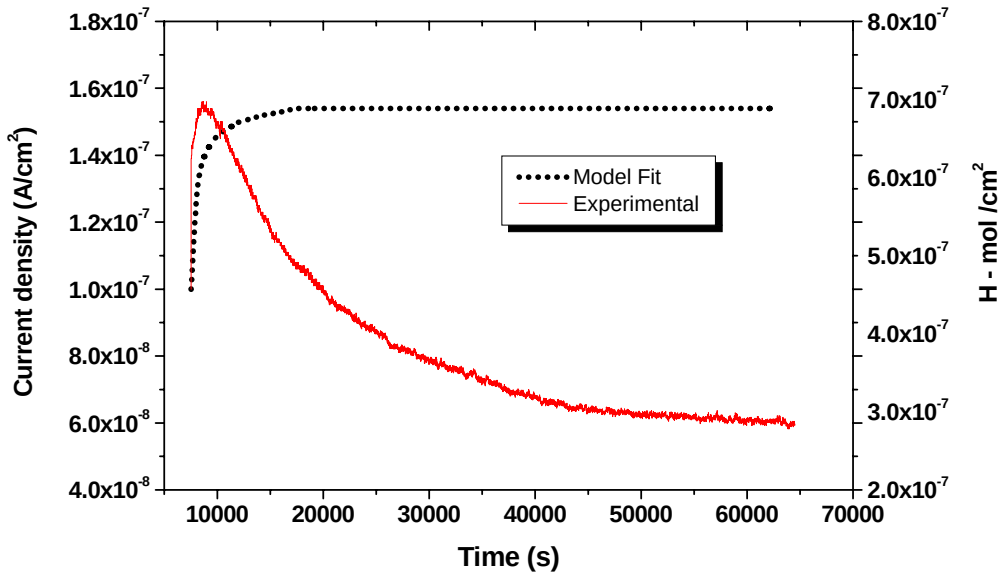

Figure 4.24 Hydrogen permeation profile and model verification for current charging of 100mA for the polished AISI-321SS

Previous experiments done using charging currents less than of 100mA did not show that permeation occurred over a period of 12 days. As a result, 100mA was used as a starting point for charging the samples. Experimental data showed that a previous stabilization current density (<< 1μA/cm^2) before starting the electrolytic charging was reached around the 10000 seconds and the peak permeation was attained after 4000 to 5000 seconds.

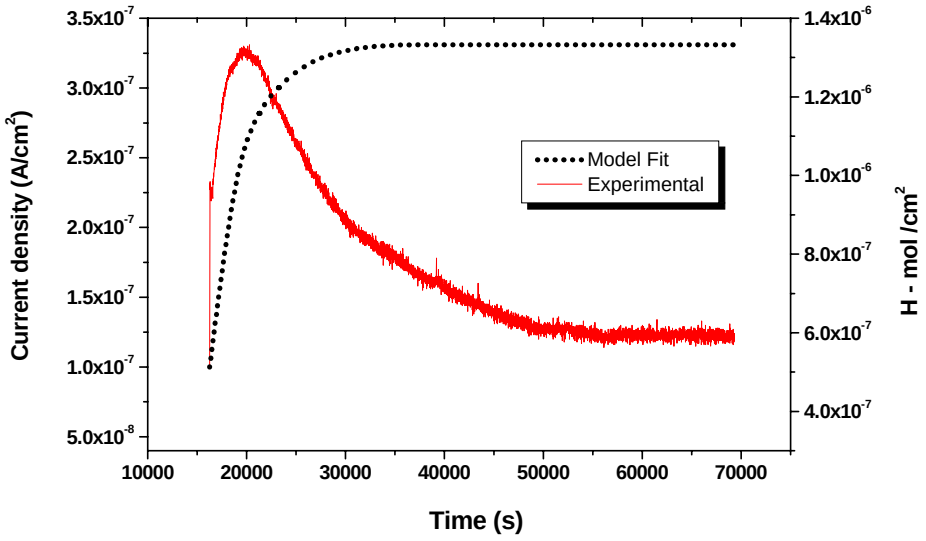

Figure 4.25 Hydrogen permeation profile and model verification for current charging of 250mA for the AISI-321SS

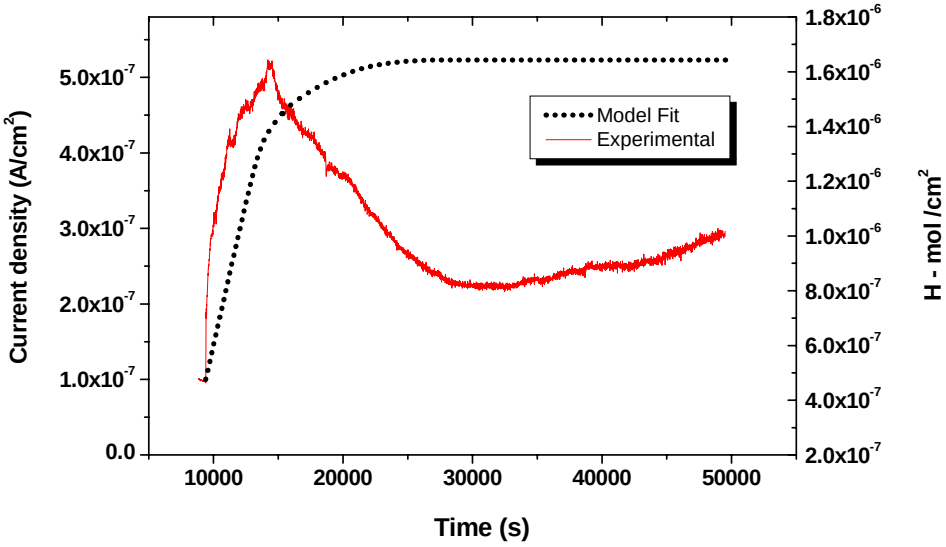

Figure 4.26 Hydrogen permeation profile and model verification for current charging of 300mA for the AISI-321SS

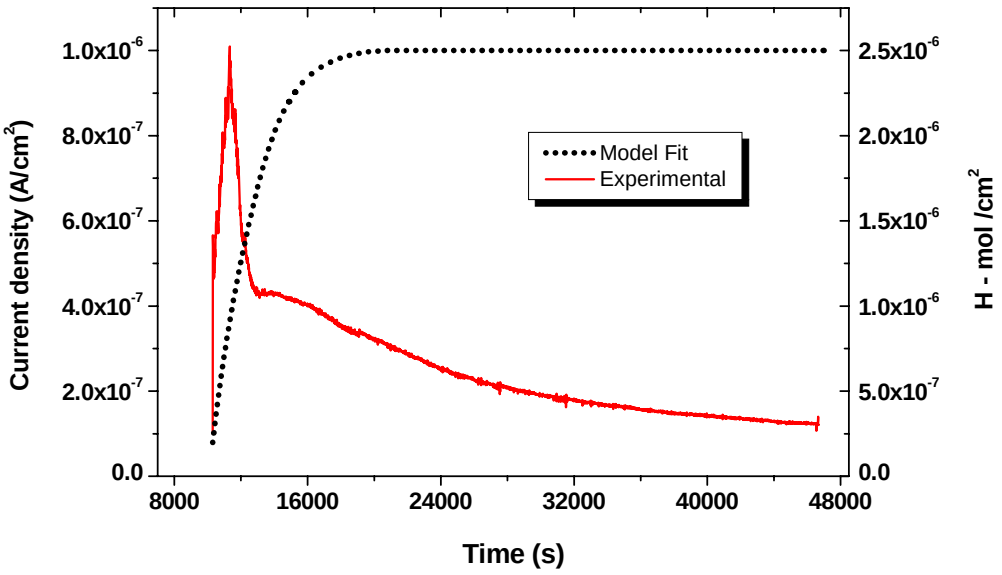

Figure 4.27 Hydrogen permeation profile and model verification for current charging of 400mA for polished AISI-321SS

4.3.3 Model Verification of Hydrogen Discharge on AISI-321 Stainless Steel

Once the permeation experiments reached the steady state value for a given charging conditions, the cathodic current was switched off and the cathodic chamber (entry side) of the Devanathan cell was rinsed with ethanol along with the sample cathodic side to avoid further corrosion. The entry side was topped of with a solution of 0.1M NaOH and a positive potential was applied. The anodic currents recorded at the entry side of the membrane during desorption of hydrogen are shown in Figure 4.28 and 4.29. Equation 2.11 was employed for the mathematical fitting of hydrogen discharge at the entry side (X=0).

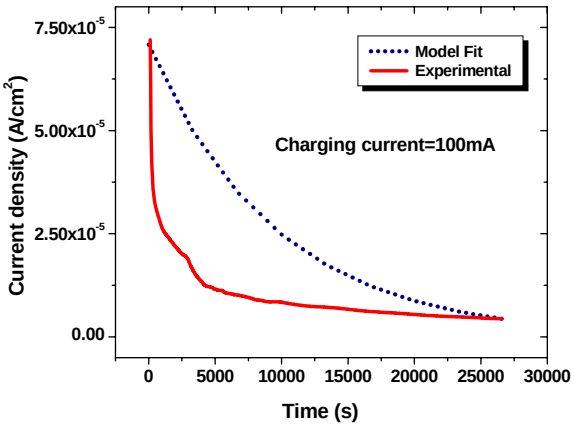

(a)

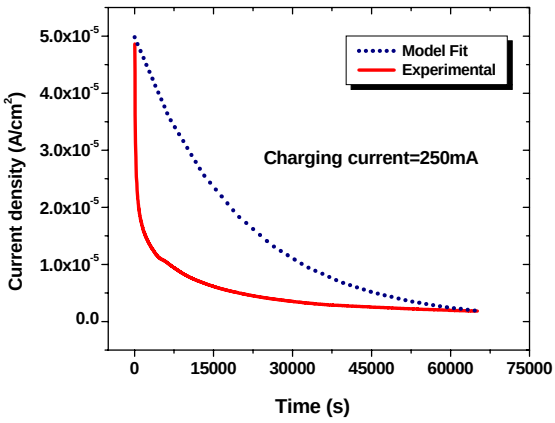

(b)

Figure 4.28 Hydrogen desorption profile and model verification for previous cathodic polarization of AISI-321SS at current charging of (a) 100mA, (b) 250mA

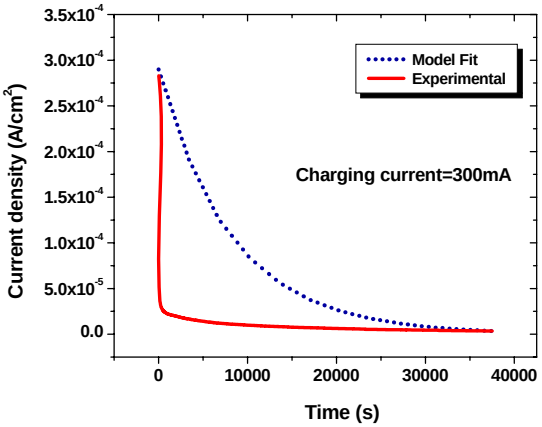

(c)

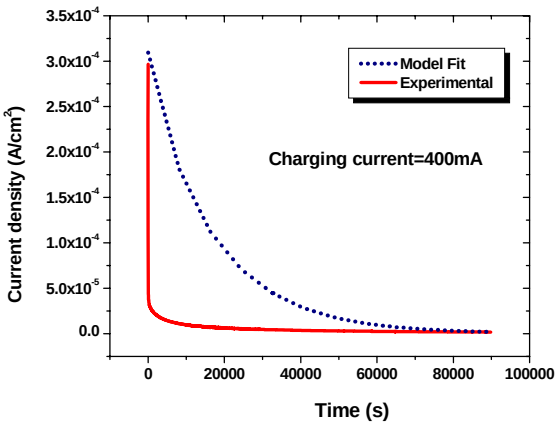

(d)

Figure 4.29 Hydrogen desorption profile and model verification for previous cathodic polarization of AISI-321 at current densities of (c) 300mA and (d) 400mA

4.4 Surface Analyses

Scanning electron microscope (SEM) technique was used to observe the surface morphologies of the 150mA cathodically charged samples, in a solution of 0.1M H_2SO_4 plus 1g/l of $Na_2HAsO_47H_2O$. The charging time of individual samples were 5 minutes, 10 minutes, 30 minutes, 60 minutes, and 24 hours, while the aging time was 15 days. Micrograph of the as received sample (not previously charged) can be seen in Figure 4.30.

Examination of the sample surface by SEM technique demonstrated that room temperature aging of pre-charged samples leads to hydrogen egress from the subsurface and consequent increase of cracking. As can be seen in Figure 4.31, a 5 minute charged sample followed by 15 days of aging developed microcracks, and voids on the surface. α-martensite phases can be identified morphologically as lath or needle shape and can also be observed in Figure 4.31. Figure 4.32 and 4.33 refer to an aged sample after cathodically charged for 24 hours. In these particular micrographs it was possible to observe a severely cracked surface. The presence of highly cracked regions suggests that the hydrogen charging leads to the formation of local strains.

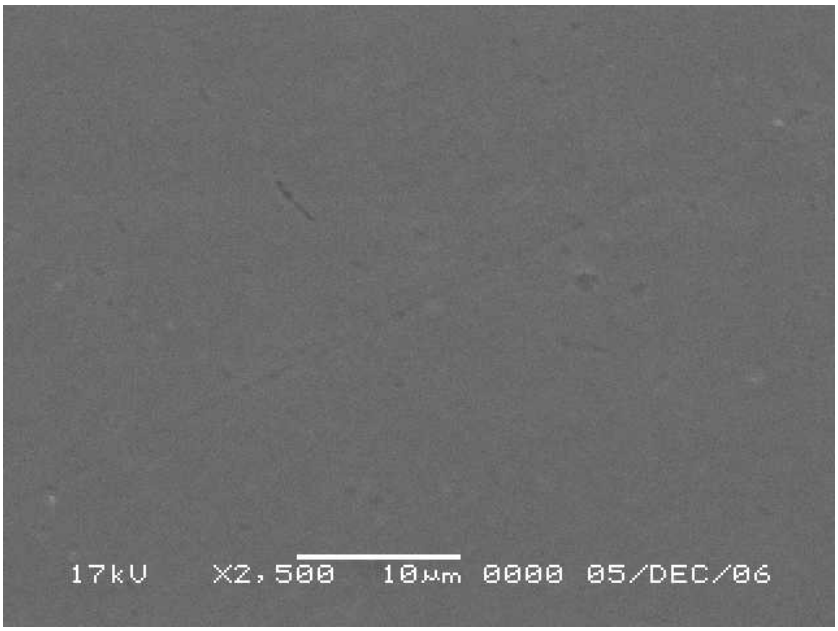

Figure 4.30 Micrograph of uncharged as-received sample

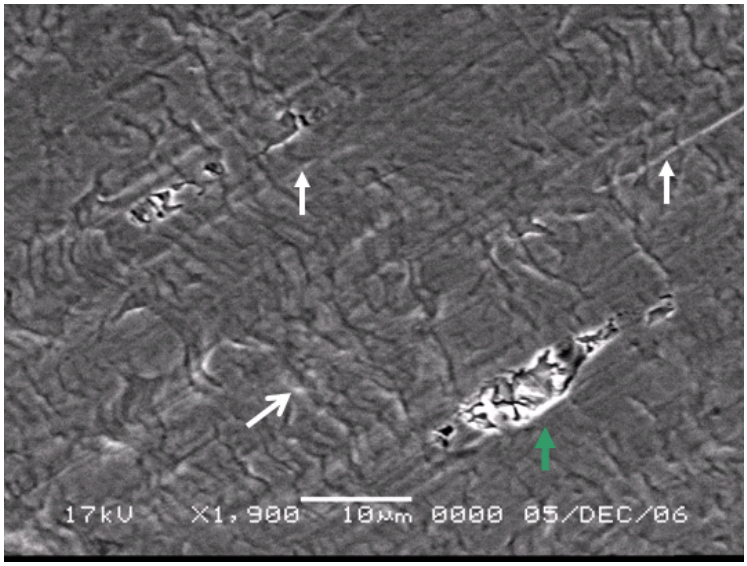

Figure 4.31 Surface morphology of as-received sample charged for 5 minutes under charging current of 150mA. Martensitic lathes (filled arrow heads), microcracks regions (unfilled arrow head)

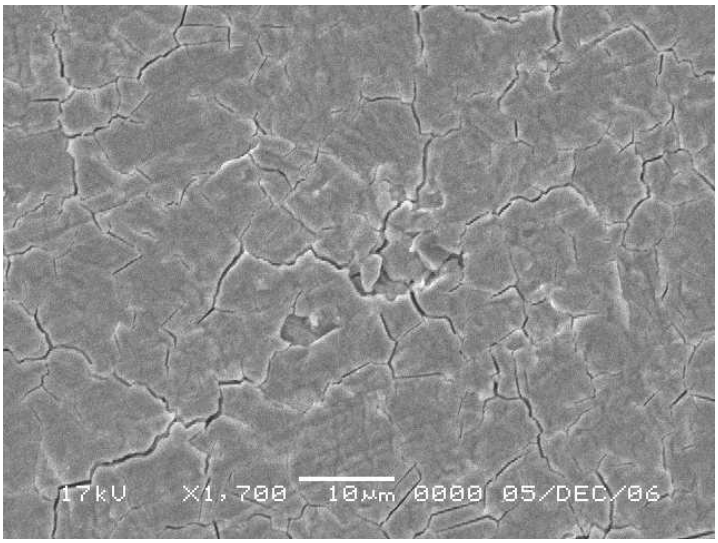

Figure 4.32 Surface morphology of as-received sample charged for 24 hours under current charging of 150mA.

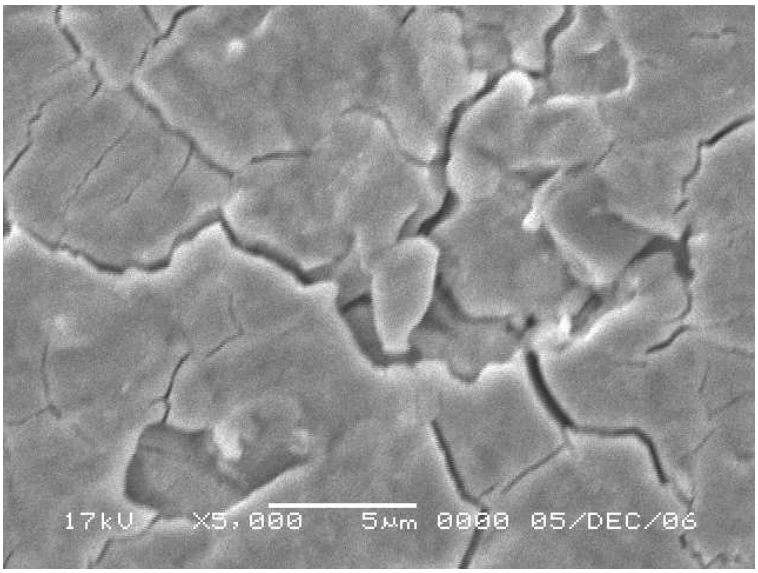

Figure 4.33 Enhanced micrograph of the as-received sample charged for 24 hours under current charging of 150mA

4.5 X-Ray Analysis

Hydrogen charging of AISI-321SS type stainless steel was studied by x-ray diffraction. X-ray spectrum on the as-received sample between 20 to 110 degrees of Bragg angle is shown in Figure 4.34. The profile exhibited four austenite peaks. Two low intensity peaks corresponding to reflection from the (111) and (200) indices and two sharp high intensity peaks indexed as (220) and (311) were observed respectively. Table 4.11 summarizes the indexing of the austenitic starting material with the resultant phase before hydrogen charging.

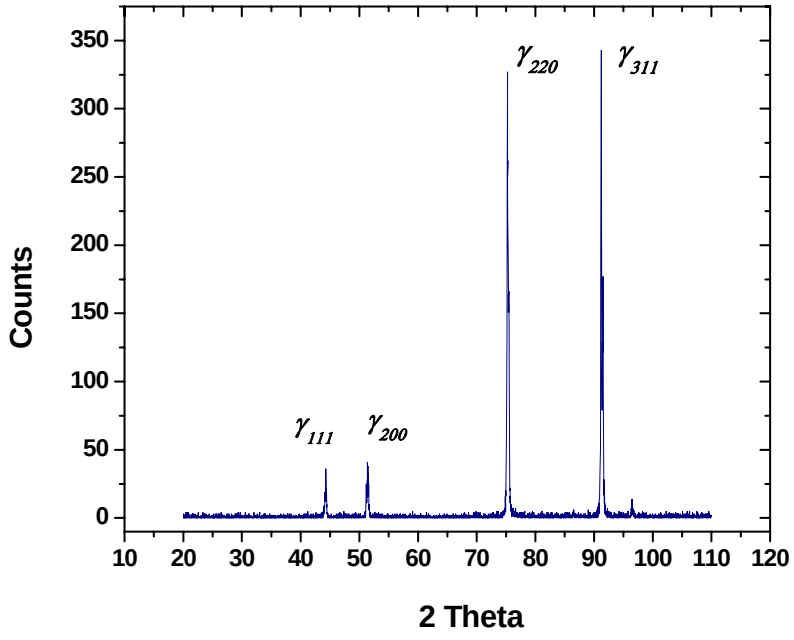

Figure 4.34 Diffraction pattern for the as-received AISI-321SS austenitic steel

TABLE 4.11 Peak positions and intensity in the as-received samples.

Angle (2θ)	44.3 *(111)*$_\gamma$	51.48 *(200)*$_\gamma$	75.26 *(220)*$_\gamma$	91.22 *(311)*$_\gamma$
Related intensity	36	41	327	343

4.5.1 Effect of Hydrogen Permeation on Phase Transformation

X-ray measurements were done immediately after hydrogen permeation on the samples to investigate phase transformation corresponding to different charging conditions. The x-ray spectrum (base) from the as-received sample is shown along with the permeated spectra peaks for comparison. Permeated samples were subjected to XRD measurements mainly on the entry side because hydrogen transport through the material is not uniform and affect the bulk by concentration gradient. As seen in Figure 4.38, evaluation of x-ray diffractions on permeated samples under current charging of 100mA, 200mA and 300mA on the anodic side (exit side) did not reflect any considerable transformation as opposed to the entry side. The diffraction pattern obtained for permeation experiments conducted during a period of 24 hours each, showed the apparition of new spectral peaks on the entry side of the sample which developed during hydrogen permeation at different current densities (Figure 4.39 and 4.40). Even though it was possible to observe transformation in the material, the evolution or change of each peak could not be directly established from the x-ray diffraction profile on permeated samples.

To investigate the phase evolution and decomposition for the AISI-321SS type, five different samples were cathodically charged at a current of 150mA for periods of 5 minutes, 10 minutes, 30 minutes, 1 hour and 24 hours. X-ray diffraction patterns obtained for this experiment can be seen in Figures 4.41 and 4.42. These figures represents the obtained diffractograms immediately taken after cathodic charging while Figure 4.43 and 4.44 represent the diffraction patterns of the previously charged samples after 15 days of room ambient aging. One of the effects of hydrogen charging on AISI-321SS is the macroscopic deformation leading to a warping of the material in question. The higher the current density employed, the higher the hydrogen evolution generated and consequently the higher the twist and deformation in the sample. This effect can be exemplified with representative samples after days of hydrogen charging as seen in Figure 4.35 (samples not permeated). The previous effect made difficult the direct comparison between diffractograms as samples had to be placed as plane as possible over the x-ray holder. The main disadvantage of this effect laid on the resulted diffraction pattern that could be shifted either to the left or right. To overcome this effect, lattice parameter and width calculations were obtained by computing the average lattice values of every single phase for each diffractogram.

Figure 4.35 Macroscopic deformation during hydrogen charging on the AISI-321SS steel [56]

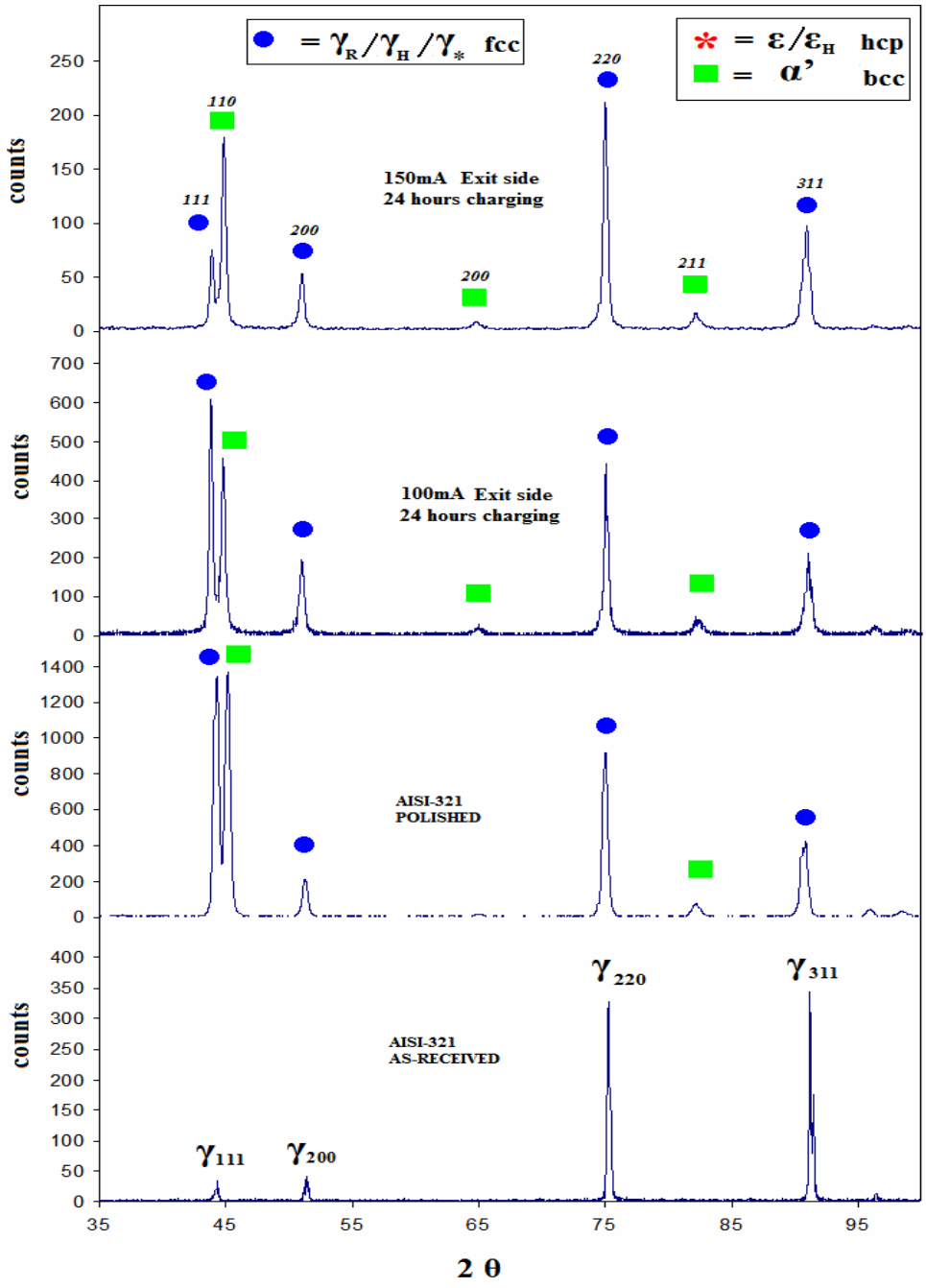

Figure 4.36 X-ray diffraction patterns from the anodic side (exit side) of as-received permeated samples under different current charging (100mA and 150mA). ε_H =Sub-surface; γ_R =Retained; γ_H =Sub-surface; γ_* =Exposed surface/faulted

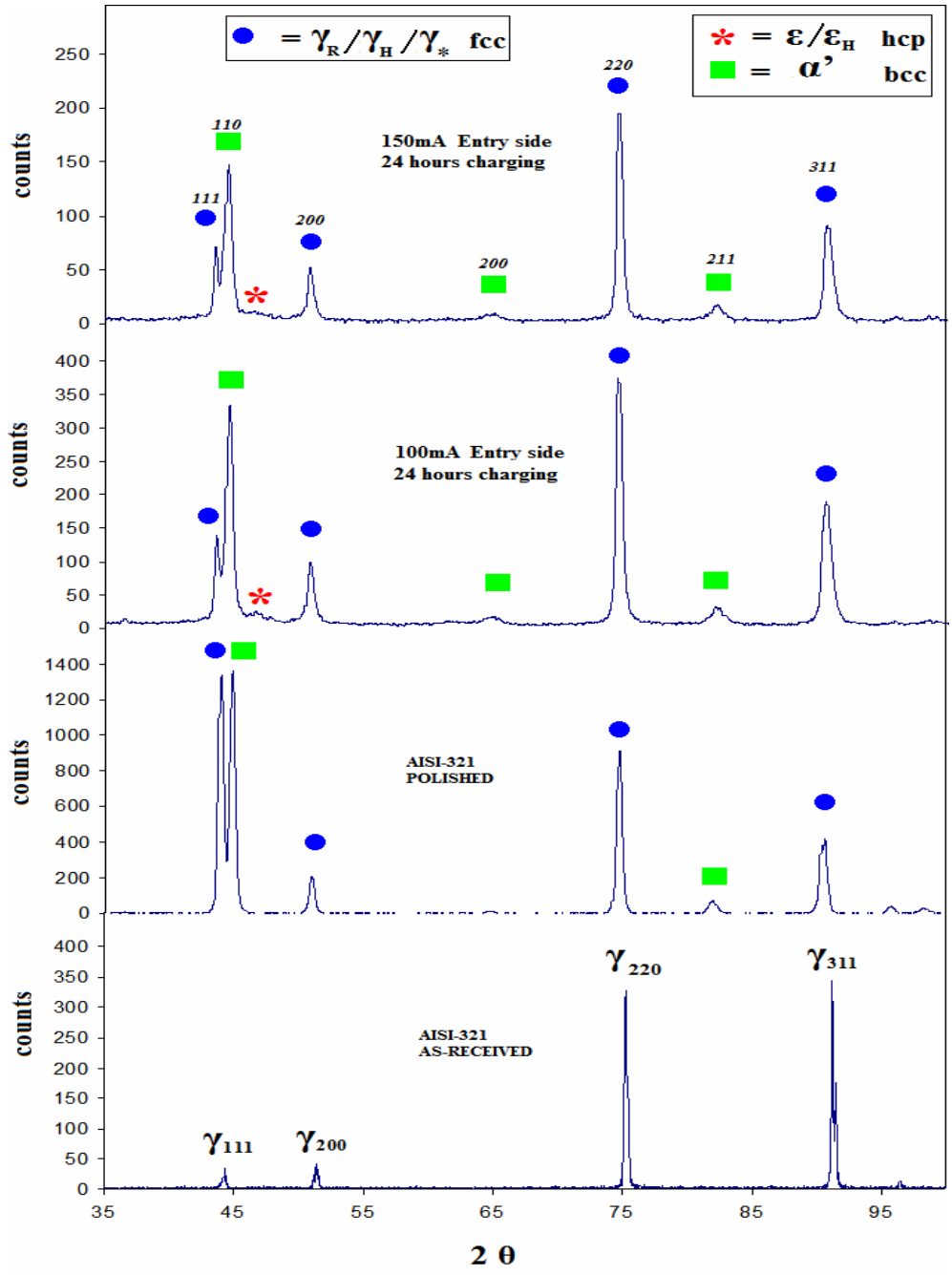

Figure 4.37 X-ray diffraction patterns from the cathodic side (entry side) of as-received permeated samples under different current charging (100mA and 150mA). *ε_H =Sub-surface; γ_R =Retained; γ_H =Sub-surface; γ_* =Exposed surface/faulted*

Figure 4.36 shows the x-ray diffraction pattern at the exit side of a permeated (100mA and 150mA) polished sample compared to the diffractogram of the as-received and both side polished material. Successive polishing of the material produced strain/stress on the surface that induced the formation of α' martensite. Similarly it can be seen that after cathodic charging there is an evolution of the martensite in the $\alpha'_{(200)}$ and $\alpha'_{(211)}$ diffraction lines. As in the case of the exit side, the x-ray diffraction pattern at entry side, the $\gamma_{(111)}$ peak exhibit a decrease in intensity due to charging of hydrogen and the initial formation of strain-induced $\alpha'_{(110)}$ martensite due to polishing , this induced martensite has a masking effect on the adjacent austenite peak. The major difference between the entry and the exit sides includes the presence of ε peaks that are absent on the exit side. This further indicates that the entry side with varying hydrogen concentration gradient produced the structural change which resulted to the formation of ε.

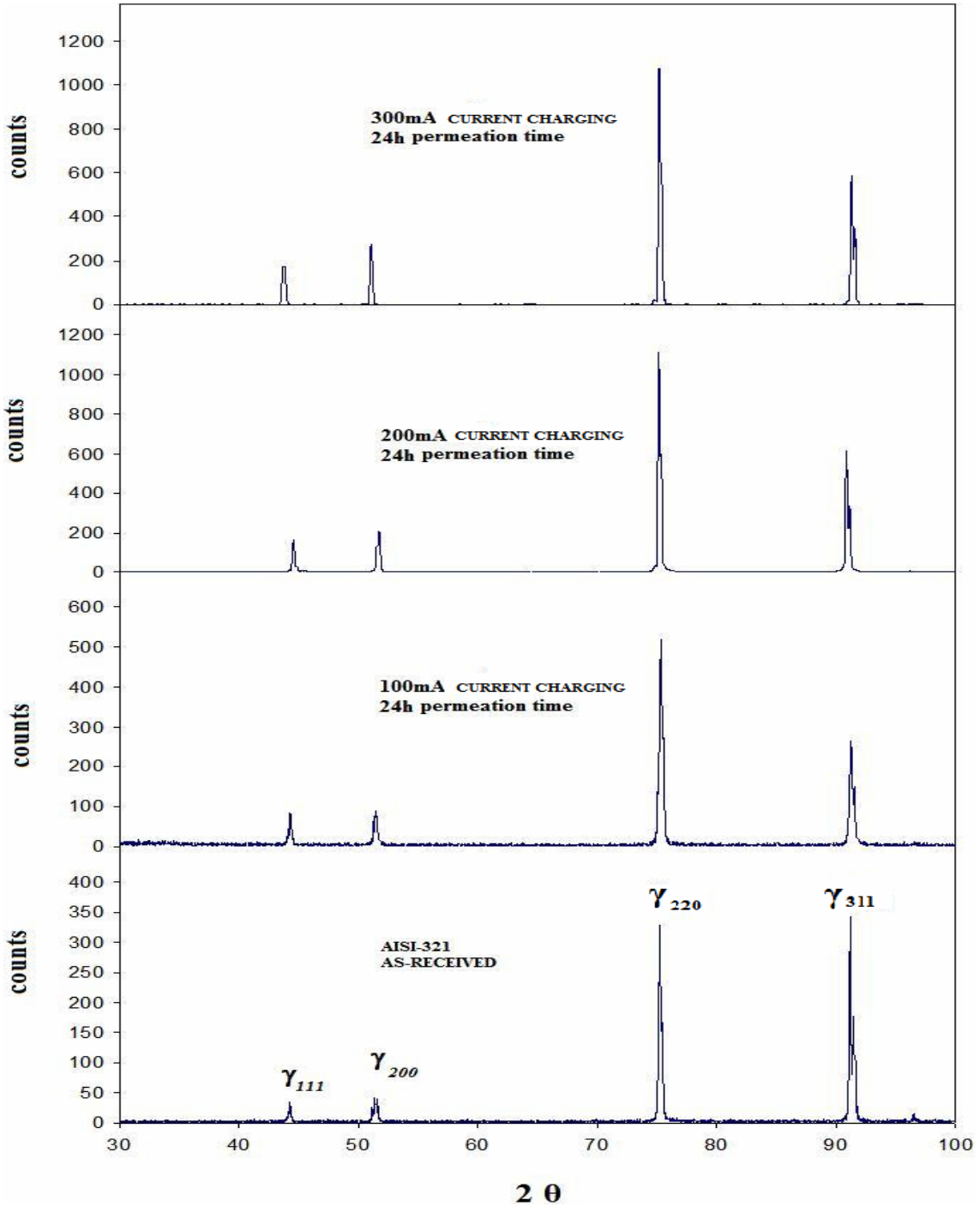

Figure 4.38 X-ray diffraction patterns from the anodic side (exit side) of as-received permeated samples under different charging current (100mA to 300mA).

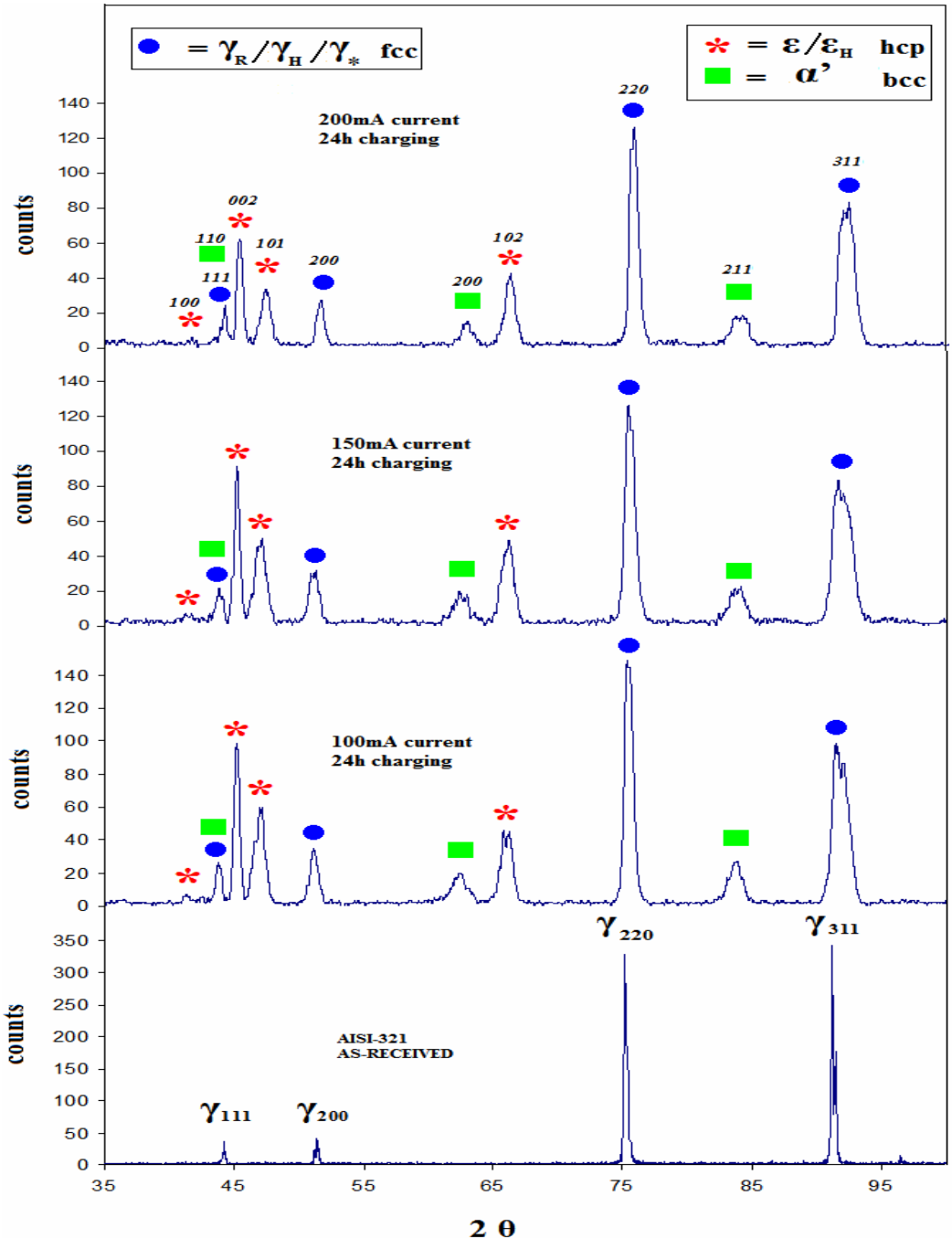

Figure 4.39 X-ray diffraction patterns from the cathodic side (entry side) of as-received permeated samples under different current charging (100mA to 200mA). ***E_H =Sub-surface; γ_R =Retained; γ_H =Sub-surface; γ_* =Exposed surface/faulted***

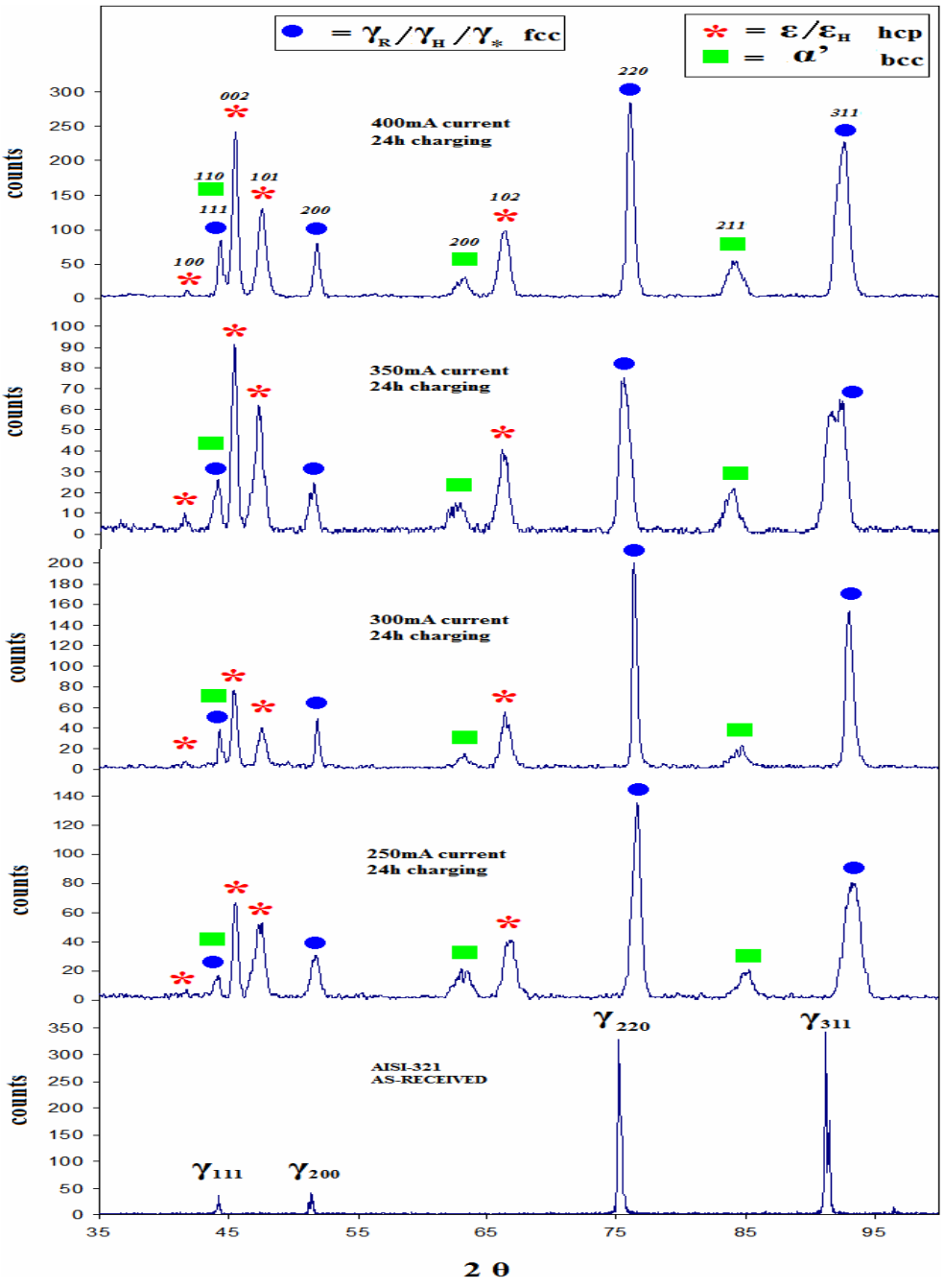

Figure 4.40 X-ray diffraction patterns from the cathodic side (entry side) of as-received permeated samples under different current densities (250mA to 400mA). ***E_H =Sub-surface; γ_R =Retained; γ_H =Sub-surface; γ_* =Exposed surface/faulted***

As seen in Figures 4.39 and 4.40, diffraction measurements done immediately after hydrogen permeation, showed the appearance of new peaks identified as α' and ε. These mentioned peaks were indexed by the extinction principle [36]. Observed peak broadening can be associated with strained lattice, development of micro-structural defects such as dislocations, stacking faults, and voids. Due to the non-uniform hydrogen concentration built-up and development of micro-stress/micro-strain within few angstroms (Å) below the cathodically polarized surface (subsurface) where hydrogen entrance is taking place, it was possible to explain the peaks shift, broadening and change in intensities. Appearance and evolution of ε peaks close to the γ phase tend to mask the latter phase at lower angles. Base on the diffraction pattern in Figure 4.38, it was possible to determine that phase decomposition occurred only in the subsurface of the material at the entry side and not in the bulk or exit side (sample's anodic side).

The calculated width at half maximum for each peak resulted after hydrogen permeation is shown in Table 4.12. In addition, Table 4.13 shows the lattice parameter for the resulted phases.

TABLE 4.12 Full width at half maximum (FWHM) values of as-received samples permeated at different current densities

FWHM values for non-polished charged samples										
Current	**ε *(100)***	**γ*(111)* + α*(110)***	**ε (*002)***	**ε *(101)***	**γ *(200)***	**α *(200)***	**ε *(102)***	**γ *(220)***	**α *(211)***	**γ *(311)***
Base		***0.20***	-	-	***0.16***	-	-	***0.18***	-	***0.20***
100mA	0.20	0.22	0.24	0.24	0.16	0.16	0.32	0.44	0.40	0.40
150mA	0.20	0.24	0.36	0.30	0.36	0.36	0.36	0.48	0.36	0.48
200mA	0.20	0.28	0.40	0.40	0.40	0.20	0.40	0.56	0.24	0.56
250mA	0.22	0.30	0.44	0.40	0.40	0.44	0.44	0.59	0.40	0.64
300mA	0.24	0.36	0.48	0.40	0.44	0.24	0.48	0.64	0.40	0.64
350mA	0.24	0.40	0.48	0.48	0.48	0.32	0.48	0.64	0.44	0.79
400mA	0.24	0.40	0.52	0.48	0.54	0.20	0.54	0.73	0.28	1.02

TABLE 4.13 Lattice parameter average for gamma, alpha and epsilon phases for permeated samples

Current Charging	**γ (Å)**			**α' (Å)**	**ε (Å)**		
					***a* (Å)**	***c* (Å)**	**c/a**
Base	**3.567**			-	-	-	-
	a ***Surface***	***a*** **Sub-surface**	***A*** **Retained**				
100mA	3.594	3.599	3.589	2.923	2.428	4.033	1.661
150mA	3.599	3.609	3.582	2.928	2.433	4.032	1.657
200mA	3.577	3.589	3.572	2.935	2.423	4.020	1.659
250mA	3.591	3.602	3.585	2.934	2.426	4.029	1.661
300mA	3.565	3.637	3.573	2.930	2.423	4.018	1.658
350mA	3.597	3.595	3.568	2.947	2.452	4.044	1.649
400mA	3.570	3.545	3.571	2.917	2.420	4.012	1.658

In order to study the phase evolution during hydrogen charging, samples were subjected to cathodic charging with a single charging current of 150mA through different times ranging from 5 minutes to 24 hours. Immediately after charging, samples were characterized by x-ray technique. Diffraction patterns obtained at various times can be seen in Figure 4.41 and Figure 4.42. The original peaks associated with the as-received material can be seen to have different profile with subsequent peak broadening and slight peak position changes. These observations are important since as stated much earlier the measurements were carried out on materials that developed buckling following cathodic charging. The masking effect over γ phase by the ε phase at low angles is evident when the charging time reaches the 24 hours. Also α' phases begin to form at higher angles after 10 minutes of charging. Calculated values of half width at half maximum and lattice parameter can be seen in Table 4.14 and 4.15.

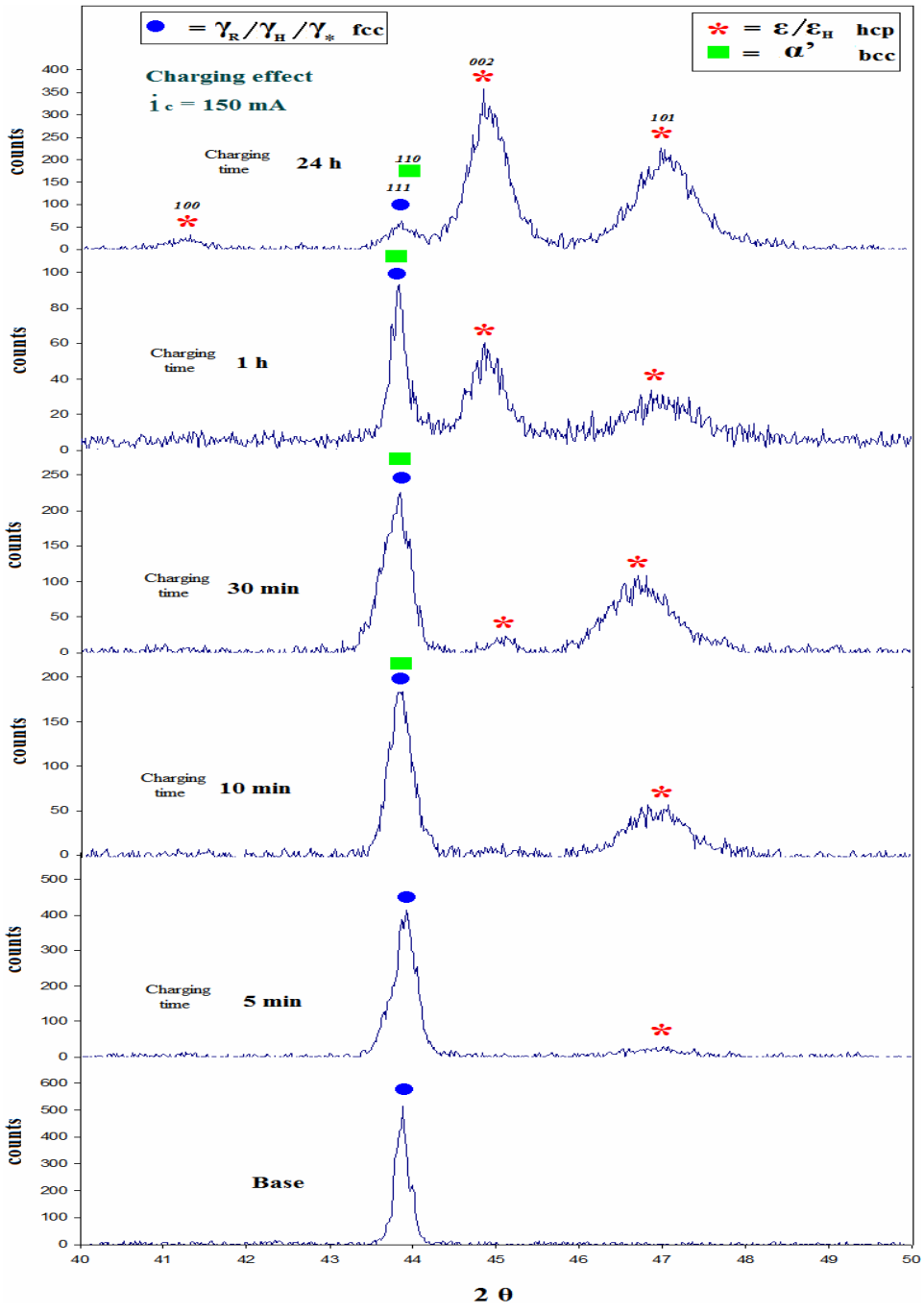

Figure 4.41 X-ray diffraction patterns (40 to 50 degrees angle) of as-received samples charged at 150mA/cm^2 for different times. *E_H =Sub-surface; γ_R =Retained; γ_H =Sub-surface; γ_* =Exposed surface/faulted*

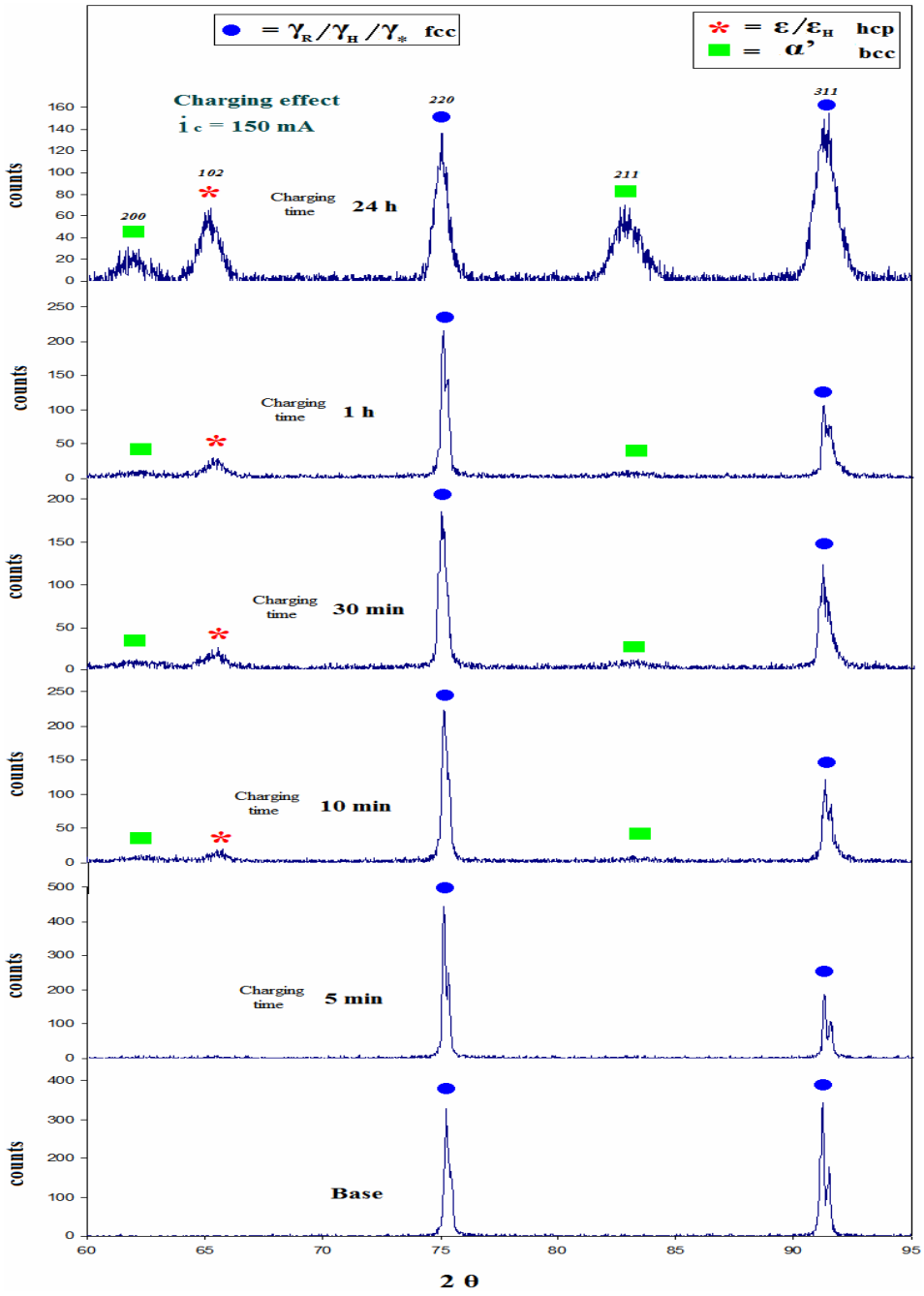

Figure 4.42 X-ray diffraction patterns (60 to 95 degrees angle) of as-received samples charged at 150mA for different times. E_H =Sub-surface; γ_R =Retained; γ_H =Sub-surface; γ_* =Exposed surface/faulted

TABLE 4.14 Full width at half maximum (FWHM) values of as-received samples previously charged at 150mA with corresponding charging time.

	FWHM values for non-polished charged samples								
Charging time	**ε (*100*)**	**γ*(111)* + α*(110)***	**ε (*002*)**	**ε *(101)***	**α *(200)***	**ε *(102)***	**γ *(220)***	**α *(211)***	**γ *(311)***
Base	**-**	**0.20**	**-**	**-**	**-**	**-**	**0.18**	**-**	**0.20**
5 min	-	0.22	-	-	-	-	0.24	-	0.22
10 min	-	0.28	-	0.20	0.16	0.20	0.32	0.12	0.32
30 min	-	0.32	0.20	0.20	0.12	0.20	0.36	0.16	0.36
1 hour	-	0.36	0.24	0.30	0.16	0.28	0.43	0.12	0.42
24 hours	0.16	0.38	0.32	0.32	0.14	0.40	0.49	0.28	0.98

TABLE 4.15 Lattice parameter average for gamma, alpha and epsilon phases for charged samples

Charging time	**γ (Å)**			**α' (Å)**	**ε (Å)**		
					***a*(Å)**	***c*(Å)**	**c/a**
Base	**3.567**			-	-	-	-
	a ***Surface***	***a*** **Sub-surface**	***a*** ***Retained***				
5min	3.582	3.588	3.560	-	-	-	-
10min	3.581	3.575	3.556	2.934	2.332	4.027	1.727
30min	3.584	3.594	3.560	2.911	2.336	4.024	1.723
1 hour	3.655	3.575	3.554	2.919	2.341	4.034	1.723
24 hours	3.582	3.560	3.556	2.927	2.406	4.044	1.225

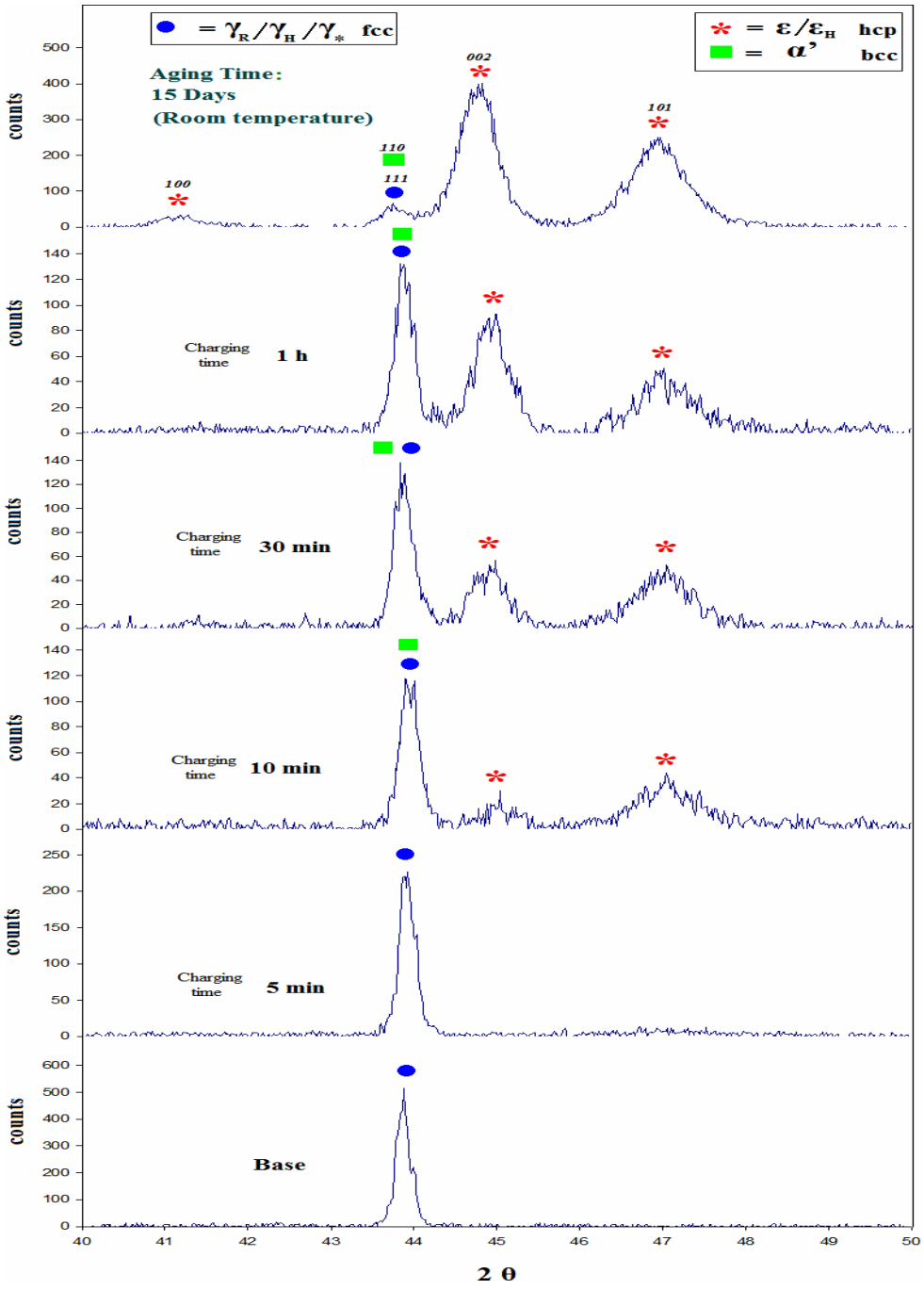

Figure 4.43 15 days aging time x-ray diffraction patterns (40 to 50 degrees angle) from previously charged as-received samples at 150mA current charging. E_H =Sub-surface; γ_R =Retained; γ_H =Sub-surface; γ_* =Exposed surface/faulted

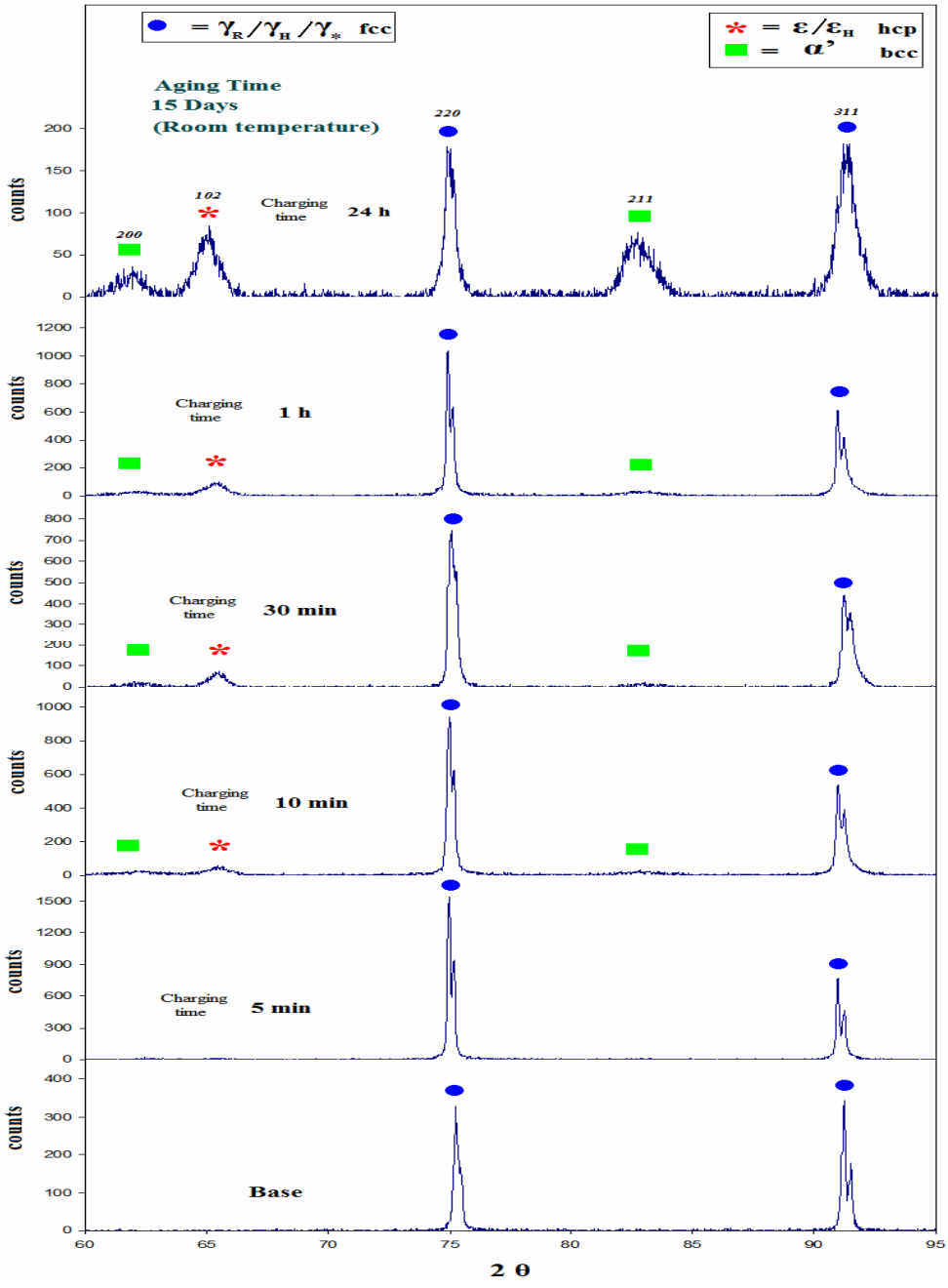

Figure 4.44 15 days aging time x-ray diffraction patterns (60 to 95 degrees angle) from previously charged as-received samples at 150mA/cm^2. ε_H =Sub-surface; γ_R =Retained; γ_H =Sub-surface; γ_* =Exposed surface/faulted

TABLE 4.16 Full width at half maximum (FWHM) values of as-received samples after 15 days of aging at room temperature with corresponding charging time.

	FWHM values for non-polished samples								
Charging time	**ε *(100)***	**γ *(111)* + α*(110)***	**ε (*002)***	**ε *(101)***	**α *(200)***	**ε *(102)***	**γ *(220)***	**α *(211)***	**γ *(311)***
Base	**-**	**0.20**	**-**	**-**	**-**	**-**	**0.18**	**-**	**0.20**
5 min	-	0.20	-	-	-	-	0.18	-	0.20
10 min	-	0.28	***0.16***	0.16	0.10	0.16	0.24	0.14	0.28
30 min	-	0.30	0.18	0.20	0.10	0.20	0.28	0.20	0.36
1 hour	-	0.34	0.20	0.27	0.16	0.24	0.37	0.16	0.41
24 hours	0.20	0.38	0.30	0.30	0.54	0.40	0.43	0.60	0.86

TABLE 4.17 Lattice parameter average for gamma, alpha and epsilon phases for aged samples

Charging time	**γ (Å)**			**α' (Å)**	**ε (Å)**		
					***a*(Å)**	***c*(Å)**	**c/a**
Base	**3.567**			-	-	-	-
	a ***Surface***	***a*** **Sub-surface**	***a*** ***Retained***				
5min	3.583	3.591	3.556	-	-	-	-
10min	3.582	3.585	3.554	2.929	2.332	4.032	1.729
30min	3.586	3.620	3.552	2.948	2.332	4.038	1.732
1 hour	3.586	3.591	3.555	2.936	2.342	4.035	1.723
24 hours	3.588	3.601	3.566	2.898	2.436	4.049	1.662

The previous results indicate that hydrogen intake affected the surface layer when the lattice parameter increased with charging time for the γ_* phase. Similarly, a slight increase of the lattice parameter for the γ_H phase in the sub-surface layer during different hydrogen charging times was observed as compared to the retained austenite γ phase. Calculated values of the lattice parameter during room temperature aging of the samples do not return to original γ values as seen in Table 4.16 and 4.17; this indicates that faulted regions remain and deformation in the material becomes permanent.

Similar findings were done by Hsiao et al. [57] who studied the deformation of AISI-321SS subjected to electrolytical charging. The author suggested that the asymmetry of $\gamma_{(200)}$ *and* $\gamma_{(111)}$ diffractions lines, was attributed to the appearance of hydride phases. The author found that hydrogen charging led to a constant increase of the lattice parameter in the austenite phase due to an augment of hydrogen content in the material. The local stress generated due to non-uniform hydrogen intake was compared to cold working. This stress would induce the martensitic transformation to ε. During aging of the samples, the lattice parameter of ε is decreased with time. Hsiao also indicated that the appearance of α' is accompanied by a loss of asymmetry of $\gamma_{(200)}$, implying the disappearance of metal hydride. The formation of metal hydrides caused the expansion of the lattice in the surface layer during hydrogen charging, meaning a compressive stress in the surface. In contrast, the decomposition of hydrides during aging caused the shrinkage of the surface and as a consequence, imposed a tensile stress which provoked the martensitic transformation and consequent surface cracking.

Schematics of hydrogen interaction in the AISI-321SS can be seen in Figure 4.45 as follows:

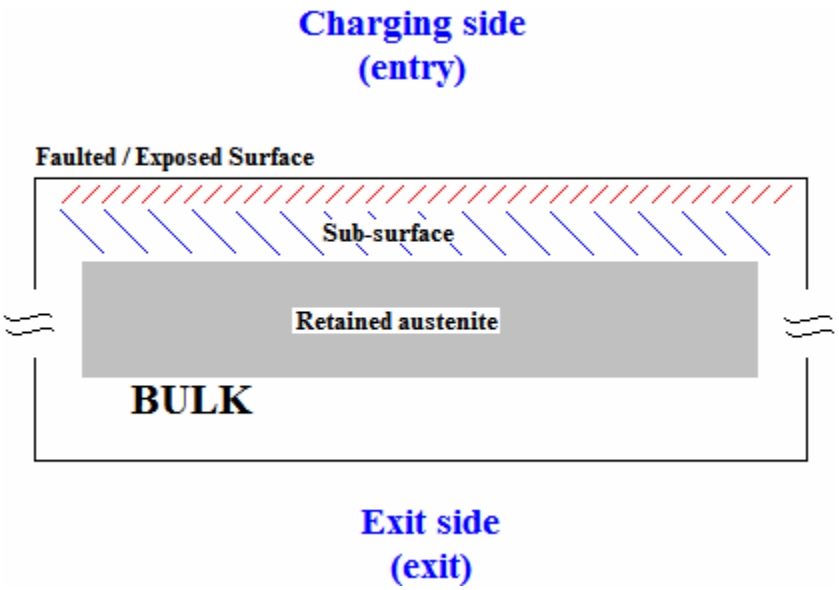

Figure 4.45 Schematics of hydrogen interaction in the AISI-321SS indicating the layer depth (not to scale) by hydrogen diffusion gradient

X-ray diffraction reports by Chen et al [1] focused on the phase decomposition of AISI-305 and AISI-304 type steel when samples were subjected to cathodic charging in aqueous media (H_2SO_4 + 0.25 g/l $NaASO_2$) at different current densities of 1, 10, and 100 mA/cm^2 for various times ranging from 5 minutes to 32 hours at room temperature. In the case of the 304 stainless steel (for comparison with the AISI-321SS type steel), two peaks were identified as hydrides by means of a profile fitting program using Lorenz function. These peaks were identified as γ^* with fcc structure and a lattice parameter a= 0.362nm, and the ε^* with hcp

crystal structure with lattice parameter a= 0.261nm and c= 0.425nm. The effect of charging on the 304 sample at different times, showed equally the same result for current densities of 10mA/cm^2 and 100mA/cm^2 as shown in Table 4.18.

TABLE 4.18 Phase decomposition of 304 steel type results at initial charging times of 5 and 30 minutes

Time	ε*	γ*
5 minutes	Present	----
30 minutes	Present	Present

The aging effect on the 304 sample indicated the disappearance of γ* and ε* hydrides, and the formation of α' and ε phases. The time of hydride decomposition was completed in 20 minutes.

Microstructural deformations produced by hydrogen concentration built-up on the surface material remain permanent after 15 days of aging with a possible slight structure restoration. In the development of the present work, no hydrides phases were identified. Formation of hydride phases on the 304 steel found by Chen [1] could have been developed due to fact that the material employed for the experiment (AISI-304SS steel) was a laboratory-heat (Fe18Cr9Ni). This type of preparation does not guarantee a perfect distribution of the alloying elements, leaving regions that could pick up hydrogen and become metallic hydride.

In the present study no hydrides have been confirmed by x-ray diffraction technique. As a private communication from Uwakweh et al. [56], mössbauer analyses on the cathodically charged AISI-321SS showed also no hydride formation on the material. A direct transformation of phases can be seen in Figure 4.46:

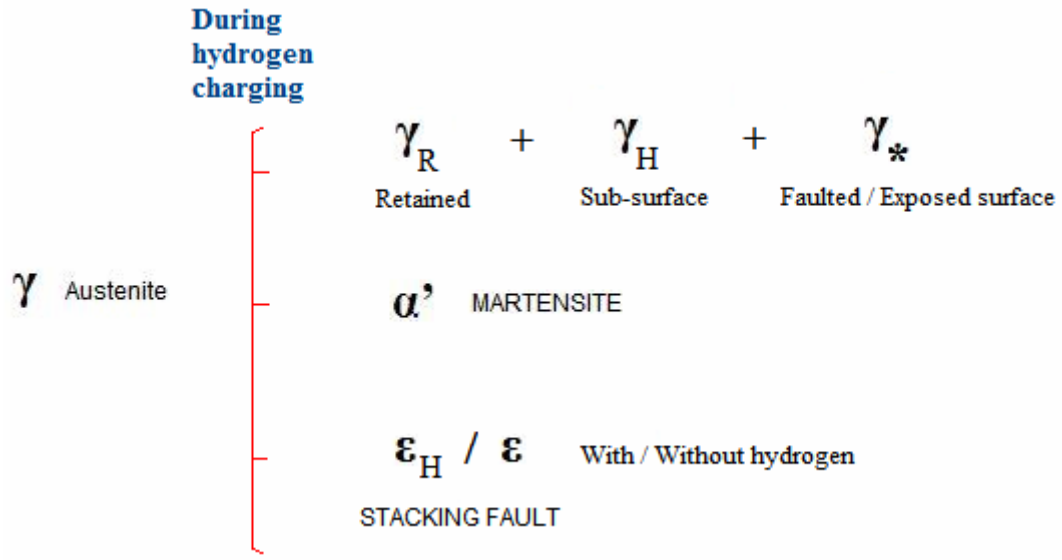

Figure 4.46 Schematics of phase decomposition of the AISI-321SS after cathodic polarization charging. The resulting phases remain and do not return to the austenitic state.

5 CONCLUSION

- The decomposition of the austenitic phase was identified in terms of three FCC, one α'- Martensitic BCC phase and two HCP. The FCC phases were identified as retained austenite, expanded and faulted austenitic phases. The hexagonal phases were identified as originating from structural faults.
- X-ray diffraction measurements exhibited peaks attributed initially to hexagonal ε – martensite phase.
- Buckling and warping of the AISI-321SS steel samples were attributed to inhomogeneous distribution of hydrogen in the subsurface layer under cathodic polarization that lead to structural deformation, based on SEM, x-ray diffraction measurements.
- The combination of SEM and x-ray techniques showed the appearance of α'-martensites phase in a previously hydrogen charged sample via cathodic polarization.
- Low values of the apparent diffusion coefficient for the AISI-321SS were calculated by Devanathan-Stachursky hydrogen permeation technique varying from $2.0x10^{-11}cm^2/s$ to $9.0x10^{-11}cm^2/s$.
- The minimum optimal current charging for AISI-321SS austenitic stainless steel was 100mA in a solution of 0.1M H_2SO_4 + 1g/l Na_2HAsO_4-$7H_2O$. This was based on analyses on permeation experiments.

- The sub-surface concentration for the as-received samples increased as the current charging increased while the values of the apparent diffusivity decreased. The different behavior observed for the polished material was attributed to the presence of α'-martensite generated during polishing.
- The predicted model for hydrogen permeation and diffusion described for ultra-high strength steels [42] did not have a complete fit for the permeated profile experiments on AISI-321SS austenitic steel.

6 FUTURE WORK

Based on the totality of the work presented, the following suggestions are made for future work:

- Carry out a prolonged low polarization current using less that 100mA for permeation experiments, in order to determine limit of permeation condition without decomposition of austenite on the entry side.
- Investigate further the influence of polarization current with respect to permeation with emphasis on breakthrough times.
- Carry out x-ray diffraction and SEM characterizations of the entry-side during permeation, in order to determine the relationship between permeation and austenite decomposition.
- Using the previous suggestions to determine the relationship between epsilon (ε) phases, and the different FCC phases.
- Use other complementary technique such as Mössbauer to investigate the relationship between the HCP, FCC, and transformed Martensitic, α'-phases
- Undertake similar investigation with other alloys such as 301, 316, and 304 steels.

7 REFERENCES

[1]: S. Chen, M. Gao and R. P. Wei: Hydride Formation and Decomposition in Electrolytically Charged Metastable Austenitic Stainless Steels. Metallurgical and Materials Transaction A; Vol. 27A, January 1996 pp 29-40.

[2]: T. Zakroczymski, J. Flis, N. Lukomski and J. Mankowski: Entry, Transport and Absorption of Hydrogen in Low-Temperature Plasma Nitrided Austenitic Stainless Steel. Acta Materialia; Vol. 49, 2001 pp 1929-1938.

[3]: T. Zakroczymski: Electrochemical Determination of Hydrogen in Metals. Journal of Electroanalytical Chemistry; Volume 475, 1999 pp 82-88.

[4]: E. H. Lee, T. S. Byun, J. D. Hunn, M. H. Yoo, K. Farrell and L. K. Mansur: On the Origin of Deformation Microstructures in Austenitic Stainless Steel: Part I-Microstructures: Acta Materialia Vol 49, January 2001 pp 3269-3276.

[5]: G. Chalaftris: Doctoral Thesis: Evaluation of Aluminum-Based Coating for Cadmium Replacement: Cranfield University: December 2003.

[6]: P. Rozenak and D. Eliezer: Environmental Hydrogen Embrittlement of Stainless Steels: Effect of Microstructure: Microstructural Science, Vol 14, pp 437-459.

[7]: D. G. Ulmer and C. J. Alstetter: Hydrogen Concentration Gradients in Cathodically Charged Austenitic Stainless Steel: Journal of Materials Research, 2(3), May/Jun 1987, pp305-312.

[8]: V. G. Gavriljuk, H. Hanninen, A. S. Tereshchenko and K. Ullakko: Hydrogen-Induced Phases in AISI 310 Type Steel; Scripta Metallurgica et Materialia; Vol 31 No 6; pp 781-785; 1994.

[9]; G. P. Tiwari, A. Bose: A study of Internal Hydrogen Embrittlement of Steel: Material Science and Engineering: A 286 (2000), P269

[10]: M. Hoelzel, S. A. Danilkin, H. Ehrenberg: Effect of High-Pressure Hydrogen Charging on the Structure of Austenitic Stainless Steels: Material Science and Engineering A, Vol. 384; 2004 pp 255-161.

[11]: K. Farrell and M. B. Lewis: The Hydrogen Content of Austenite after Cathodic Charging: Scripta Metallurgica, Vol 15, pp 661-664; 1981.

[12]: R. A. Oriani: The Diffusion and Trapping of Hydrogen in Steel: Acta Metallurgica, Vol. 18; January 1970 pp 147-157

[13]: N. R. Quick and H. H. Johnson: Hydrogen and Deuterium in Iron: Acta Metallurgica, Vol 26; 1978. pp 903-907.

[14]: C. Gabrielli, G. Maurin, L. Mirkova: Transfer Function Analysis of Hydrogen Permeation Through an Iron Membrane in a Devanathan Cell. European Internet Centre for Impedance Spectroscopy ICIS: 2004; P1-1-P1-9.

[15]: S. L. Robinson, N. R. Moody, S. M. Myers: The Effects of Current Density and Recombination Poisons on Electrochemical Charging of Deuterium Into an Iron-Base Superalloy: Journal of Electrochemical Society Vol 137 No 5; May 1990. pp 1391-1396.

[16]: A. J. Kumnick and H. H. Johnson. Steady State Hydrogen Transport Through Zone Refined Irons; Metallurgical Transactions A, Vol 6A; May 1975 pp. 1087-1091.

[17]: G. Hinds, J. Zhao, A. J. Griffiths: Hydrogen Diffusion in Super 13% Chromium Martensitic Stainless Steel: Corrosion 61; April 2005 pp. 348-454.

[18]: M. H. Abd Elhamid; Mechanistic Analysis of Hydrogen Evolution and Absorption on Iron; A Summary Report to the Electrochemical Society for a 1998 Department of Energy Summer Research Fellowship. The Electrochemical Society, spring 1999.

[19]: A. M. Brass, F. Guillon and S. Vivet; Quantification of Hydrogen Diffusion and Trapping in 2.25Cr-1Mo and 3Cr-1Mo-V Steels with the Electrochemical Permeation Technique and Melt Extractions; Metallurgical and Materials Transactions A, Vol 35A; May 2004; pp 1449-1464

[20]: R. N. Iyer and H. W. Pickering, Analysis of Hydrogen Evolution and Entry Into Metals for the Discharge-Recombination Process; Journal of Electrochemical Society Vol. 136, No. 9; September 1989, 2463

[21]: O. N. C. Uwakweh and J. M. R. Genin: Morphology and aging of the Martensite Induced by Cathodic Hydrogen Charging of High-Carbon Austenitic Steels: Metallurgical Transaction A. Vol 22A; September 1991. pp 1979-1991

[22]: R. B. Hutchings, A. Turnbull and A. T. May: Measurement of Hydrogen Transport in a Duplex Stainless Steel; Scripta Metallurgica et Materialia. Vol 25; (1991). pp 2657-2662.

[23]: M. Nabb and P. K. Foster; A new Analysis of the Diffusion of Hydrogen in Iron and Ferritic Steels: Transactions of the Metallurgical Society of AIME; Vol. 227 Jun 1963 pp618-627

[24]: R. N. Iyer and H. W. Pickering; Mechanism and Kinetics of Electrochemical Hydrogen Entry and Degradation of Metallic Systems; Annual Review Materials Science: Vol 20, 1990, pp 299-338

[25]: R. A. Oriani, J. P. Jirth, M. Smialowsky; Hydrogen Degradation of Ferrous Alloys; William Andrew Publishing/ Noyes 1985

[26]: M. E. Stroe; Doctoral Thesis: Hydrogen Embrittlement of Ferrous Materials; January 2006. Université Libre de Bruxelles.

[27]: R. K. Dayal and N. Parvathavarthini; Hydrogen Embrittlement in Power Plant Steels; Sadhana; Vol. 28, parts 3 & 4: June /August 2003; pp 431-451.

[28]: F. A. Lewis; Solubility of Hydrogen in Metals; Pure and Applied Chemistry; Vol. 62, No 11; pp 2091-2096. 1990

[29]: Bank Elektronik – Intelligent Controls GmbH; Potentiostate

[30]: M. Sjardin; Master Thesis: Techno-Economic Prospect of Small-Scale Membrane Reactors in a Future Hydrogen Fuelled Transportation Sector; August 2004.

[31]: B. J. Castro, I. Uribe, M. A. Silva; Cinetica de Permeacion de Hydrogeno en un Acero Implantado con Iones de Nitrogeno; Revista Colombiana de Fisica: Vol.34, No 1. 2002.

[32]: S. K. Yen and I. B. Huang; Hydrogen Permeation Tests in Laminates: Application to Grain/Grain Boundary of AISI430 Stainless Steel; Corrosion Vol.59, 11; November 2003. pp995

[33]: S. Prussin; Generation and Distribution of Dislocations by Solute Diffusion; Journal of Applied Physics; Vol 32, No 10; October 1961.

[34]: J. C. Li; Physical Chemistry of Some Microstructural Phenomena: Metallurgical Transactions A; Vol. 9A; October 1978. pp 1353

[35]: J. Mc Breen, L. Nanis and W Beck; A Method for Determination of the Permeation Rate of Hydrogen Through Metal Membranes: Journal of the Electrochemical Society; November 1966. pp 1218

[36]: B. D. Cullity; Elements of X-Ray Diffraction, Second Edition; Addison-Wesley Publishing 1978

[37]: T. Zakroczymski; An Electrochemical Method for Hydrogen Determination in Steel: Corrosion; 1982. pp 218

[38]: M. A. V. Devanathan and Z. Stachurski; The Mechanism of Hydrogen Evolution on Iron in Acid Solution by Determination of Permeation Rates: Journal of Electrochemical Society; Vol. 111, No 5; May 1964. pp 619

[39]: L. S. Darken and R. P. Smith; Behavior of Hydrogen in Steel During and After Immersion in Acid; Corrosion.

[40]: H. Uhlig; Why Metals Corrode; Corrosion. 1949

[41]: Y. Fukai, T. Haragushi and K. Mori; High Pressure Phase Diagrams of Transition Metals-hydrogen systems; 2000.

[42]: S. Charca-Mamani; Master of Science Thesis: Study of Hydrogen Permeation and Diffusion in Steels: Predictive Model for Determination of Desorbed Hydrogen Concentration; 2005. University of Puerto Rico – Mayaguez.

[43]: M. Smialowski; Hydrogen in Steel, Effect of Hydrogen on Iron and Steel During Production, Fabrication, and Use; Addison-Wesley Publishing 1962

[44]: R. Mousavinejad; Master of Applied Science thesis: Gas Phase Hydrogen Permeation in Pd-25% Ag; 2005. University of Toronto.

[45]: Y. Nishino, M. Obata and S Asano; Hydrogen-Induced Phase Transformations in Fe_{50}-$Ni_{50-x}Mn_x$ Alloys; Scripta Metallurgica et Materialia, Vol 24, 1990. pp 703-708

[46]: G.B. Olson and Morris Cohen; A General Mechanism of Martensitic Nucleation: Part I. General Concepts and the FCC → HCP Transformation; Metallurgical Transactions A, Vol 7A December 1976. pp 1897-1904

[47]: ASTM G 148-97 (Reapproved 2003): Standard Practice for Evaluation of Hydrogen Uptake, Permeation and Transport in Metals by an Electrochemical Technique

[48]: ASTM 1974: Hydrogen Embrittlement Testing. Symposium Presented at the Seventy-Fifth Annual Meeting American Society for Testing and Materials, Los Angeles, California, 25 June 1972.

[49]: J. P. Hirth; Effects of Hydrogen on the Properties of Iron and Steel; Metallurgical Transactions A, Vol 1A, Number 6. 1980. pp 861-890

[50]: B. G. Pound; The Effect of Aging on Hydrogen Trapping in Precipitation-Hardened Alloys; Corrosion Science, 42. 2000. pp 1941-1956

[51]: www.aksteel.com; Product Data Sheet, 321 Stainless Steel.

[52] M. S. Iotov; Doctor of Philosophy Science thesis: Diffusion in Amorphous Media; 1998. California Institute of Technology

[53] T. Zakroczymski, Entry of Hydrogen into Iron Alloys from the Liquid Phase; in "Hydrogen Degradation of Ferrous Alloys" (R.A. Oriani, J.P. Hirth, M. Smiałowski, Eds.) Noyes Publications, Park Ridge, New Jersey, U.S.A., 1985.

[54] C. Christensen, Hydrogen Monitoring in Geothermal Plants and Oil and Gas Refineries; Nordtest Report, Finland, TR 474, Approved 2001.

[54] N. R. Moody, Deuterium Concentration Profiles in Fe-Ni-Co Alloys Electrochemically Charged at Room Temperature. Acta Metallurgica, Vol 37, 1989, No 1, pp. 281-290.

[55] G. R. Caskey, Jr., Hydrogen Effects in Stainless Steel; in “Hydrogen Degradation of Ferrous Alloys" (R.A. Oriani, J.P. Hirth, M. Smiałowski, Eds.) Noyes Publications, Park Ridge, New Jersey, U.S.A., 1985.

[56] O. N. C. Uwakweh, A. S. Vinod; Mössbauer Effect Study of Room Temperature Cathodic Polarization of AISI-321 Austenitic Stainless Steel. Department of Science and Engineering of Materials, University of Puerto Rico. In preparation. 2007.

[57] C. M. Hsiao and W. Chu. Beijing University of Iron and Steel Technology. Article included in Hydrogen Effects in Metals. Edited by I. M. Bernstein. Conference Proceedings, The metallurgical Society of AIME. March, 1981.

APPENDIX A

A.1. Methods to determined the diffusion coefficient

Slope Method.

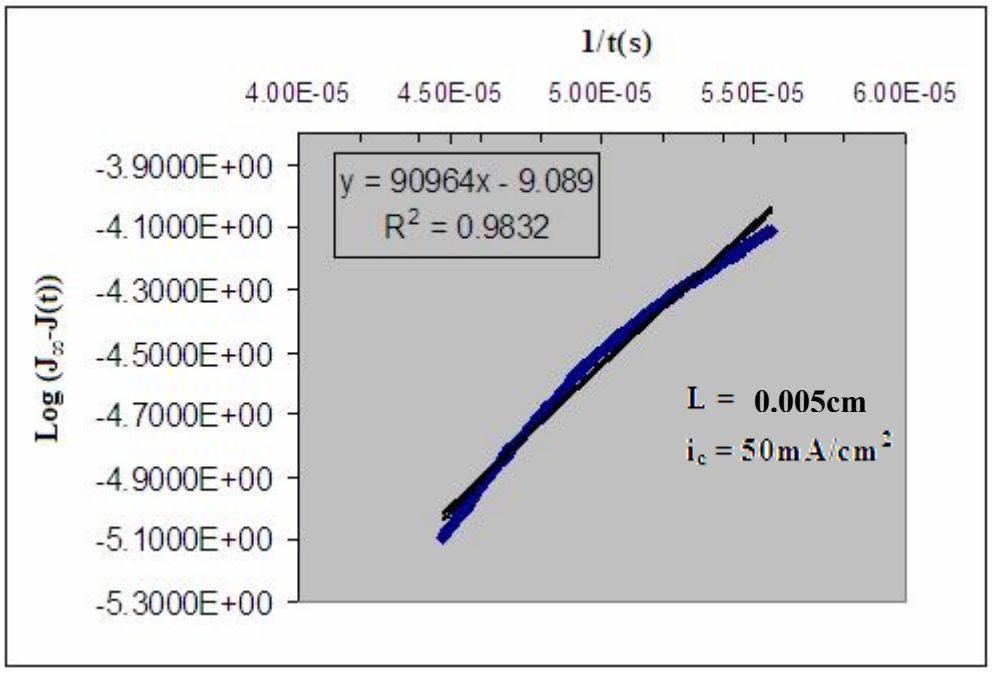

Figure A.1.1 Slope determined from a hydrogen permeation transient profile for AISI-321SS Stainless Steel

Once the profile of hydrogen permeation is observed, it is possible to calculate the diffusion coefficient by the analysis of the transient zone. The slope obtained from the linear plot of $log\,(J_\infty - J(t))$ Vs 1/t(s) is an approximation of the following equation:

$$K = \frac{L^2 \log(e)}{4D} \qquad \textbf{A.1.1}$$

Where K represents the slope obtained, L is the thickness of the sample, D is the apparent diffusion coefficient and the value of ***e*** equals 2.71828182846. In this case the value of D can be found substituting the values mentioned.

A.2. Methods to determine the hydrogen fraction as seen in the permeation profiles

Figure A.2.1 shows the typical sigmoid permeation profile of an AF1410 sample charged at a current density of 25mA/cm^2 (current of 50mA). In order to obtain the total amount of hydrogen ($q_{H,\ Total}$ in mol H per unit area) stored in the membrane before the charging interruption (turn off the power supply), the currents $J_{H,\ 0}$ and $J_{H,\ L}$ (Equation 2.11 and 2.12 accordingly) need to be integrated with respect to time to get the amounts of hydrogen leaving the membrane at entry and exit side [2, 3]. Analytical integration of Equation 2.11 and Equation 2.12 give the following result:

$$q_{H,0} = \frac{2 j_H^o L^2}{\pi^2 DF}\left[\sum_{n=1}^{\infty}\frac{1}{n^2} - \sum_{n=1}^{\infty}\frac{1}{n^2}\exp\left(-\frac{n^2\pi^2 Dt}{L^2}\right)\right] \qquad \textbf{A.2.1}$$

and

$$q_{H,L} = \frac{2 j_H^o L^2}{\pi^2 DF}\left[\sum_{n=1}^{\infty}\frac{(-1)^n}{n^2}\exp\left(-\frac{n^2\pi^2 Dt}{L^2}\right) - \sum_{n=1}^{\infty}\frac{(-1)^n}{n^2}\right] \qquad \textbf{A.2.2}$$

The final amounts of the desorbed hydrogen for a $t \to \infty$, are:

$$q_{H,0} = \frac{2 j_H^o L^2}{\pi^2 DF}\left[\sum_{n=1}^{\infty} \frac{1}{n^2}\right] \qquad \textbf{A.2.3}$$

and

$$q_{H,L} = \frac{2 j_H^o L^2}{\pi^2 DF}\left[-\sum_{n=1}^{\infty} \frac{(-1)^n}{n^2}\right] \qquad \textbf{A.2.4}$$

Finally the equations reduce respectively to:

$$q_{H,0} = \frac{j_H^o L^2}{3DF} \qquad \text{H-mol/cm}^2 \qquad \textbf{A.2.5}$$

$$q_{H,L} = \frac{j_H^o L^2}{6DF} \qquad \text{H-mol/cm}^2 \qquad \textbf{A.2.6}$$

And the total amount of hydrogen $q_{H,\ Total}$ as shown previously in Equation 4.3, is the addition of the Equations 4.1 and 4.2 that yields the to the following result:

$$q_{H,TOTAL} = q_{H,L} + q_{H,0} = \frac{j_H^0 L^2}{2DF} \qquad \text{H-mol/cm}^2 \qquad \textbf{A.2.7}$$

The corresponding values of the amount of hydrogen in mol per unit area are shown conveniently in every permeation profile as a double Y axis (right side of the figure) for comparison with the obtained current densities registered during hydrogen permeation (left side of the figure).

J_H^o with units of μA/cm^2, represents the initial steady state permeation rate of hydrogen; this value can be obtained directly from the current density registered by the potentiostat during hydrogen permeation. Values of the apparent diffusivity (D) were found by the slope method.

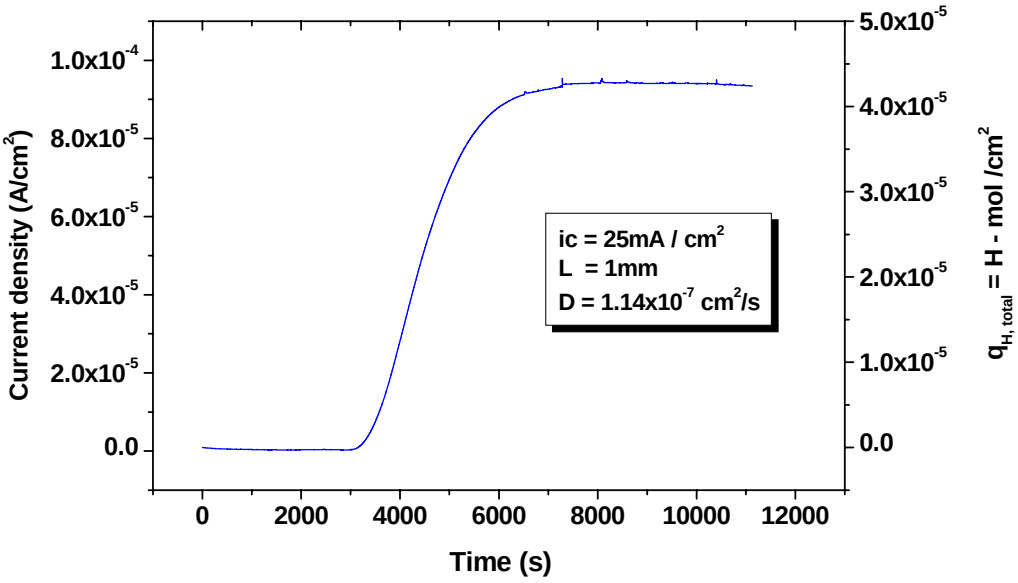

Figure A.2.1 Hydrogen sigmoid permeation profile of an AF1410 sample with corresponding values of current density and total amount of hydrogen in the sample

APPENDIX B.

B.1. Mathematical approximation to determine the subsurface concentration

Certain conditions have to be achieved to obtain the subsurface concentration (C_o). A sample of thickness L is cathodically charged with hydrogen on the entry side (X=0). In contrast the

hydrogen desorbing at the opposite side (X=L) is being oxidized by anodic currents. The hydrogen concentration in the membrane at the entry side is assumed to be constant (C_0), while at the exit side it is assumed to be equal to zero (C_L=0). Fick's first law equates each electron of the oxidation current to a hydrogen atom permeating the sample; as a result if F is the faraday constant (96500 coulombs mole $^{-1}$), then the permeation current J (A/cm^2) is given by:

$$J = -DF\frac{dC}{dx} \qquad \textbf{B.1.1}$$

Once the values of the diffusivity (D) and the sample thickness (L) are known, and a steady state was achieved during the permeation process (J_∞); a constant flux permeation through the sample (per unit area) in units of current density can be expressed as follows:

$$J_\infty = \frac{FDC_0}{L} \qquad \textbf{B.1.2}$$

From Equation B.1.2, the subsurface (Co) can be found.